

Optimal Cloud Analysis (OCA) Release 1 Validation Report

DOI: 10.15770/EUM_SEC_CLM_0049 (0DEG)

Doc.No. : EUM/OPS/REP/21/1209273
Issue : v2F e-signed
Date : 31 May 2022
WBS/DBS :

EUMETSAT
Eumetsat-Allee 1, D-64295 Darmstadt, Germany
Tel: +49 6151 807-7
Fax: +49 6151 807 555
<http://www.eumetsat.int>

This page intentionally left blank

Change Record

<i>Version</i>	<i>Date</i>	<i>DCR* No. if applicable</i>	<i>Description of Changes</i>
1D	14/12/2021		Draft for internal review
2A	27/01/2022		Internal review completed
2B	16/02/2022		Internally approved
2F	31/05/2022		comments from external reviewers accepted

****DCR = Document Change Request***

Table of Contents

1	SUMMARY	9
2	INTRODUCTION	10
2.1	Purpose and Scope	11
2.2	Applicable Documents	11
2.3	Reference Documents	11
2.4	Acronyms	12
3	DATA RECORD SUMMARY	14
3.1	Spatial and temporal coverage	14
4	DATA USED FOR THE VALIDATION	16
4.1	DARDAR	16
4.2	CALIPSO L3 GEWEX cloud top product	17
4.3	CLAAS 2.1	17
4.4	MODIS L3	18
5	VALIDATION STRATEGY	20
5.1	Comparison against A-Train CloudSat and CALIPSO measurements	20
5.2	Comparison against MODIS and CLAAS 2.1	23
6	OVERALL EVALUATION	25
6.1	OCA daytime temporal analyses	26
6.1.1	Daily and monthly aggregation	26
6.1.2	Daily and monthly cloud properties	27
6.2	Example of geographical distribution	30
6.3	Evaluation Outcome	35
7	COMPARISON AGAINST REFERENCE DATA	36
7.1	OCA vs DARDAR	36
7.1.1	Evaluation of the OCA product uncertainty	46
7.2	OCA vs MODIS and CLAAS 2.1	48
7.2.1	Cloud Top Pressure (CTP)	49
7.2.2	Cloud Optical Thickness (COT)	53
7.2.3	Cloud Particle Effective Radius (CRE)	55
8	COMPARISON OPERATIONAL NEAR REAL TIME (NRT) SEVIRI OCA	60
8.1.1	Single product comparison	60
8.1.2	Long term comparison	63
9	LIMITATIONS AND POSSIBLE FUTURE IMPROVEMENTS	66
10	CONCLUSIONS	67
APPENDIX A	TIME SERIES AT 00 AND 12UTC	68
APPENDIX B	HOVMOELLER DIAGRAM FOR ALL DAY RETRIEVAL	69

Table of Figures

Figure 1: Spatial coverage of Meteosat SSP at 0° exploited for OCA up to 65 degrees. The area covered also by the backup platforms at 3.4W and at 9.5E are shown. The common retrieved area along the whole data record time coverage is also shown.	16
Figure 2: Frequency of detection for multi-layer pixels as function of the cloud layers separation (in km) and optical thickness of the topmost layer. Left: multi-layer pixels, as defined by DARDAR, also detected by OCA. Right: multi-layer pixels detected by DARDAR. Excluded are cases where the cloud top height of the second layer differs by more than 7 km between OCA and DARDAR, indicating high likelihood that the instruments measured different parts of the cloud.	22
Figure 3: MODIS true color RGB image of the scene analysed in Figure 4 and Figure 5. The blue line shows the track of AQUA ascending orbit. The image is rotated by 90° and the left side is at 57S latitude, the right side at 22S latitude.	23
Figure 4: Section of an A-Train granule extending from 63.4S-27.1E to 21.8S-10.8E on the 1 st of June 2007. The three panels show from the top: DARDAR cloud feature mask, CloudSat reflectivity, CALIPSO backscatter and DARDAR retrieved ice water content. In the lower panel, the contour lines show the temperature from the corresponding ECMWF forecasts.	23
Figure 5: Example of identification of cloud tops from DARDAR and CALIPSO data for the granule section of Figure 4. Red dots show the cloud top inferred from the A-Train data, green dots show the OCA cloud top where the identification of single or two-layer agrees with the one from DARDAR data. The top panel shows the cloud top for single layers only, middle panel the cloud top of the upper layer of two-layer profiles and lower panel the cloud top of the second layer of two-layer profiles. The orange dots in the first two panels show where the identification from OCA does not agree with DARDAR: this means OCA two-layer in the first panel and OCA single layer in the middle panel.	24
Figure 6: Time series for the average daily cloud properties computed using for all available slots of that day: CRE (upper panel), COT (middle panel) and CTP (bottom panel). The plots distinguish among the cloud phases.	26
Figure 7: Hovmoeller diagram daily mean number of valid retrieval in each 1 degree box. A box is filled with a value if at least 20% of the pixels have been retrieved.	27
Figure 8: Hovmoeller diagram of the zonal mean (+60°-60°) of monthly percentage of available days.	28
Figure 9: Hovmoeller diagram of zonal mean (+60° to -60°) monthly cloud top pressure (hPa). Upper panel includes all data; lower panel includes only filtered data using a threshold at 60% (lower panel).	29
Figure 10: Monthly Hovmoeller diagrams of the zonal mean of the cloud type fraction of one-layer water (upper panel), one-layer ice (middle panel), two-layers (bottom panel). The values are averaged over 1-degree box and over a month. So the total for all cases is not expected to be 100%. No threshold on the available number of days per month is applied.	30
Figure 11: Monthly Hovmoeller diagrams for zonal mean (+60° to -60°) cloud optical thickness (upper panel) and cloud particle effective radius (bottom panel). No threshold on the available number of days per month is applied.	31
Figure 12: Daily numbers of one-layer water clouds (upper left sub-panel), ice clouds (upper right sub-panel) two-layers clouds (lower left sub-panel) and rejected values (lower right sub-panel). The four main-panels present a boreal winter and summer cases in 2005 (Meteosat-8) and 2018 (Meteosat-10). Only quality-controlled values are shown in the plots.	33
Figure 13: Daily numbers of cloud top pressure (upper left sub-panel), cloud effective radius (upper right sub-panel) cloud optical thickness (lower left sub-panel) and number rejected retrievals (lower right sub-panel). The four main-panels present a boreal winter and summer cases in 2005 (Meteosat-8) and 2018 (Meteosat-10). All values are shown, without any quality control screening.	34
Figure 14: Monthly fraction of one-layer water clouds (upper left sub-panel), ice clouds (upper right sub-panel) two-layers clouds (lower left sub-panel) and valid percentage of daily values per month (lower right sub-panel). The four main-panels present a boreal winter and summer cases in 2005 (Meteosat-8) and 2018 (Meteosat-10). All values are shown, without any quality control screening. A threshold of 60% is applied.	35
Figure 15: Monthly averages of cloud top pressure (upper left sub-panel), cloud effective radius (upper right sub-panel) cloud optical thickness (lower left sub-panel) and valid percentage of daily values	

per month (lower right sub-panel). The four main-panels present a boreal winter and summer cases in 2005 (Meteosat-8) and 2018 (Meteosat-10). A threshold of 60% is applied.....	36
Figure 16: Time series cloud top height of single-layer clouds from OCA (continuous line) and DARDAR (dashed line) for daytime orbits. Top panel: mean for collocated products within one granule crossing the SEVIRI disk. The coloured shading shows one standard deviation of DARDAR data. Lower panel: mean and standard deviation of the differences between OCA and DARDAR cloud top height. Data are divided between ice (blue lines) and liquid (green lines) clouds.....	37
Figure 17: As Figure 16 but for two-layer pixels. Data are divided between upper layer (blue lines) and second layer (green lines).	38
Figure 18: Scatter plots of cloud top height (km) retrieved by OCA and DARDAR for all the collocated pixels in the daytime granules. Upper panels: single layer pixels ice (left) and liquid (right). Lower panels: two-layer pixels top layer (left) and second layer (right).	40
Figure 19: As Figure 18 but for the collocated pixels in the nighttime granules.....	41
Figure 20: Scatter plots of ice cloud optical thickness and effective radius retrieved by OCA and DARDAR for all the collocated pixels in the daytime granules. Upper panels: cloud optical thickness for pixels identified as single layer (left) and two-layer (right). Lower panels: cloud top effective radius for pixels identified as single layer (left) and two-layer (right). For the two-layer pixels only the total COT from DARDAR where both upper and lower layers are of type ice are used.....	43
Figure 21: As Figure 20 but for the collocated pixels in the nighttime granules.....	44
Figure 22: Comparison of cloud categorisation in OCA and DARDAR (DD). The categories are single layer ice (SL_i), single layer liquid (SL_l) and multi layer (ML). The multi layer category is further divided into upper layer (MLu) and lower layer (MLl) and both can be of the type ice (MLu_i, MLl_i) or liquid (MLu_l, MLl_l). The numbers and colors refer to the percentage of cases with respect to the total of that category (blue=ice, green=liquid, red=multi-layer). For OCA, the multi-layer category only allows ice for the upper layer while for the lower layer the phase is not defined. The comparison is done for the daytime A-Train orbits collocated with SEVIRI with the quality-control filter applied as explained in the text.	46
Figure 23: Scatter plots of cloud top height (km) retrieved by OCA and DARDAR for all the collocated pixels in the daytime granules for the profiles where the single/two layer characterisation does not agree between OCA and DARDAR. Left: profiles where OCA retrieves two layer clouds and DARDAR single layer. The first layer in the OCA retrieval is shown. Right: profiles where OCA retrieves single layer clouds and DARDAR shows multiple layers. The OCA CTH is compared to the second layer in the DARDAR profile.	47
Figure 24: CTH comparison between OCA and DARDAR for the ice cloud type. The comparison includes all cases of single and multi-layer profiles. The left hand side plot includes the profiles where the multi-layer categorisation does not agree between OCA and DARDAR. In the right hand side plot only includes points where the multi-layer categorisation agrees between the two datasets. Data are for the set of day-time orbits between 2007 and 2015.....	47
Figure 25: OCA CTH uncertainty validation expressed as the difference between OCA and DARDAR CTH scaled by the combination of retrieval uncertainty and uncertainty due to the comparison procedure (see text). Top panels are for day-time orbits 2007-2016 and lower panel for night-time orbits (2007-2010). Left are results for one-layer liquid clouds and right for one-layer ice clouds. Large values indicate that the uncertainty is likely too small to correctly account for the observed difference between the OCA and DARDAR CTH.	49
Figure 26: Seasonal mean combined (ice+liquid water clouds) CTP from OCA, MODIS, CLAAS 2.1 and CALIOP GEWEX L3 datasets. On the bottom the difference between OCA and respectively MODIS, CLAAS 2.1 and CALIPSO GEWEX L3 (passive CTP flavour). White areas in the OCA and CLAAS 2.1 figures indicate regions where not enough valid retrieval were available (see text for details).....	51
Figure 27: OCA (a) and CLAAS 2.1 (b) CTP (hPa) retrieval over western Sahara for the repeat cycle at 12UTC on the 20th of January 2010. In blue are clouds with low CTPs and in red clouds with high CTPs. RGB composite from SEVIRI channels 0.63 μm , 0.87 μm , 1.6 μm (c) and 0.63 μm , 0.87 μm , 10.8 μm (d).	52
Figure 28: As Figure 26 but only showing the CTP comparison between OCA and CALIPSO L3 GEWEX for the TopLayer version	53
Figure 29: Weighted area-average of retrieved cloud top pressure (CTP) from OCA, MODIS, CLAAS 2.1 and CALIPSO L3 GEWEX (passive CTP flavour) datasets over a SEVIRI disk. Averages are done for the areas within a maximum SEVIRI viewing angle of 50°. Top panel: monthly means	

with a lowess (locally weighted scatter plot smooth) smoothing filter applied to each time series. Lower panel: differences between OCA and respectively MODIS, CLAAS 2.1 and CALIPSO L3.54

Figure 30: Seasonal mean combined (ice+liquid water clouds) cloud optical thickness (COT) from OCA, MODIS and CLAAS 2.1 datasets. On the right the difference between OCA and respectively MODIS and CLAAS 2.1. White areas in the OCA and CLAAS 2.1 figures indicate regions where not enough valid retrieval were available (see text for details).55

Figure 31: Weighted area-average of retrieved cloud optical thickness (COT) from OCA, MODIS and CLAAS 2.1 datasets over a SEVIRI disk. Averages are done for the areas within a maximum SEVIRI viewing angle of 50°. Top panel: monthly means with a lowess (locally weighted scatter plot smooth) smoothing filter applied to each time series. Lower panel: differences between OCA and respectively MODIS and CLAAS 2.156

Figure 32: Seasonal mean ice water clouds effective radius (CRE) from OCA (single layer and two-layer), MODIS and CLAAS 2.1 datasets. On the right the difference between OCA and respectively MODIS and CLAAS 2.1. White areas in the OCA and CLAAS 2.1 figures indicate regions where not enough valid retrieval were available for this cloud phase. Similarly for the MODIS figures the white areas are regions for which the ice cloud fraction according to the Cloud_Retrieval_Fraction_Ice_FMean variable is less than 0.2 (see section 5.2).57

Figure 33: Weighted area-average of retrieved ice water cloud effective radius (CRE) from OCA (single layer and two-layer), MODIS and CLAAS 2.1 datasets over a SEVIRI disk. Averages are done for the areas within a maximum SEVIRI viewing angle of 50°. Top panel: monthly means with a lowess (locally weighted scatter plot smooth) smoothing filter applied to each time series. Lower panel: differences between OCA and respectively MODIS and CLAAS 2.158

Figure 34: Seasonal mean liquid water clouds effective radius (CRE) from OCA, MODIS and CLAAS 2.1 datasets. On the right the difference between OCA and respectively MODIS and CLAAS 2.1. White areas in the OCA and CLAAS 2.1 figures indicate regions where not enough valid retrieval were available for this cloud phase. Similarly for the MODIS figures the white areas are regions for which the liquid cloud fraction according to the Cloud_Retrieval_Fraction_Liquid_FMean variable is less than 0.3 (see section 5.2).59

Figure 35: Weighted area-average of retrieved liquid water cloud effective radius (CRE) from OCA, MODIS and CLAAS 2.1 datasets over a SEVIRI disk. Averages are done for the areas within a maximum SEVIRI viewing angle of 50°. Top panel: monthly means with a lowess (locally weighted scatter plot smooth) smoothing filter applied to each time series. Lower panel: differences between OCA and respectively MODIS and CLAAS 2.160

Figure 36: Comparison of single products for the 26th of January 2018 boreal winter: night case (upper panel) and daylight case (bottom panel).62

Figure 37: Same as Figure 36 for boreal summer: 15th of July 201863

Figure 38: Case at 00 UTC (a) all pixels used for the average; (b) only common retrieved pixels used for the average. Cloud top pressure in hPa (upper plot) and number of retrievals (bottom plot). NRT in blue, CDR in red, dashed line for ice and continuous line for water.65

Figure 39: Same as Figure 38 for the daylight case at 12:00 UTC66

Figure 40: Time series for the 12UTC repeat cycle for the cloud properties averaged over the SEVIRI disk: CRE (upper panel), COT (middle panel) and CTP (bottom panel). The plots distinguish among the cloud phases. The upper bad in the upper panel shows the lifetime of the primary satellite providing the measurements. The colorbar at the top shows the Meteosat satellite used at a particular point in time.69

Figure 41: As but for the 00UTC repeat cycle69

Figure 42: Monthly Hovmoeller diagrams for zonal mean (60°-60°) COT. No threshold on the available number of days per month is applied70

Figure 43: Monthly Hovmoeller diagrams for zonal mean (60°-60°) CTP. No threshold on the available number of days per month is applied70

Figure 44: Monthly Hovmoeller diagrams for zonal mean (60°-60°) CRE. No threshold on the available number of days per month is applied71

Table of Tables

Table 1: Satellite, instrument, mission, nominal orbit position and services for the period 2004-2007. The period includes Meteosat 8-11 (MSG).	15
Table 2: summary of the main differences in spatial and temporal resolution between L2 and L3 retrieval products from OCA-SEVIRI and MODIS. OCA is provided to the users at the native SEVIRI resolution of 15 minutes (Level 2). The aggregation to monthly mean (Level 3) has been done for comparison purposes only.	19
Table 3: Summary of the statistics from a set of A-Train granules collocated with SEVIRI pixels. Cloud top height (CTH), ice cloud effective radius at cloud top (CRE) and ice clouds optical thickness (COT) are shown for OCA and DARDAR retrievals. In brackets the standard deviation computed over all the collocated products.	44

1 SUMMARY

This document presents the validation of the Optimal Cloud Analysis (OCA) Climate Data Record (CDR) Release 1 cloud properties (cloud top pressure, cloud optical thickness, cloud particles effective radius and cloud phase) retrieved by a adapted version of the OCA Near Real Time (NRT) algorithm using as inputs the 15 minutes Spinning Enhanced Visible and Infrared Imager (SEVIRI) measurements (from Meteosat-8 to Meteosat-11) during the period 2004-2019. The OCA algorithm has been used in near real time at EUMETSAT as demonstrational SEVIRI L2 cloud product since 2013. The main feature that sets OCA apart from existing similar radiometer-based retrieval algorithms is its capability to detect and retrieve cloud properties for two overlapping cloud layers with full error estimates. The CDR extends the OCA retrieval back to 2004 by producing for the first time OCA using all of the Meteosat-9 and Meteosat-8 measurements.

A significant application of the OCA CDR is its usage as the main source for cloud height assignment and associated uncertainty for assigning the height of the SEVIRI Atmospheric Motion Vectors (AMV). The validation of the cloud top pressure (CTP) is especially important. Nevertheless, the quality of other values retrieved by OCA has been included in the product validation.

The main goal of this validation is to confirm the homogeneity and consistency of the CDR and the accuracy of the reprocessing products, especially cloud top pressure/height, within the known limits of the algorithm throughout the entire period. The outcome is that CTP retrieval is homogenous, stable and consistent across all four Meteosat platforms.

We analysed the comparison of the OCA CDR against the operational OCA NRT archive product for the year 2018, collocated measurements and retrieval products from other independent satellite measurements such as polar orbiting radar and lidar from CloudSat and CALIPSO, and reference L3 products from MODIS and CLAAS 2.1 CDR covering the same period. The outcome is that CDR and NRT are consistent even if some differences are present and mainly due to the usage of very different cloud masking. The comparison against independent reference dataset shows good agreement for CTP. The bias found when comparing against Lidar measurements is in line with previous studies and to be expected, in particular in case of high thin ice clouds. The retrieval of the cloud optical thickness and particle effective radius is most reliable for daytime measurements (when solar channels are available) while the cloud top height retrieval is of comparable quality for daytime and nighttime SEVIRI slots. The comparison of the OCA Release 1 CDR against other two independent satellite reference CDRs (MODIS L3 and CLAAS 2.1) shows that the products of the three different algorithms are compatible and consistent over the whole period 2004-2019. This is particularly true for the cloud top pressure and for the cloud optical thickness while for cloud microphysics results are less comparable between the databases. As a outcome of the validation, some potential improvements (e.g. better input cloud masking and more realistic modelling for the detection of high thin ice clouds) have been identified and they might be included in a future release.

2 INTRODUCTION

The Optimal Cloud Analysis (OCA) algorithm was first developed as a research study awarded to the Rutherford Appleton Laboratory (RAL) in 1997 and was coded as a prototype processor in 2001. The algorithm was developed by EUMETSAT with the aim of providing potential Day-2 products from the Meteosat Second Generation (MSG) Spinning Enhanced Visible and Infrared Imager (SEVIRI) instrument.

Since June 2013, the OCA products have been operationally generated at full repeat cycle (15 min) frequency as a demonstration product. Cloud properties retrieved by OCA are cloud top pressure, cloud optical thickness, cloud effective radius and cloud phase. In order to generate a homogeneous data record over the period 2004-2019, the OCA algorithm has been adapted for reprocessing, allowing fast time series generation and the ingestion of a different cloud mask.

While the detection of multi-layer (a.k.a ‘overlap’) clouds is quite a common output in cloud schemes, a key characteristic of the OCA algorithm is the ability to estimate the cloud properties of up to two-layers, in favourable situations at least. This is a distinguishing feature of this dataset in comparison to other available long time series cloud products from passive imagers such as SEVIRI. It also provides an estimation of the retrieval uncertainty that could be propagated in downstream algorithm such as the one for the derivation of Atmospheric Motion Vectors (AMV), the main objective for the generation of a temporally complete and homogeneous OCA data record.

The OCA Release 1 Climate Data Record¹ (CDR) has been produced with the aim to provide a fully consistent long-term data record employing the most up-to-date available Near Real Time (NRT) version of the OCA processor using as inputs consistent auxiliary inputs and most up-to-date version of MSG Level-1 products.

The OCA Release 1 covers the 15-year period of SEVIRI measurements from MSG -8, -9, -10, and -11 during the period February 2004 until August 2019². The quality of OCA Release 1 has been evaluated using different types of analyses:

- Temporal consistency evaluation to verify the completeness of the retrieval, the stability in time and the presence of the typical geographical and seasonal features;
- Validation of the cloud properties against retrieval from observations acquired by the same platform such as the CLAAS-2.1;
- Validation against independent satellite observations from instruments on board both geostationary and polar-orbiting platforms mainly from the A-Train constellation;
- Comparison against the EUMETSAT’s OCA NRT archived product.

¹ CDRs consist of a consistently processed time series of uncertainty-quantified retrieved values of a geophysical variable or related indicator, located in time and space, and of sufficient length and quality to be useful for climate science or applications (definition from the joint CEOS/CGMS working group on climate).

² The CDR stops in August 2019 as this is the end of ERA interim reanalysis data that is used as input for the OCA retrieval

2.1 Purpose and Scope

The purpose of this document is to provide comprehensive validation of the first release of Optimal Cloud Analysis Release 1 (OCA R1) Climate Data Record (CDR).

2.2 Applicable Documents

None

2.3 Reference Documents

Bennartz, R., Fell, F., and Walther, A.: AVAC-S: A-Train Validation of Aerosol and Cloud properties from SEVIRI, , EUM-07-839-INF, 2010.

Delanoë, J. and Hogan, R. J.: A variational scheme for retrieving ice cloud properties from combined radar, lidar, and infrared radiometer, *J. Geophys. Res.*, 113, D07204, <https://doi.org/10.1029/2007JD009000>, 2008.

Delanoë, J. and Hogan, R. J.: Combined CloudSat-CALIPSO-MODIS retrievals of the properties of ice clouds, *J. Geophys. Res.*, 115, D00H29, <https://doi.org/10.1029/2009JD012346>, 2010.

EUMETSAT: MTG-FCI: ATBD for Optimal Cloud Analysis Product, 2016.

EUMETSAT: Optimal Cloud Analysis (OCA) Release 1 Product Users Guide, 2021.

Finkensieper, Stephan, Meirink, Jan Fokke, van Zadelhoff, Gerd-Jan, Hanschmann, Timo, Benas, Nikolas, Stengel, Martin, Fuchs, Petra, Hollmann, Rainer, Kaiser, Johannes, and Werscheck, Martin: CLAAS-2.1: CM SAF CLOUD property dAtAset using SEVIRI - Edition 2.1 (3.1), https://doi.org/10.5676/EUM_SAF_CM/CLAAS/V002_01, 2020.

Hamann, U., Walther, A., Baum, B., Bennartz, R., Bugliaro, L., Derrien, M., Francis, P. N., Heidinger, A., Joro, S., Kniffka, A., Le Gléau, H., Lockhoff, M., Lutz, H.-J., Meirink, J. F., Minnis, P., Palikonda, R., Roebeling, R., Thoss, A., Platnick, S., Watts, P., and Wind, G.: Remote sensing of cloud top pressure/height from SEVIRI: analysis of ten current retrieval algorithms, *Atmos. Meas. Tech.*, 7, 2839–2867, <https://doi.org/10.5194/amt-7-2839-2014>, 2014.

Hoffmann, L., Günther, G., Li, D., Stein, O., Wu, X., Griessbach, S., Heng, Y., Konopka, P., Müller, R., Vogel, B., and Wright, J. S.: From ERA-Interim to ERA5: the considerable impact of ECMWF's next-generation reanalysis on Lagrangian transport simulations, *Atmos. Chem. Phys.*, 19, 3097–3124, <https://doi.org/10.5194/acp-19-3097-2019>, 2019.

Hubanks, P. A., Platnick, S., King, M. D., and Ridgway, W. L.: MODIS Atmosphere L3 Global Gridded Product User's Guide & ATBD for C6.1 Products: 08_D3, 08_E3, 08_M3, 2020.

King, M. D., Kaufman, Y. J., Menzel, W. P., and Tanre, D.: Remote sensing of cloud, aerosol, and water vapor properties from the moderate resolution imaging spectrometer (MODIS), *IEEE Trans. Geosci. Remote Sensing*, 30, 2–27, <https://doi.org/10.1109/36.124212>, 1992.

Meirink, J. F., Roebeling, R. A., and Stammes, P.: Inter-calibration of polar imager solar channels using SEVIRI, *Atmos. Meas. Tech.*, 6, 2495–2508, <https://doi.org/10.5194/amt-6-2495-2013>, 2013.

Merchant, C. J., Paul, F., Popp, T., Ablain, M., Bontemps, S., Defourny, P., Hollmann, R., Lavergne, T., Laeng, A., de Leeuw, G., Mittaz, J., Poulsen, C., Povey, A. C., Reuter, M., Sathyendranath, S., Sandven, S., Sofieva, V. F., and Wagner, W.: Uncertainty information in climate data records from Earth observation, *Earth Syst. Sci. Data*, 9, 511–527, <https://doi.org/10.5194/essd-9-511-2017>, 2017.

Platnick, S., Meyer, K. G., King, M. D., Wind, G., Amarasinghe, N., Marchant, B., Arnold, G. T., Zhang, Z., Hubanks, P. A., Holz, R. E., Yang, P., Ridgway, W. L., and Riedi, J.: The MODIS Cloud Optical and Microphysical Products: Collection 6 Updates and Examples From Terra and Aqua, *IEEE Trans. Geosci. Remote Sensing*, 55, 502–525, <https://doi.org/10.1109/TGRS.2016.2610522>, 2017.

Stephens, G. L., Vane, D. G., Boain, R. J., Mace, G. G., Sassen, K., Wang, Z., Illingworth, A. J., O’connor, E. J., Rossow, W. B., Durden, S. L., Miller, S. D., Austin, R. T., Benedetti, A., Mitrescu, C., and the CloudSat Science Team: THE CLOUDSAT MISSION AND THE A-TRAIN: A New Dimension of Space-Based Observations of Clouds and Precipitation, *Bull. Amer. Meteor. Soc.*, 83, 1771–1790, <https://doi.org/10.1175/BAMS-83-12-1771>, 2002.

Watts, P. D., Bennartz, R., and Fell, F.: Retrieval of two-layer cloud properties from multispectral observations using optimal estimation, *J. Geophys. Res.*, 116, D16203, <https://doi.org/10.1029/2011JD015883>, 2011.

Winker, D. M., Pelon, J. R., and McCormick, M. P.: The CALIPSO mission: spaceborne lidar for observation of aerosols and clouds, *Third International Asia-Pacific Environmental Remote Sensing Remote Sensing of the Atmosphere, Ocean, Environment, and Space*, Hangzhou, China, 1, <https://doi.org/10.1117/12.466539>, 2003.

2.4 Acronyms

The below table lists acronyms and abbreviations used in this document:

Acronyms	Meaning
AMV	Atmospheric Motion Vector
ATBD	Algorithm Theoretical Basis Document
AVAC-S	A-Train Validation of Aerosol and Cloud Properties from SEVIRI
CALIPSO	Cloud-Aerosol Lidar and Infrared Pathfinder Satellite Observations
CDR	Climate Data Record
CFC	Cloud Fractional Cover
CLAAS	CLoud property dAtAset using SEVIRI
CLM	CLoud Mask
CM-SAF	Climate Monitoring - Satellite Application Facility

COT	Cloud Optical Thickness
CPL	Cloud Physics Lidar
CPP	Cloud Physical Properties
CRE	Cloud Particle Effective Radius
CTH	Cloud Top Height
CTP	Cloud Top Pressure
DARDAR	raDAR/liDAR
ECMWF	European Centre for Medium-Range Weather Forecasts
EUMETSAT	European Organisation for the Exploitation of Meteorological Satellites
FOV	Field Of View
ICARE	Cloud-Aerosol-Water-Radiation Interactions
IFS	Integrated Forecast System
IR	InfraRed
L2	Level 2
L3	Level 3
LIDAR/Lidar	LIght Detection And Ranging
MODIS	Moderate Resolution Imaging Spectroradiometer
MPEF	Meteosat Product Extraction Facility
MSG	Meteosat Second Generation
NRT	Near Real Time
NWP-SAF	Numerical Weather Prediction - Satellite Application Facility
OCA	Optimal Cloud Analysis
OPE	Operational
PSD	Particle Size Distribution
PUG	Product User Guide
QC	Quality Control
RAL	Rutherford Appleton Laboratory
RGB	Red Green Blue
RTTOV	Radiative Transfer for TOVS
SAF	Satellite Application Facility
SEVIRI	Spinning Enhanced Visible and Infrared Imager
SSP	Sub Satellite Point
TOVS	TIROS Operational Vertical Sounder
WV	Water Vapour

3 DATA RECORD SUMMARY

The details about the theory of the retrieval algorithm are given in the Algorithm Theoretical Base Document (ATBD) (EUMETSAT, 2016).

The retrieval consists of the following steps:

- 1) Initial Guess based on presumption of single layer model
- 2) Cost Minimization: Levenberg-Marquardt algorithm, with phase switching
- 3) Multi-Layer detection:
 - a) initial guess based on presumption of two-layer model;
 - b) cost minimisation: Levenberg-Marquardt;
 - c) post processing of retrieved parameters to two-layer state.

OCA inputs consist of the visible and infrared observations from the SEVIRI instrument, model data and a cloud mask information, all at pixel level. The output consists of cloud phase (CPH), top pressure (CTP), Optical Thickness (COT) and Particle Effective Radius (CRE) for each cloudy pixel, together with uncertainty information. A detailed description of the algorithm including all inputs and outputs is provided in the Product User Guide (PUG) (EUMETSAT, 2021).

3.1 Spatial and temporal coverage

The OCA algorithm derives cloud properties from images of the SEVIRI instrument on-board the MSG satellites. The OCA Release 1 provides four-hourly products for the full Earth disk. The retrieval is done at full spatial resolution, with a nominal pixel size at sub satellite point of 3km. Due to normal operation changes (satellite maintenance) of the prime satellite, few products are generated using the current backup platform. For this reason some products are generated at SSP of 3.4 degrees west and others at 9.5 degrees East (see Figure 1). The information about the current SSP is not included in the product in this release, but the correct area in latitude and longitude is considered. The products cover a region of about 65 degrees radius around the SSP listed in Table 1. The spatial coverage is given in Figure 1.

Table 1: Satellite, instrument, mission, nominal orbit position and services for the period 2004-2019. The period includes Meteosat 8-11 (MSG).

Satellite	Instrument	Mission (SSP)	Start Date	End Date
Meteosat-8	SEVIRI	0DEG (0°)	2004-02-21	2007-05-31
Meteosat-9	SEVIRI	0DEG (0°)	2007-05-01	2013-04-30
Meteosat-10	SEVIRI	0DEG (0°)	2013-04-01	2018-02-20
Meteosat-11	SEVIRI	0DEG (0°)	2018-02-21	2019-08-31

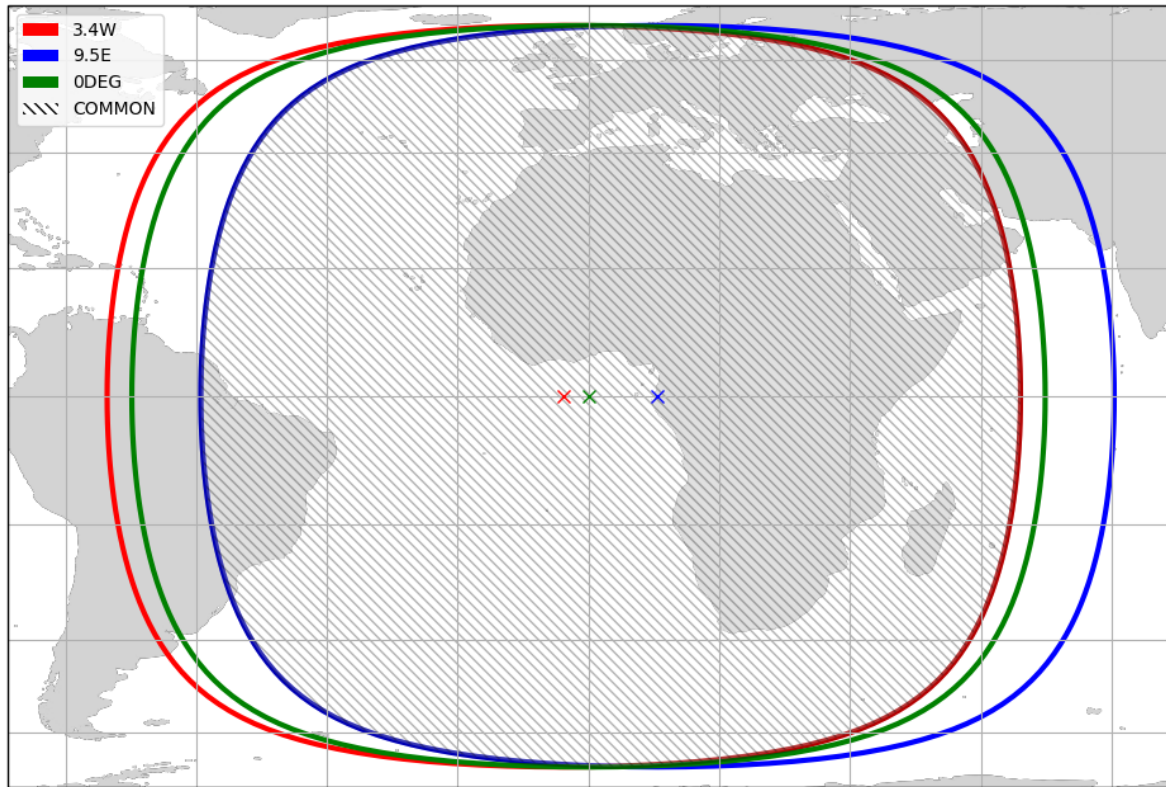


Figure 1: Spatial coverage of Meteosat SSP at 0° exploited for OCA up to 65 degrees. The area covered also by the backup platforms at 3.4W and at 9.5E are shown. The common retrieved area along the whole data record time coverage is also shown.

4 DATA USED FOR THE VALIDATION

To validate and verify the quality of the OCA Release 1 retrievals we used several different products ranging from independent observations to retrieval products from other instruments on-board both geostationary and polar-orbiting platforms.

The main source for providing independent measurements for the validation of cloud properties is the A-Train constellation and in particular the active measurements from the CloudSat radar and Cloud-Aerosol Lidar and Infrared Pathfinder Satellite Observations (CALIPSO) lidar. The main source for comparing OCA cloud properties against retrievals from other passive imager algorithms were the Moderate Resolution Imaging Spectroradiometer (MODIS) Level 2 (L2) and Level 3 (L3) products and the SEVIRI The CLOUD property dataset using SEVIRI, Edition 2.1 (CLAAS 2.1), two well tested and validated cloud property data records. All the data used in this validation report will be described in the following sections.

4.1 DARDAR

The raDAR/liDAR (DARDAR) algorithm (Delanoë and Hogan, 2008, 2010) combines in a variational algorithm data from spaceborne radar, lidar and infrared radiometers for cloud phase identification and the retrieval of ice clouds properties. The algorithm is applied to the instruments on the “A-Train” of satellites which includes CALIPSO (Winker et al., 2003) carrying a nadir-viewing two-wavelength (532 and 1064nm) polarization-sensitive lidar, CloudSat a 94 GHz cloud profiling radar (Stephens et al., 2002), and AQUA platform carrying the MODIS instrument (King et al., 1992).

The synergistic use of different instruments to retrieve the microphysical properties of ice clouds allows to combine the strengths of each instruments. Radars are less sensitive to small particles than lidars, but the latter are more sensitive to optically thin clouds and tend to be strongly attenuated by thick cloud layers. Moreover, radar and lidar backscatter depends on different moments of the cloud Particles Size Distribution (PSD) so that their combination provides a more complete retrieval of the cloud profile. Radar returns in Rayleigh scattering regime are proportional to the sixth moment of the PSD, hence to the largest particles while lidar backscattering is more sensitive to the particles cross section and number concentration being therefore proportional to the second moment of the PSD. DARDAR is able to retrieve seamlessly the cloud properties between areas where one or more instruments are available by the use of all available measurements and empirical constraints in an optimal estimation framework.

For the definition of the horizontal grid, DARDAR is geo-located using the CloudSat 2B-GEOPROF product³ as reference on a 1km grid. This means that radar measurements are interpolated and lidar measurements averaged to the final grid (on average three lidar beams per footprint). For the vertical grid a resolution of 60 meters is employed to re-grid both radar and lidar products.

Given the capability of OCA retrievals to distinguish between single and multi-layer situations, DARDAR allows us to explore, in a fine vertical grid, the complete view of the vertical profile of a cloud layer. In this validation report we used the DARDAR feature mask and retrieval as

³ Link valid on 16/02/2022: <https://www.cloudsat.cira.colostate.edu/data-products/2b-geoprof>

the main reference for defining single and multi-layer cloud profiles, cloud phase, cloud top height of up to three overlapping cloud layers. To account for the different sensitivity to thin cloud layers between lidar and passive radiometers, we processed the DARDAR feature mask to improve the likelihood that both instruments were observing the same cloud layer (see Section 5.1).

The DARDAR data were retrieved from the ICARE⁴ archive, which comprises the A-Train retrievals for the period 2006-2017. These data do not cover the whole period, because starting from September 2011 the CloudSat instrument has been working during daytime only. This affected from 2012 onwards, the DARDAR product and the collocations with SEVIRI that were derived using CloudSat as reference for the geolocation of A-Train products. In order to keep the computational load of the data processing reasonable, three days per month with one daytime and one nighttime orbit per day (when available) were analysed. The chosen days are always about 10 days apart, around the 1st, the 10th and the 20th of the month, depending on their availability. The analysed DARDAR granules cross the SEVIRI disk around 2am UTC and 3am UTC for the night overpasses and between 1pm UTC and 2pm UTC for the daytime overpasses. The selected DARDAR granules are close to the central part of the SEVIRI disk to facilitate the comparison between the instruments by excluding too large viewing angles to the East and West of the MSG sub satellite point.

For the collocation between SEVIRI and A-Train observations including parallax correction, we used the A-Train Validation of Aerosol and Cloud Properties from SEVIRI (AVAC-X) software an updated version its precursor, AVAC-S, that was adapted to work with generic geostationary satellites (Bennartz et al., 2010). AVAC-X uses the CloudSat 2B-GEOPROF file as base for the geolocation and alignment of SEVIRI and DARDAR, CloudSat and CALIPSO L2 products (see section 5.1 for more details).

4.2 CALIPSO L3 GEWEX cloud top product

This gridded dataset is based on CALIPSO L2 cloud products and produced for the Global Energy and Water Cycle Experiment (GEWEX) Cloud Assessment⁵. The L2 products aggregated on a 1°x1° grid in a set of monthly files covering the period 2006-2016 and divided into day-only, night-only and day-night retrievals.

Different versions (flavours) of cloud top products are available in each monthly files, suitable for different applications. The two relevant for the present analysis are the “TopLayer” and the “Passive” versions. The former selects only the topmost layer in each CALIPSO profile while the latter restricts the cloud top products to clouds with an optical thickness larger than 0.3, as this is more likely to be sensed by a passive instrument.

4.3 CLAAS 2.1

The time-series consistency and the mean climatological features of the OCA Release 1 CDR were analysed through a comparison against another dataset based on SEVIRI measurements covering the same time span, the CM SAF CLOUD property dAtAset using SEVIRI - Edition 2 (CLAAS v2.1) dataset (Finkensieper, Stephan et al., 2020). This dataset contains retrieved

⁴ Link valid on 04/05/2022: <https://www.icare.univ-lille.fr/>

⁵ Link valid on 04/05/2022: https://www-calipso.larc.nasa.gov/resources/calipso_users_guide/qs/cal_lid_l3_gewex_cloud_v1-00.php

cloud properties from inter-calibrated measurements of SEVIRI on-board the MSG satellites MSG-1, MSG-2 and MSG-3 covering the period 2004-2017. The EUMETSAT Satellite Application Facility on Climate Monitoring (CM-SAF, <http://www.cmsaf.eu>) produces the dataset.

The CLAAS v2.1 was generated using are the MSGv2012 software package of the SAF for support to Now casting and Very Short Range Forecasting (NWC-SAF) for the cloud fraction and cloud top properties (Derrien and Le Gléau, 2005), and the CPP (Cloud Physical Properties) algorithm (Roebeling et al. 2006) for cloud-top thermodynamic phase, cloud optical thickness, cloud particle effective radius, and liquid/ice water path.

In this report, instantaneous OCA Release 1 and CLAAS v.2.1 products of selected SEVIRI repeat cycles were compared to highlight the differences between their Level 2 (L2) retrievals and the differences between their monthly-mean Level 3 (L3) products. The comparison focussed on the cloud microphysics, optical thickness and cloud top pressure.

4.4 MODIS L3

We compared OCA retrievals to the products from the MODIS (King et al., 1992) as cross comparison between cloud properties retrievals from passive radiometers using similar spectral channels but different platforms. The MODIS instrument flies on-board the TERRA and AQUA satellites, both on a polar sun-synchronous orbit with equatorial crossing times respectively of 10:30am in descending direction and 1:30pm local solar time in ascending direction.

For the following evaluation, we used the gridded MODIS L3 datasets to compare the OCA CDR over the whole SEVIRI reprocessing period 2004-2019 (see Section 6.1). The L3 TERRA *MOD08_M3*⁶ and L3 AQUA *MYD08_M3*⁷ collection 6.1 files contain monthly-means clouds, atmosphere and aerosol retrievals parameters on a 1°x1° grid and for the whole globe. We averaged the retrievals from TERRA and AQUA in order to obtain a slightly more accurate daytime average using both the morning and afternoon equatorial crossing times. The sparse temporal sampling tends to bias the day time MODIS product towards being representative of the local solar time, especially for the region between 23° N and 23° S. Poleward of these latitudes L3 data slowly become an average of several orbits roughly 100 minutes apart and poleward of 77° this leads to an effective daily average (see the MODIS L3 ATBD for more details, Hubanks et al., 2020).

Based on a similar set of channels, MODIS and OCA products do differ somewhat not only due to the different spatial resolution, temporal resolution (Table 2) and the larger number of channels available in MODIS, but also due to the different retrieval approach for the same cloud parameters (see e.g. Platnick et al., 2017 and references herein for an overview of the core MODIS Cloud Products algorithms).

Table 2: summary of the main differences in spatial and temporal resolution between L2 and L3 retrieval products from OCA-SEVIRI and MODIS. OCA is provided to the users at the native SEVIRI resolution of 15 minutes (Level 2). The aggregation to monthly mean (Level 3) has been done for comparison purposes only.

⁶ Link valid 04/05/2022 https://ladsweb.modaps.eosdis.nasa.gov/missions-and-measurements/products/MOD08_M3

⁷ Link valid 04/05/2022 https://ladsweb.modaps.eosdis.nasa.gov/missions-and-measurements/products/MYD08_M3

	L2 products resolution		L3 products resolution	
	Spatial	Temporal	Spatial	Temporal
OCA	3 km at nadir	15 minute	1°x1°	Monthly mean from 7 observations/day (hourly from 09Z to 15Z)
MODIS	1 km at nadir	Twice daily at low/mid latitudes	1°x1°	Monthly mean from roughly one observation a day at low to mid latitudes

MODIS cloud top height retrieval is based on a CO₂ slicing technique using several channels located in the broad CO₂ 15 μm absorption band only one of which is available with SEVIRI. Furthermore, although MODIS is able to identify overlapping cloud layers, these cases are still treated as single-layer clouds. The MODIS retrieval of cloud microphysics benefits from two extra (daytime only) near-infrared channels at 2.1 μm and 1.2 μm for cloud detection. Unlike the MODIS algorithm, OCA attempts a continuous retrieval of the microphysics properties for both daytime and nighttime conditions.

5 VALIDATION STRATEGY

5.1 Comparison against A-Train CloudSat and CALIPSO measurements

The comparison with A-Train measurement is done using the EUMETSAT A-Train Validation of Aerosol and Cloud (AVAC-X) software, briefly introduced in Section 4.1. AVAC-X provides the full collocation and parallax correction of SEVIRI-based retrievals and A-Train products.

The geolocation of the CloudSat provides AVAC-X with the master information to select the relevant SEVIRI pixels closest to the surface Field of View (FoV) of the relevant A-Train product, with a temporal tolerance for the collocation set to 7.5 minutes. AVAC-X provides the A-Train products either averaged over the SEVIRI pixel or for the nearest profile to the SEVIRI grid box. We used the nearest profile for discrete products, such as the DARDAR feature mask, and for consistency the nearest profile was also used for the other DARDAR products. The main conclusions of this validation do not depend on this choice and using the DARDAR products averaged over a SEVIRI FoV brings differences of less than 6% for COT and less than 1% for CTH and CRE.

Given the capability of OCA to retrieve cloud information for overlapping cloud layers, this validation used a combination of CloudSat and CALIPSO measurements to identify the presence of multiple cloud layers and the top height/pressure of up to three layers. We used primarily the cloud classification and cloud properties retrievals from the DARDAR algorithm together with the backscattering profile from CALIPSO.

It can be difficult to define uniquely a multiple cloud layer situation since this can depend on the type of instrument and its sensitivity to the signal coming from the different cloud layers. The DARDAR cloud feature mask was used to objectively identify multiple overlapping cloud layers. In particular, the DARDAR classification is used to determine the number of cloud layers for each CloudSat and CALIPSO profile that was collocated with a SEVIRI. A valid cloud layer is assigned when two-layers are at least 1000m apart and have a geometrical thickness of at least 600m. This helps reducing the ambiguous cases linked to a noisy backscatter profile from the instruments and identifies situations of radiative and meteorological significance.

This first classification step selects the pixels with higher probability of overlapping cloud layers. The second step detects thin cloud layers taking into account the higher sensitivity of the lidar with respect to a passive radiometer. A set of 184 A-Train granules over the SEVIRI disk during three years (2007-2009) was used to compare the frequency of two-layer situations detected by OCA and by DARDAR as function of the separation between the layers and the visible optical thickness of the top layer. The optical thickness of the uppermost layer, scaled by the SEVIRI view angle to allow for a better comparison with the optical path seen by OCA, is computed for ice clouds from the extinction profile at 550nm retrieved by DARDAR. In rare cases, the upper layer of a multi-layer situation is of type liquid water (~5% of all two-layer cases on average), for which the extinction from DARDAR is not available. For these cases, the extinction profile was estimated from the Cloud Physics Lidar (CPL) backscatter, assuming a constant Lidar factor of 20 *sr* and an empirical adjustment for multiple scattering (Platt 1973) with a correction factor *n* equal to 0.7. Figure 2 shows that OCA detects most multi-layer situations for a wide range of cloud layers separation when the optical thickness of the upper layer is larger than about 0.3 and up to about 5. The Lidar/Radar system is able to detect, with

significant larger frequency, layers with an optical thickness down to less than 0.1. In order to reduce the number of ambiguous situations, we decided to only assign cases with overlapping cloud layers in case the topmost layer has an optical thickness between 0.3 and 5.

Limitations in the use of this multi-layer identification have to be taken into account in the interpretation of the validation results. In particular, the reliability of the technique is low for more complex multi-layer profiles, such as those with deep and broken convective clouds, multiple/mixed cloud phases, aerosol layers, or with non-homogeneous cloud cover within the SEVIRI gridbox concerned.

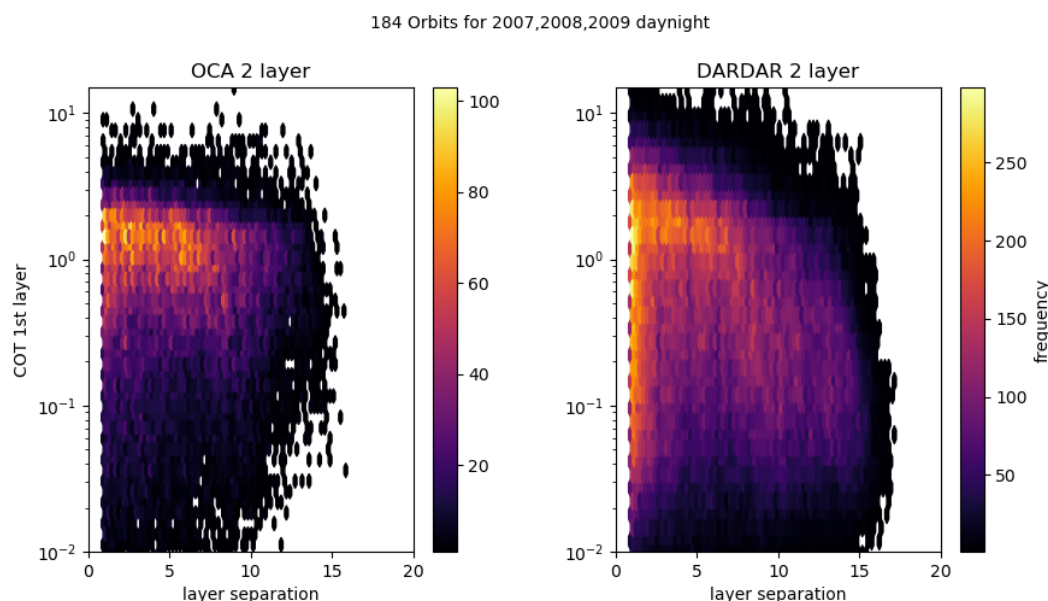


Figure 2: Frequency of detection for multi-layer pixels as function of the cloud layers separation (in km) and optical thickness of the topmost layer. Left: multi-layer pixels, as defined by DARDAR, also detected by OCA. Right: multi-layer pixels detected by DARDAR. Excluded are cases where the cloud top height of the second layer differs by more than 7 km between OCA and DARDAR, indicating high likelihood that the instruments measured different parts of the cloud.

Figure 3 and Figure 4 show an example of a section of an A-Train orbit crossing the SEVIRI disk on the 1st of June 2007. The MODIS true colour RGB (Figure 3) shows a complex area of high and low clouds associated to a frontal system to the south and low stratocumulus to the north, off the western coast of South Africa and Namibia. The DARDAR cloud feature mask (Figure 4) shows a thick ice cloud at the beginning of the section followed by a situation with a thinner ice cloud in the upper layer and broken liquid clouds below. Finally, a section with low liquid clouds with some aerosol dominates the rest of the scene. The DARDAR algorithm uses this information to define the top of up to two cloud layers per profile, which will then be used to evaluate the retrieval from OCA. The cloud top pressure from OCA is converted to cloud top height using the ECMWF model meteorological data associated to the selected A-Train profile. An example of this comparison is shown in Figure 5. The upper panel shows the profiles found for a single layer cloud only. These are found mostly in thick ice clouds or in the low liquid water clouds. The second and third panels show the top of the upper and lower cloud layers respectively, for profiles with overlapping clouds. In the case of multiple layers, the comparison shows that OCA tends to switch to the two-layer retrieval more often than DARDAR (orange points in the first panel) and that the bias in the cloud top retrieval between

the two remains similar to the one seen in the single layer case when the profile is identified as multi-layer by both OCA and DARDAR. In the case where DARDAR identifies a multi-layer profile and OCA uses the single-layer retrieval (orange points in the second panel), the placement of the cloud top shows larger errors.

The figure confirms the difficulty of unambiguously defining the position of the multiple layers in a pixel, especially in vertically complex cloud profiles (e.g. at position 52S,20E).

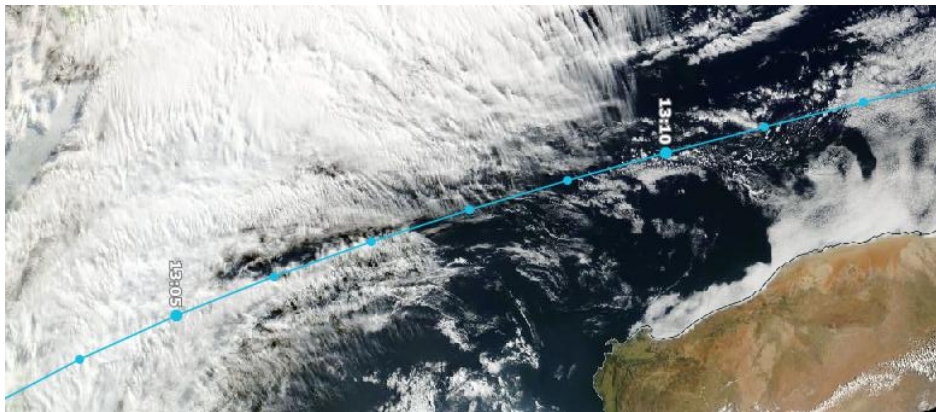


Figure 3: MODIS true color RGB image of the scene analysed in Figure 4 and Figure 5. The blue line shows the track of AQUA ascending orbit. The image is rotated by 90° and the left side is at 57S latitude, the right side at 22S latitude.

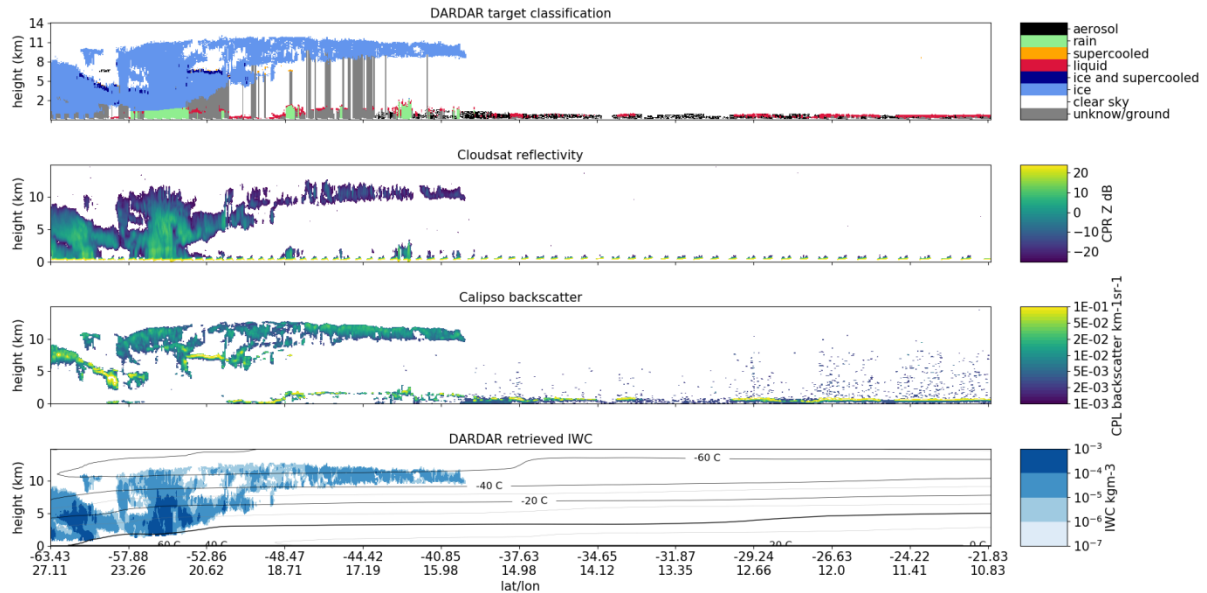


Figure 4: Section of an A-Train granule extending from 63.4S-27.1E to 21.8S-10.8E on the 1st of June 2007. The three panels show from the top: DARDAR cloud feature mask, CloudSat reflectivity, CALIPSO backscatter and DARDAR retrieved ice water content. In the lower panel, the contour lines show the temperature from the corresponding ECMWF forecasts.

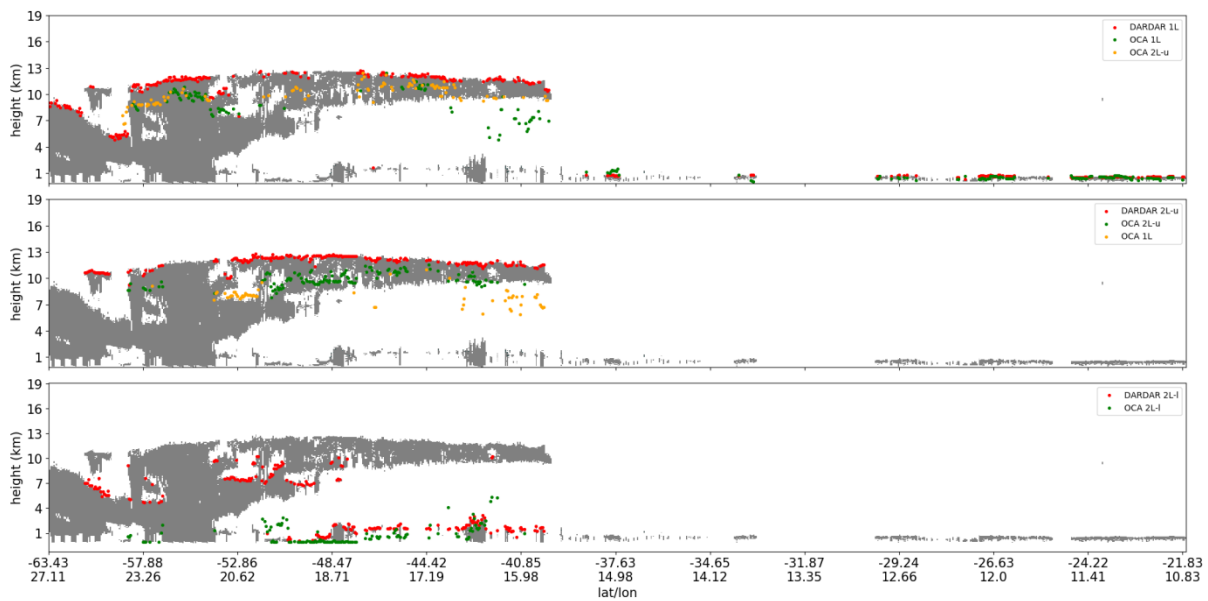


Figure 5: Example of identification of cloud tops from DARDAR and CALIPSO data for the granule section of Figure 4. Red dots show the cloud top inferred from the A-Train data, green dots show the OCA cloud top where the identification of single or two-layer agrees with the one from DARDAR data. The top panel shows the cloud top for single layers only, middle panel the cloud top of the upper layer of two-layer profiles and lower panel the cloud top of the second layer of two-layer profiles. The orange dots in the first two panels show where the identification from OCA does not agree with DARDAR: this means OCA two-layer in the first panel and OCA single layer in the middle panel.

5.2 Comparison against MODIS and CLAAS 2.1

In order to cover the full time span of the OCA Release 1 CDR and maintain the processing to a manageable size, we compared against monthly mean products from MODIS and CLAAS 2.1. Furthermore, all products were re-gridded to the common $1^\circ \times 1^\circ$ grid of the MODIS L3 dataset. The details of the creation of spatial and temporal averaged OCA data is explained in Section 6.1.

Cloud top retrievals are available as day and night retrievals for all datasets. The MODIS and CLAAS 2.1 cloud microphysics retrievals are available during daytime only, while OCA provides cloud properties retrievals during day and nighttime. We therefore, as outlined in Section 6.1, only considered the daytime values in the monthly aggregation of OCA retrievals by selecting only the repeat cycles between 9Z and 15Z: this ensures that most of the SEVIRI disk is in daylight, although part of it will still include portion of nighttime retrievals. A discussion on the quality of nighttime products using the collocated retrievals from DARDAR can be found in section 7.1.

To reduce the impact of the residual nighttime retrievals on the disk averages, these have been restricted to regions inside the area covered by a maximum SEVIRI viewing angle of 50° . This also helps excluding areas of more extreme viewing angles where the retrieval uncertainty grows larger. To remove the data with the largest uncertainty we only used the retrievals for which the final cost function and the retrieval errors for the cloud top pressure are respectively less than 900 and 90 hPa. The thresholds are low enough as to block the worse retrievals but large enough as not to cause a rejection of too many pixels. These are about 5% at nighttime and 15% at daytime. Finally, to avoid using monthly averages over areas with few valid

retrievals, pixels with less than 20 valid daily means per month from OCA and CLAAS 2.1 were rejected.

The comparison of cloud top pressure and cloud optical thickness is done for combined liquid and ice cloud phases, while we stratified the cloud effective radius by cloud phase. This has been done in the following way for the three datasets:

- For the OCA monthly mean only the combined values are available and the percentage of two-layer, ice water and liquid water clouds is used to select the cloud type that dominates the pixel. The chosen fractions for the category liquid water clouds and the category ice water plus two-layer clouds are 0.5 and 0.4, respectively. The categories ice water and two-layer clouds were combined because OCA defines the uppermost layer of two-layer clouds as ice clouds always. The fraction for the liquid water category is larger than for the ice category to account for the fact that liquid water clouds have a larger percentage in absolute.
- For the MODIS L3 ice and liquid cloud products, the `Cloud_Retrieval_Fraction_Liquid_FMean` and `Cloud_Retrieval_Fraction_Ice_FMean` were used to filter out areas dominated by one of these cloud types. Note that MODIS fractions have a different meaning than OCA fractions, because the first include statistics of successful retrievals. We used fraction thresholds of 0.3 and 0.2 to select pixels dominated by liquid water and ice water clouds, respectively. The threshold for the ice clouds is lower because of the lower overall frequency of that phase.
- For CLAAS 2.1 we used the ice and water category products that come with the L3 datasets. Similar to the other two datasets, areas with low frequencies of each phase were taken out. However, in this case we used the variable `nobs` (number of daily means available in the monthly mean files), which is available separately for the ice and liquid products. Finally, consistent with the OCA monthly aggregation, we used a threshold of minimum 20 days of valid daily means per month.

6 OVERALL EVALUATION

In this section, the OCA CDR is analysed in terms of self-consistency showing that the data record does not include unexpected gaps and that it is stable and homogeneous in time. The key retrieval variables of cloud properties are plotted and are shown for the complete spatial and temporal coverage. For this purpose, L2 OCA products were aggregated to daily and monthly means and re-gridded to a 1-degree resolution (see Section 6.1). Hovmöller diagrams, covering the full period, have been then produced from these aggregate files to provide a robust overview of the data record behaviour over the complete time-series.

Firstly, a time-series for all slots, i.e. without spatial-temporal aggregation, is shown to provide a simple qualitative overview of the whole processing. The plots consider the different cloud phases (one-layer water, one-layer ice and two-layers). Figure 6 shows this time series of the averaged daily cloud properties computed using all available SEVIRI images (slots). It shows that even using four SEVIRI instruments on-board different Meteosat satellites, the retrieval is homogenous without steps or bias introduced by the swap between the satellite. Some outliers/spikes are visible as the one at the end of 2008 (zooming it will show a sinus-shaped form). They are mainly related to the cloud mask input (because for some images the infrared 10.8 channel was not available). The mask, only bases on VIS observations, will include during the course of the day only those pixels visible according to the daily sun illumination. A CDR products blacklist covering this and other known issue is provided to the users. Similar time series for a particular time at day (0UTC) and night (12UTC) are presented in Appendix A.

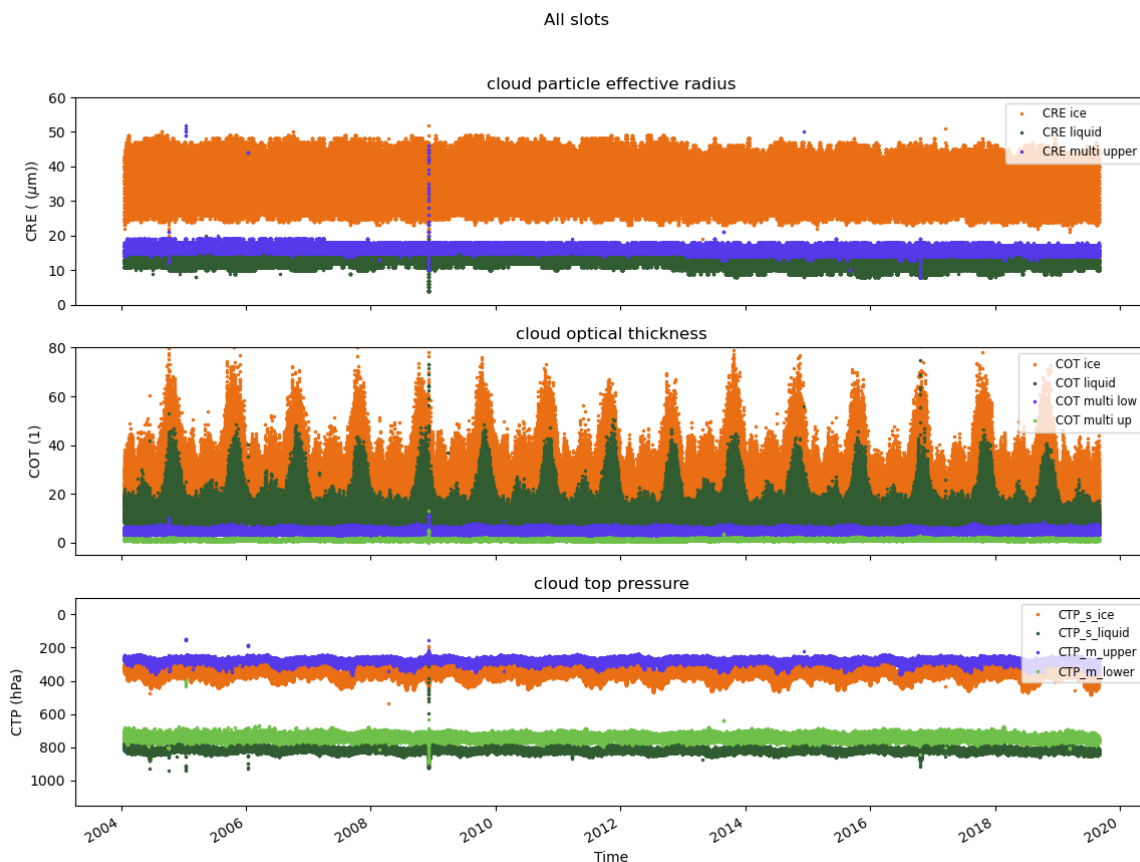


Figure 6: Time series for the average daily cloud properties computed using for all available slots of that day: CRE (upper panel), COT (middle panel) and CTP (bottom panel). The plots distinguish among the cloud phases.

6.1 OCA daytime temporal analyses

6.1.1 Daily and monthly aggregation

Daily files on a grid of 1-degree resolution are created using daylight hourly products from 09:00 to 15:00 UTC (seven products/day). The aggregation is done for observations in the range $[-60^\circ, 60^\circ]$ to limit the inclusion of pixels with a too high zenith angle. Therefore, they can be defined daylight aggregation products. This choice has been made for two reasons: (a) to better compare against MODIS products, which only contain daytime microphysics retrievals; (b) to avoid including false and unrealistic cloud optical thickness retrievals at nighttime over specific region, such as the Sahara Desert, in the space/time aggregated files. A diagram of the impact of these wrongly retrieved COTs is shown in Appendix B. The same section also shows that no artefact due to night time retrieval is present for the CTP and CRE products. A 1-degree box is filled with an average value if at least 20% of the pixels in the box have been retrieved. This has the objective avoiding upscaling grid points without a significant sampling. Two further sets of variables are calculated. One using all available retrievals and one (quality controlled or QC) only containing the OCA retrievals fulfilling some requirements for the estimated uncertainty and cost functions (same thresholds as explained in section 5.2). The impact of such operation is evident in OCA products but it tends to become insignificant on moving to 1 degree daily and monthly aggregation. From the daylight aggregation files, a monthly aggregation file is created. A mask for each grid point, containing the ratio between the days with a retrieval and the number of days in the month, is stored. For instance, if a grid point in June 2005 (containing 30 days) comprises three daylight values, the value of the mask is 0.1 (10%) for that grid point. This mask can be applied to all monthly averaged stored variables to assess the effect of sampling in the overall average. For example, if applied to CTP it will help removing the unrealistic values over bright desert areas. The number of pixels with a cloud retrieval per each box is highest in the tropical belt and decreases towards the poles (see Figure 7). This is to be expected considering, as a 1-degree box contains more pixels close to the sub satellite point of an image from a geostationary platform such as SEVIRI.

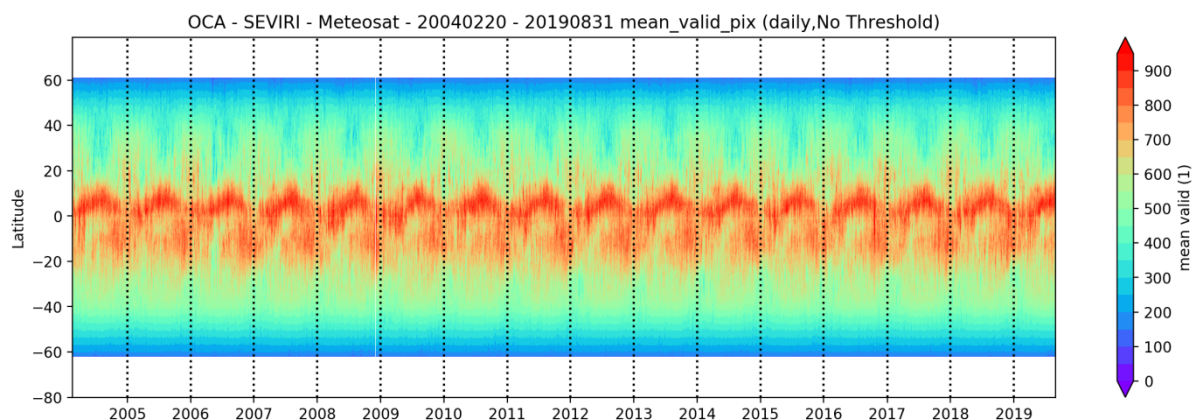


Figure 7: Hovmoeller diagram daily mean number of valid retrieval in each 1 degree box. A box is filled with a value if at least 20% of the pixels have been retrieved.

The number of valid mean daily retrieval in a month shows a minimum in the area around 25° north and 20° south due to the seasonal lack of clouds in those regions (see Figure 8). Note that the time series is smooth and the changes of SEVIRI instrument on-board the four MSG satellites do not appear on those time series.

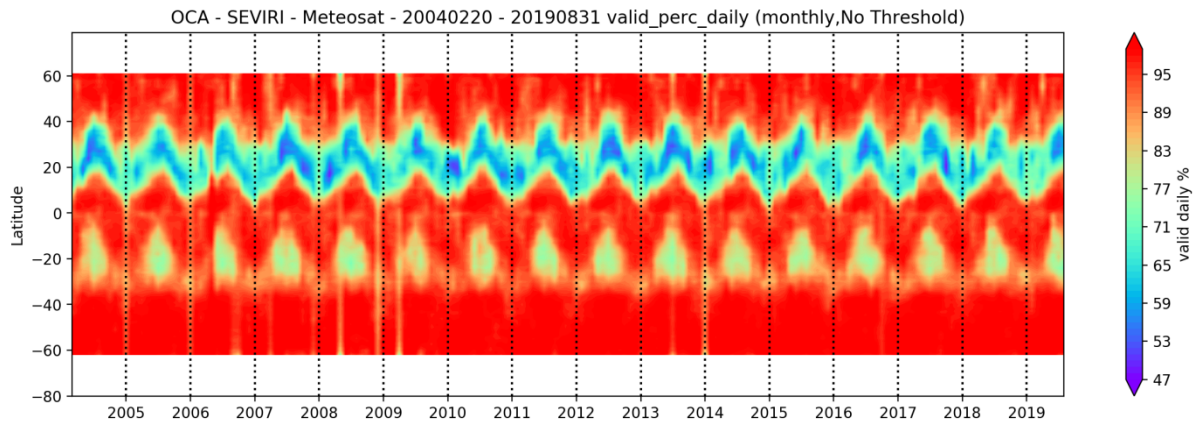


Figure 8: Hovmoeller diagram of the zonal mean (+60°-60°) of monthly percentage of available days.

6.1.2 Daily and monthly cloud properties

In Figure 9, the zonal averaged CTP over the latitude range -60° to +60° is shown without any filtering (upper panel) and with filtering using a 60% cloud retrieval threshold (lower panel). The impact is visible even if not so pronounced. This result is in line with the values shown in the daily (Figure 13) and monthly map (Figure 15). The average over longitude bands is not affected by decreased number of samples in the same value range (wrongly assigned low-level clouds) over the desert areas. The CTP time series is homogeneous and smooth over the period and does not exhibit any changes linked with changes in SEVIRI instruments. We clearly see the stratus and cumulus clouds at about 20° latitude. There is a clear seasonal cycle showing more low clouds over the south 20° band going from about 850 hPa in June to 700 hPa in January. Over the Tropics, the averaged CTP is higher located at about 500hPa. At higher latitudes above 40°, the time series do not show any clear seasonal cycle and the zonal averaged CTP over the 60/60° bands is about 650 hPa. A more detail evaluation of the CTP, presenting the comparison with other passive-imager cloud climatologies is given in section 7.2.1. In conclusion, the OCA Release 1 CDR retrieval of CTP is in line with the expected CTP averaged seasonal cycle.

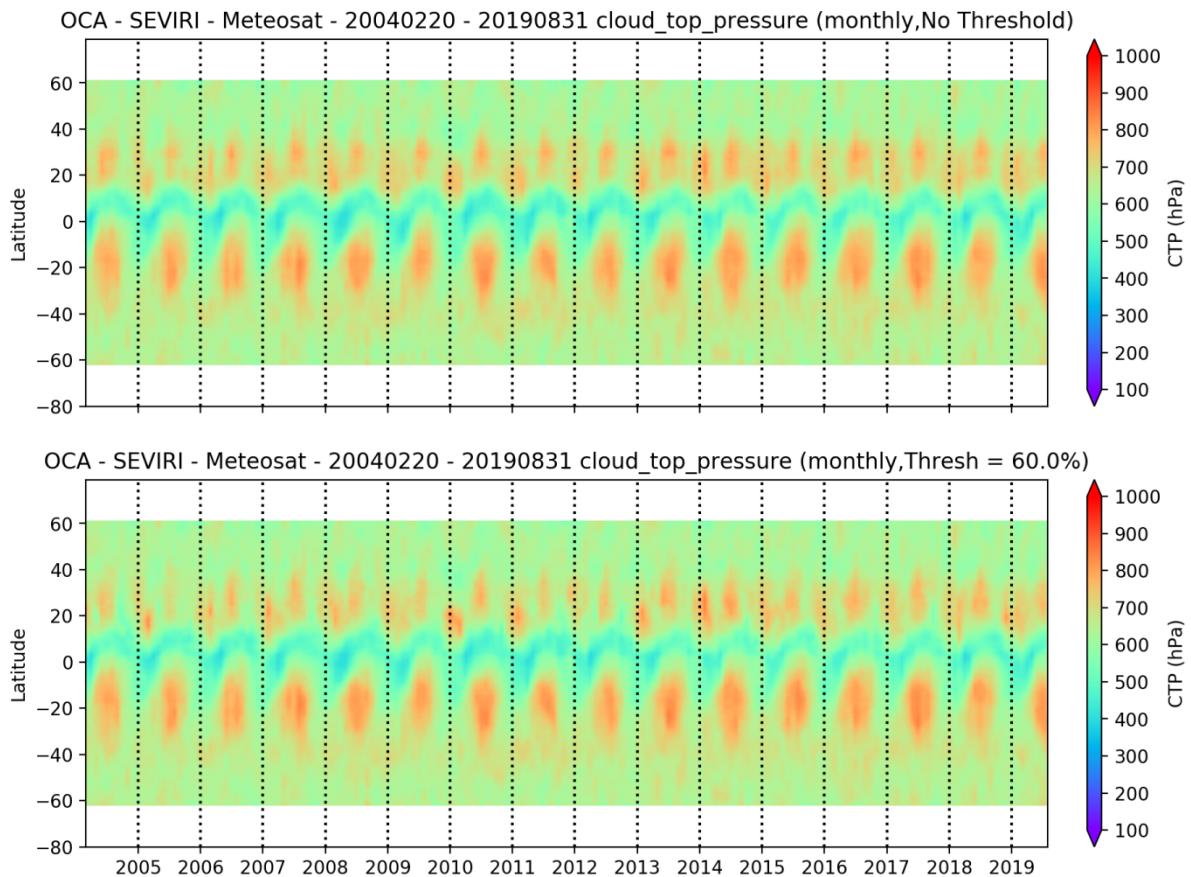


Figure 9: Hovmoeller diagram of zonal mean ($+60^{\circ}$ to -60°) monthly cloud top pressure (hPa). Upper panel includes all data; lower panel includes only filtered data using a threshold at 60% (lower panel).

For each cloud retrieved by OCA, a cloud type is associated. Three types are possible, i.e., a one-layer ice cloud, a one-layer water cloud, or two-layer clouds. Note that in case of a two-layer clouds the OCA assumes the ice phase for the uppermost layer while no phase is specified for the underlying layer. The averaged fraction of each of the three available cloud types is shown in Figure 10. It is very interesting to observe the behaviour in time of the fraction of each cloud type. The one-layer water clouds clearly dominate (about 60% of the cases), followed by the one-layer ice clouds (about 30% of the case). The least occurring cloud type in OCA are the two-layer clouds with a fraction of about 20%. The distribution is very constant during the whole period, and shows clear seasonal variations. Also, the figure shows clearly that the most common case is the one-layer water, followed by the one-layer ice. The two-layer case is the least frequent. Figure 10 confirms the OCA cloud type retrievals are homogeneous over latitude zones and stable in time.

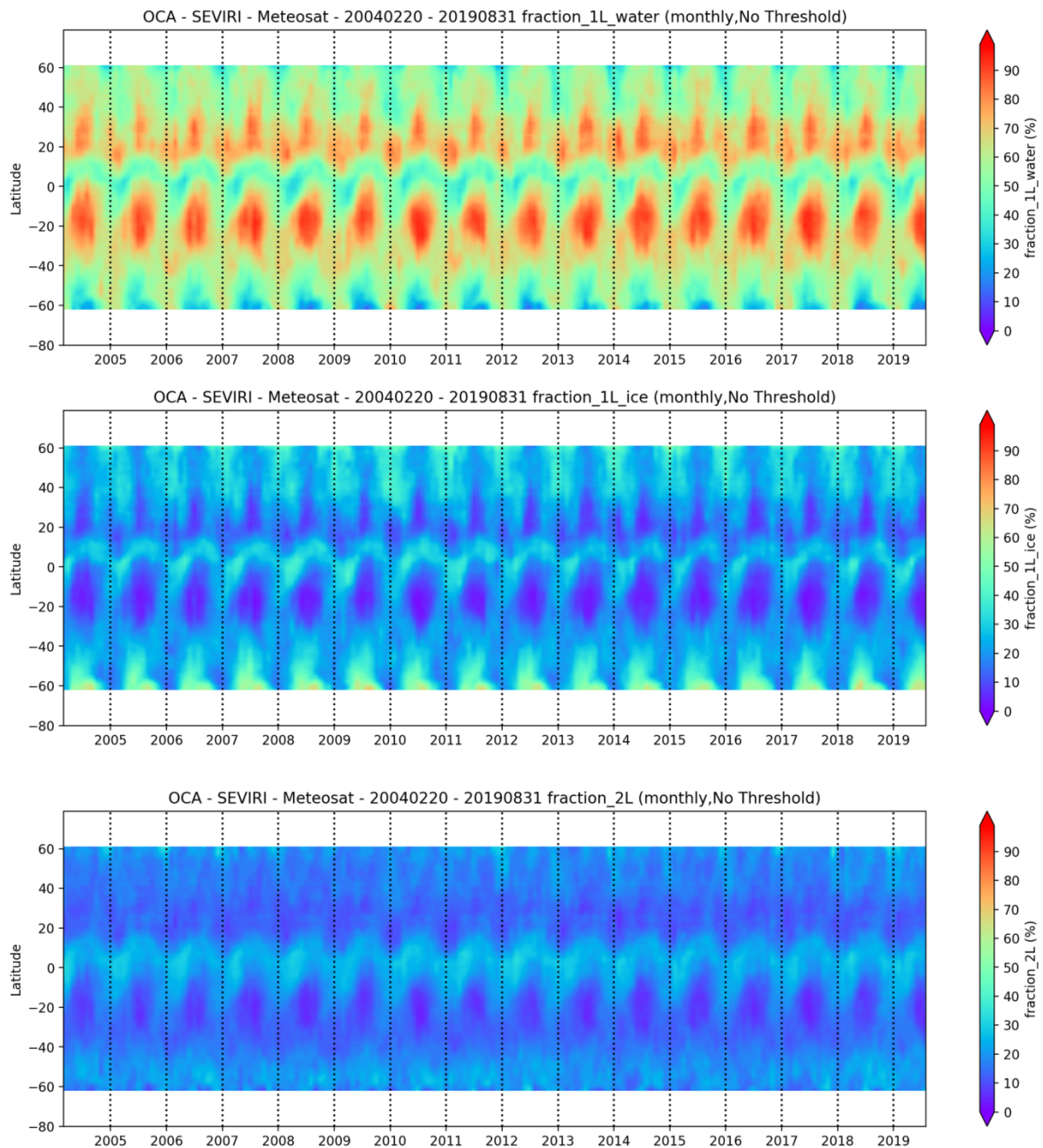


Figure 10: Monthly Hovmoeller diagrams of the zonal mean of the cloud type fraction of one-layer water (upper panel), one-layer ice (middle panel), two-layers (bottom panel). The values are averaged over 1-degree box and over a month. So the total for all cases is not expected to be 100%. No threshold on the available number of days per month is applied.

Finally, the zonal averaged over the latitude range -60° to $+60^{\circ}$ for total cloud optical thickness (COT) and for cloud particle effective radius (CRE) are shown (Figure 11). The constant COT's high value at -60° latitude is possibly due to the combination of high viewing angles and difficult to sense surface conditions (such as sea or land ice). The same effect is discussed in Section 7.2.2. The CRE is a key property of clouds governing their radiative transfer. OCA averaged CRE is around $20 \mu\text{m}$. More in-depth analyses of OCA COT and CRE are provided in the section 7.2.2 and 7.2.3.

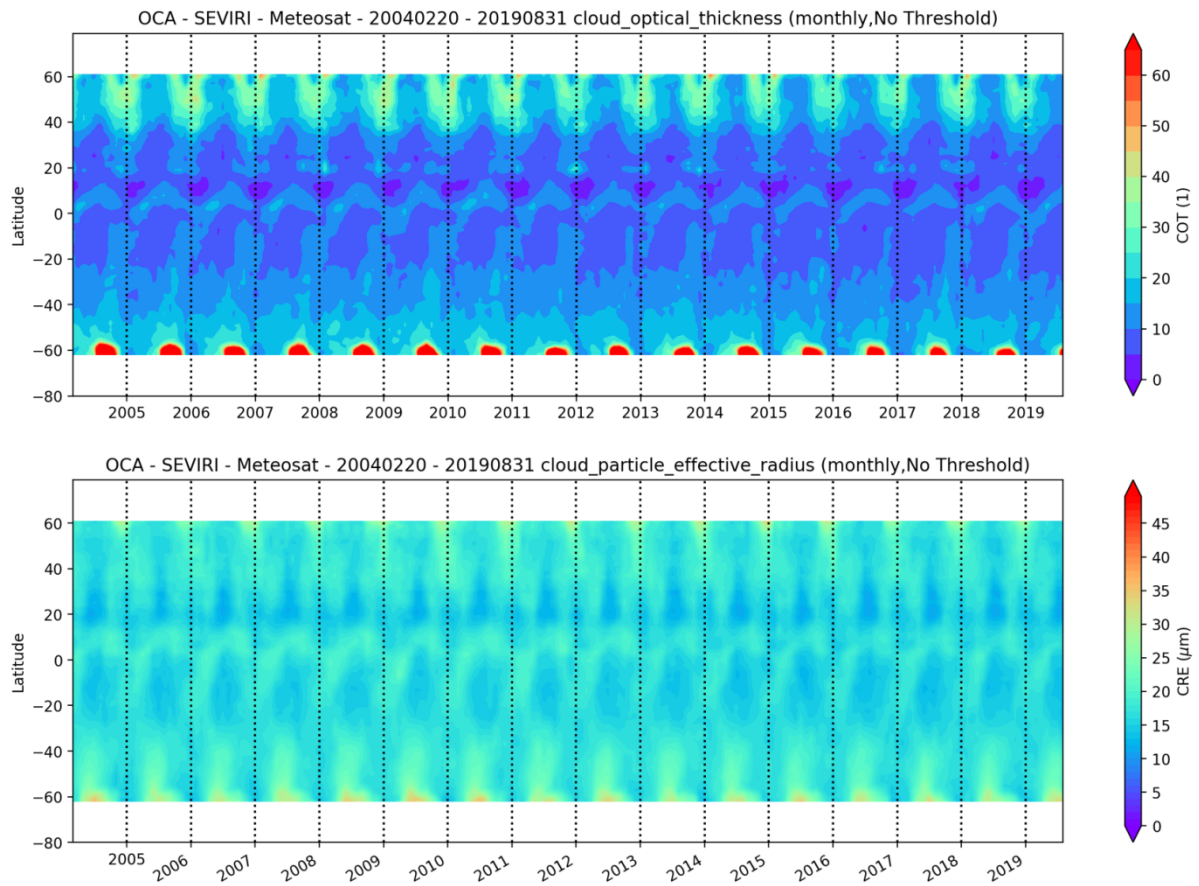


Figure 11: Monthly Hovmoeller diagrams for zonal mean (+60° to -60°) cloud optical thickness (upper panel) and cloud particle effective radius (bottom panel). No threshold on the available number of days per month is applied.

6.2 Example of geographical distribution

The geographical distribution of the OCA cloud properties is shown in the

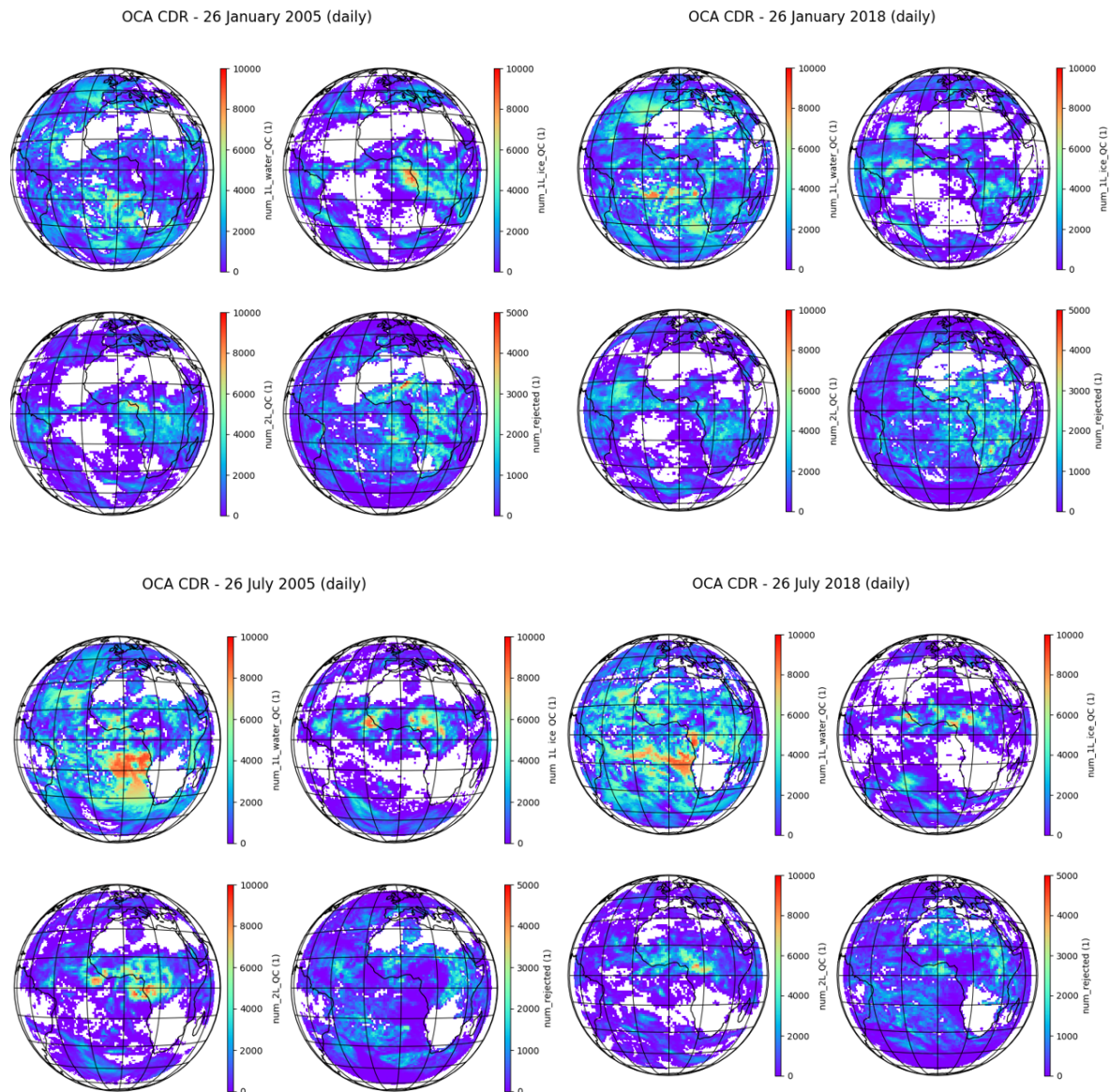


Figure 12 to Figure 15. It gives daily and monthly maps for January and July showing the effect of the quality control threshold (removal of retrievals with high uncertainty) on the data quality. Interesting information about the two-layer retrieval performed by OCA can be acquired looking at the daily number of one-layer (ice and water) and two-layer geographical distribution. This information is transformed into a fractional value when moving to a monthly aggregation.

The daily maps show with high spatial detail the cloud type and properties distribution during a summer time and winter time day (Figure 12 and Figure 13) while the general climatological distribution resulting from the single daily data is observed in the monthly mean figures (Figure 14 and Figure 15).

OCA products shows a good representation of the typical climatology of cloud types for this area of the Planet. We can see that the majority of single layer liquid water clouds are found over the oceans, in the stratocumulus and trade-cumulus region off the west coast of Africa in

the Middle and Southern Atlantic. Ice clouds are associated with high convection in the tropics, where the signature of individual deep convection cells are visible in the daily average. Mixed liquid and ice clouds can be found most often in the mid-latitudes storm track. Two-layer clouds follow generally the area where mostly ice clouds are found as this is where more likely an ice cloud can overlap cloud layers below.

We can also see that a significant amount of pixels rejected according to the quality control filters discussed in section 5.2 appear both over land and over water, often in areas of complex overlapping cloud conditions and challenging surface properties such as over deserts or in the vicinity of large convective systems.

The properties of these clouds as retrieved by OCA reflect their typical physical characteristics. Generally high cloud with low top pressure are associated with ice crystals with larger size of order of 30 microns while lower liquid water clouds have droplet size of less than 20 microns. The largest values of cloud optical thickness are found within deep convective systems and frontal systems in the mid latitudes. We can observe that there is the tendency for OCA to overestimate the amount of low level clouds over the deserts, which is visible in the daily and monthly averages. The reason for this feature is discussed more in detail in section 7.2.1.

Finally, on a monthly average scale the areas with the least number of usable products are mostly located over the dry subsidence areas in the tropical and subtropical regions.

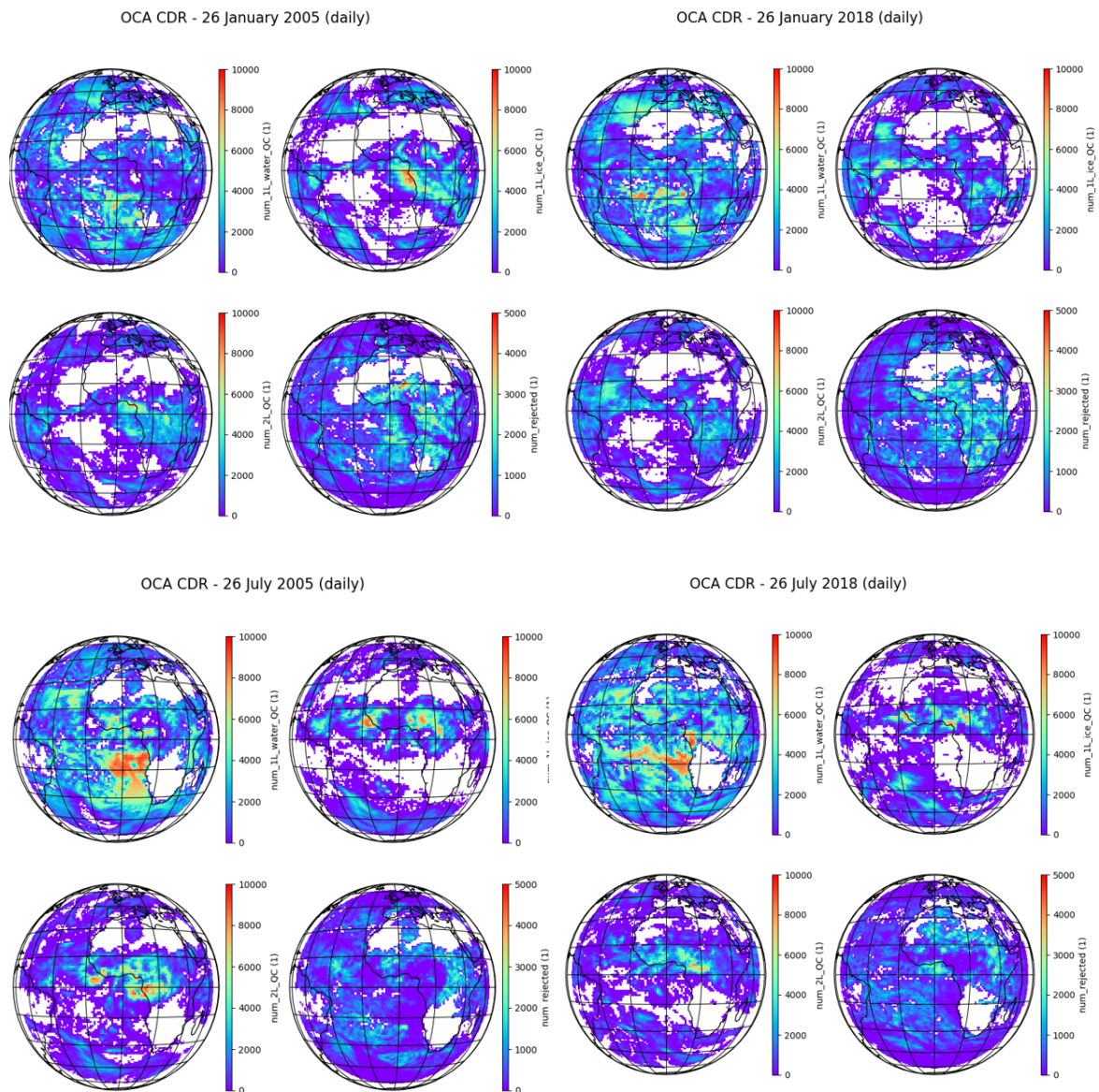


Figure 12: Daily numbers of one-layer water clouds (upper left sub-panel), ice clouds (upper right sub-panel) two-layers clouds (lower left sub-panel) and rejected values (lower right sub-panel). The four main-panels present a boreal winter and summer cases in 2005 (Meteosat-8) and 2018 (Meteosat-10). Only quality-controlled values are shown in the plots.

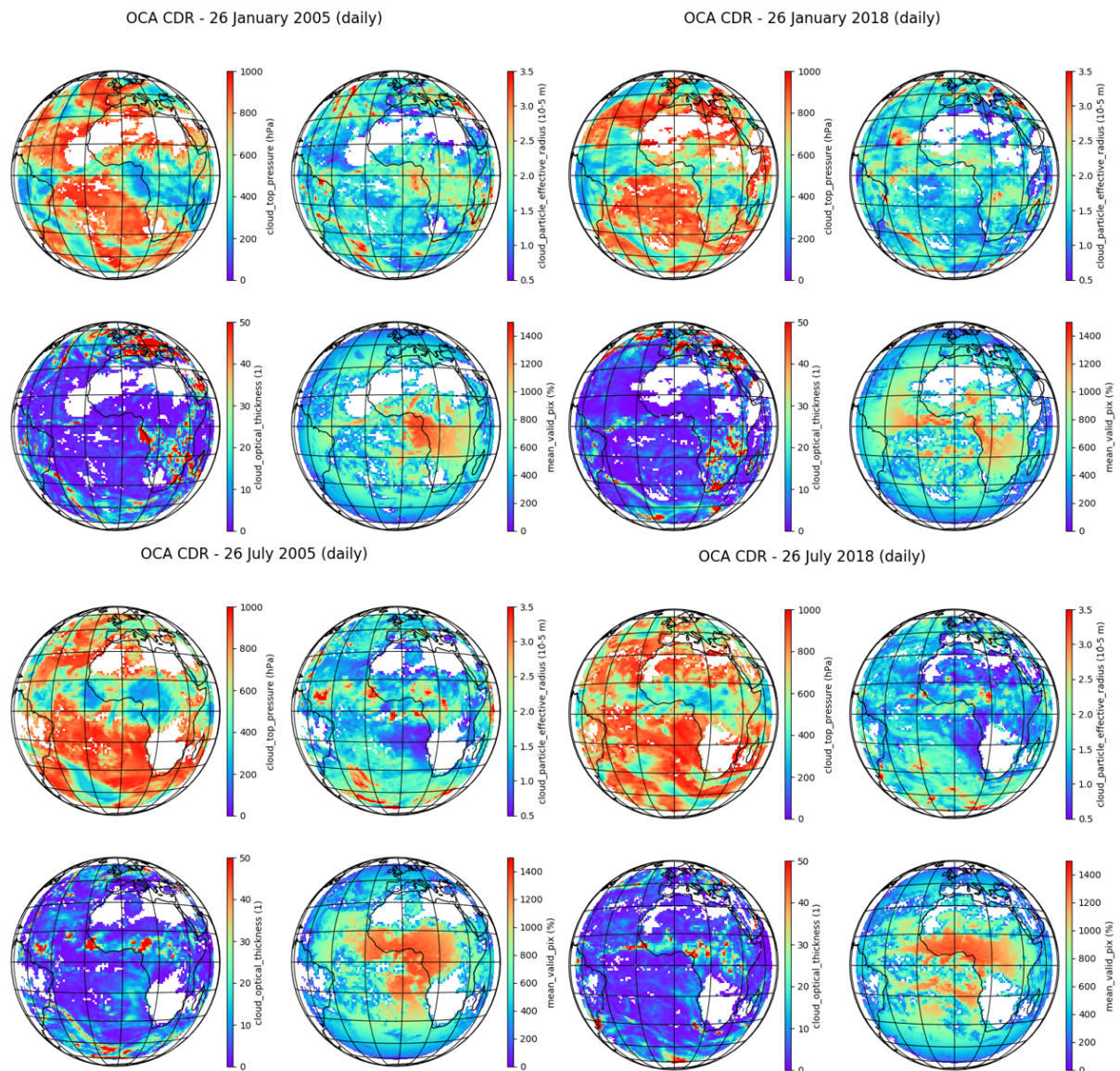


Figure 13: Daily numbers of cloud top pressure (upper left sub-panel), cloud effective radius (upper right sub-panel) cloud optical thickness (lower left sub-panel) and number rejected retrievals (lower right sub-panel). The four main-panels present a boreal winter and summer cases in 2005 (Meteosat-8) and 2018 (Meteosat-10). All values are shown, without any quality control screening.

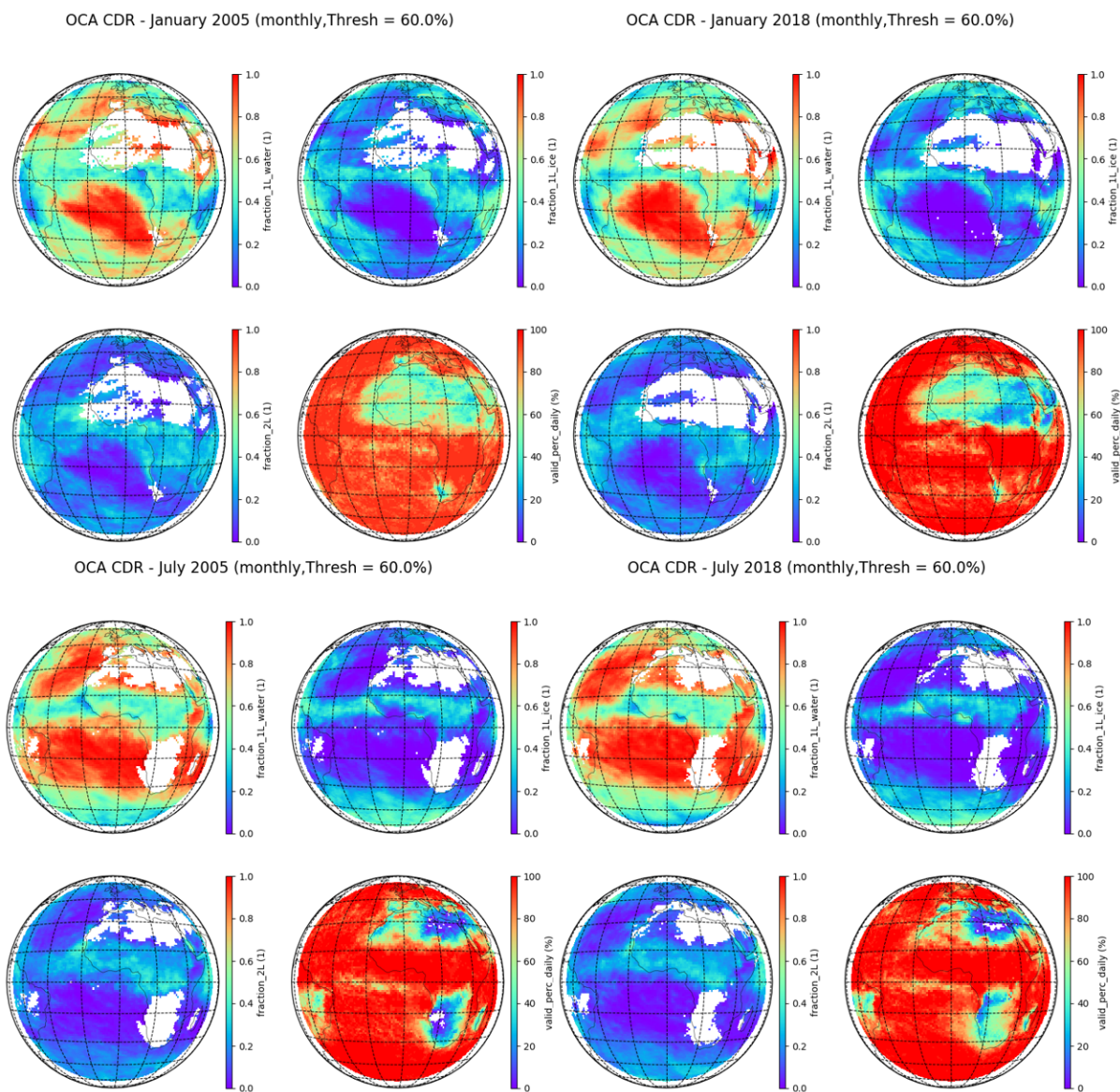


Figure 14: Monthly fraction of one-layer water clouds (upper left sub-panel), ice clouds (upper right sub-panel) two-layers clouds (lower left sub-panel) and valid percentage of daily values per month (lower right sub-panel). The four main-panels present a boreal winter and summer cases in 2005 (Meteosat-8) and 2018 (Meteosat-10). All values are shown, without any quality control screening. A threshold of 60% is applied.

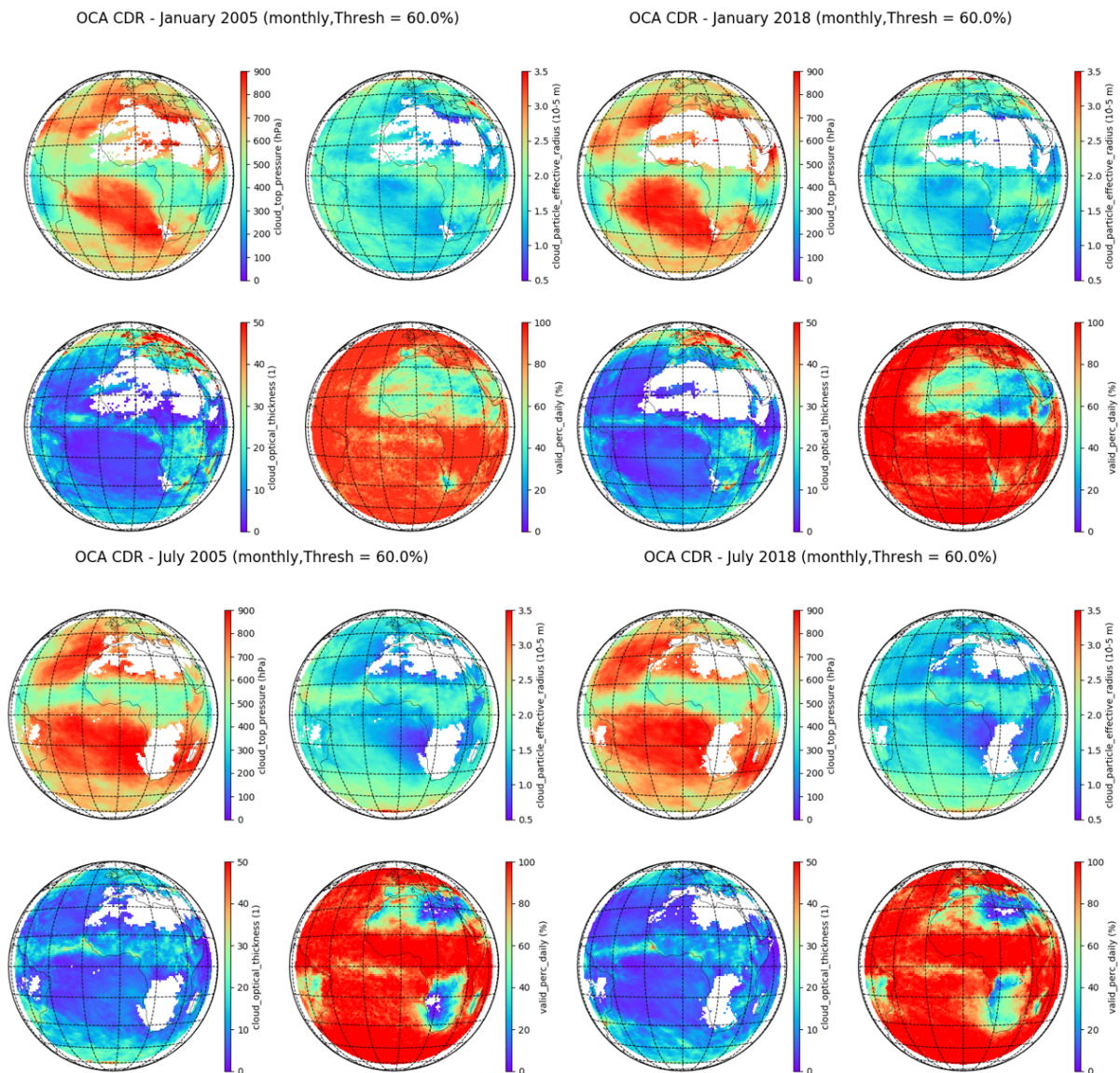


Figure 15: Monthly averages of cloud top pressure (upper left sub-panel), cloud effective radius (upper right sub-panel) cloud optical thickness (lower left sub-panel) and valid percentage of daily values per month (lower right sub-panel). The four main-panels present a boreal winter and summer cases in 2005 (Meteosat-8) and 2018 (Meteosat-10). A threshold of 60% is applied.

6.3 Evaluation Outcome

The analysis of monthly and daily aggregation shows that the OCA Release 1 CDR is complete throughout the 15-year period. The data record is stable, homogeneous and is not affected by the satellite changes. It exhibits the expected geographical and seasonal features of the cloud fields over the domain observed by the Meteosat satellites. The retrieval is more robust during daytime than during nighttime. Over specific areas, such as the Sahara Desert, the quality is lower. This is mostly due to an erroneous cloud mask assignment. Sparse gaps in the data records are due to missing input images.

7 COMPARISON AGAINST REFERENCE DATA

7.1 OCA vs DARDAR

This section presents the comparison of collocated and synchronised A-Train and OCA retrievals over the period 2007-2016, using the collocation technique described in section 5.1. DARDAR retrievals are available during daytime for most of the period, while nighttime combined CALIPSO and CloudSat retrievals are only available until 2011 because CloudSAT stopped working in night mode after this year (see section 3.1). As explained in Section 4.1, data from three days per month were used in order to reduce the amount of processing to a manageable amount. We found that the main evaluation results are not affected by this choice and a larger amount of orbits only slightly reduces the dispersion of the data.

In order to exclude retrievals with low reliability, the final value of the cost function (J_m) and the retrieval errors to filter the OCA retrievals were used to select retrievals with $J_m < 150$ and cloud top errors < 30 hPa. The choice of these thresholds is dictated by the balance of reducing most of the unreliable values, without significantly compromising the sample size. The application of this quality control filter, results in a rejection of about 20% of retrievals. Although each variable could be filtered with its own retrieval error, we used a single filter on the cloud top retrieval error for the validation presented here. A single filter generally indicates highly uncertain retrieval results for all parameters. As DARDAR provides the retrieval of clouds optical and microphysical properties (effective radius and optical thickness) for both water and ice clouds, we also performed the comparison of these properties for the ice cloud retrievals from OCA.

For single layer profiles, the time series of the retrieved cloud top height by OCA against the cloud top height estimated from DARDAR (Figure 16) is consistent through the analysed period and shows that on average OCA cloud tops are 1.7 km lower than DARDAR for ice clouds and 0.1 km lower for liquid clouds.



Figure 16: Time series cloud top height of single-layer clouds from OCA (continuous line) and DARDAR (dashed line) for daytime orbits. Top panel: mean for collocated products within one granule crossing the SEVIRI disk. The coloured shading shows one standard deviation of DARDAR data. Lower panel: mean and standard deviation of the differences between OCA and DARDAR cloud top height. Data are divided between ice (blue lines) and liquid (green lines) clouds.

This result is similar to earlier results (Watts et al., 2011; Hamann et al., 2014, Chung et al., 2017) and highlight the discrepancy in the sensitivity to the effective top layer by the radiometric passive measurements used by OCA and the direct backscatter measured by the lidar. The difference between the two measurements is larger for high ice clouds because they (often) have low density and therefore extinction, permitting radiation to originate from deeper in the cloud. This inherent characteristic of the passive measurements is not accounted for in the OCA fast forward model: a set of lookup tables describe the cloud layers as plane-parallel with an effectively *infinitesimal* geometrical thickness. Therefore, the retrieved cloud top height will be placed at the level of the effective emission of the cloud, because no extra information about the vertical profile of the cloud properties is provided to the forward model. Improvements to the OCA algorithm will include an updated cloud model based on a set of climatological cloud profiles based on CALIPSO and CloudSat measurements (Hoffmann et al., 2019). The use of a more complex, vertically inhomogeneous cloud model significantly impacts the retrieval of cloud top height for high ice clouds and has been found to reduce the difference with respect to the cloud top height estimated from lidar/radar measurements. Note that each cloud has a unique vertical profile of cloud properties. Thus, using climatological cloud profiles will reduce the systematic uncertainty (bias) of OCA retrievals of CTH, but is unlikely to lead to a large reduction of the random uncertainty of these retrievals. The latter might more effectively be reduced if the cloud model was adapted pixel-by-pixel with dedicated cloud property profiles implied by, for example, a cloud type indicator.

Results for the cloud top height retrieval for two-layer clouds shows results comparable to the single layer pixel for the upper layer, but with larger differences (2.0 km lower for OCA) while the second layer shows a bias of 1.9 km, OCA being lower than DARDAR.

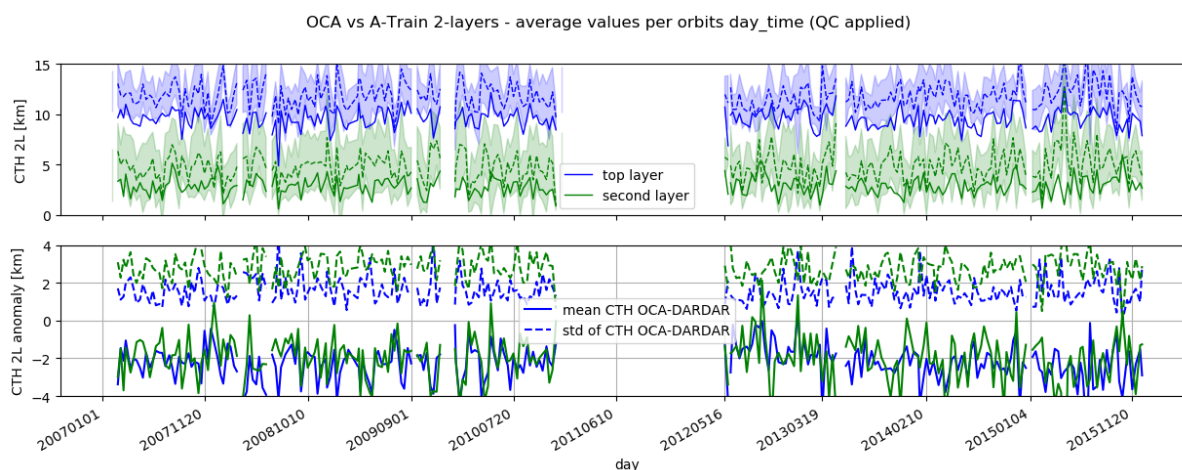


Figure 17: As Figure 16 but for two-layer pixels. Data are divided between upper layer (blue lines) and second layer (green lines).

The number of two-layer pixels within the total dataset of collocated and synchronised A-Train and OCA retrievals is about 25%. For these pixels we only analysed those where both OCA and DARDAR report a multi-layer situation. This explains the large dispersion shown in Figure 17. Although we restricted the analysis to pixels that were classified as multi-layer clouds with higher confidence, using the optical thickness thresholds discussed above, these collocated and synchronised dataset still includes situations where the optical thickness of topmost layer is at the limit of what OCA is capable to observe. In some cases this results in

OCA measuring the height of underlying cloud layers instead of the overlying thin ice cloud layer.

The results for all pixels analysed over the period 2007-2015 are summarised in the aggregated scatter plots of Figure 18. In line with Figure 16, it can be seen that single layer situations OCA compares well with DARDAR for mid and low level clouds, especially for the liquid category, and that the bias increases for high ice clouds. In line with Figure 17, it can be seen that for two-layer cases, the bias for the topmost layer is similar to that of high single layer clouds but with larger dispersion. The comparison for the cloud height of the second layer shows significant dispersion and relatively high frequency of clouds with CTH 5 km that are placed too low by OCA. Some of these points are likely cases where the DARDAR identification of the overlapping layers does not match the same layers sensed by OCA, possibly because of a very thin upper layer.

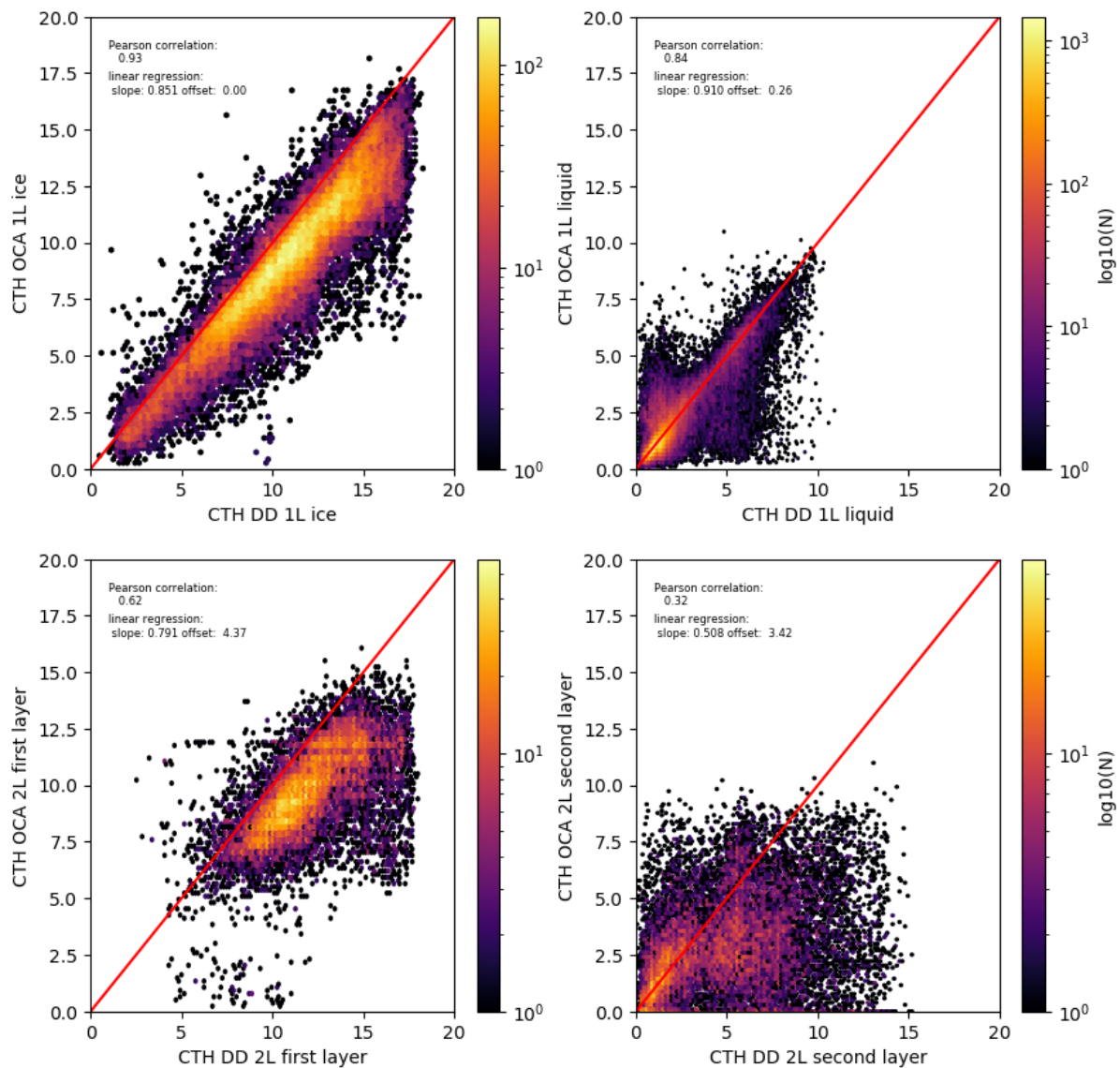


Figure 18: Scatter plots of cloud top height (km) retrieved by OCA and DARDAR for all the collocated pixels in the daytime granules. Upper panels: single layer pixels ice (left) and liquid (right). Lower panels: two-layer pixels top layer (left) and second layer (right).

Nighttime orbits cover a shorter time period, but the general result for the CTH comparison is similar as for the daytime orbits (Figure 19), however with a larger dispersion and slightly larger mean differences (Table 3).

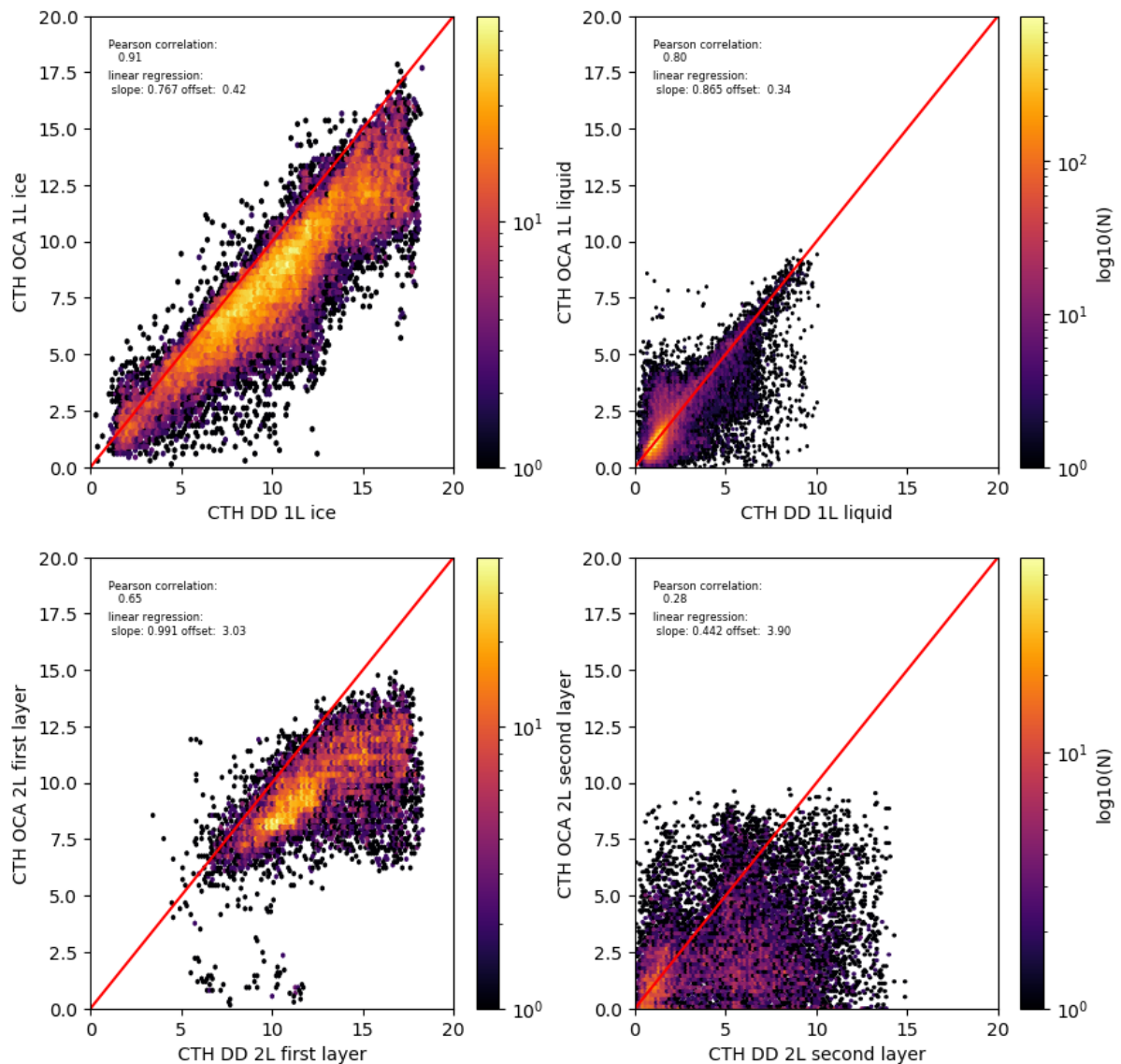


Figure 19: As Figure 18 but for the collocated pixels in the nighttime granules.

The comparison of the retrieved cloud optical thicknesses for ice clouds only, reveals a good agreement for the single-layer cases (Figure 20, upper panels). This is true especially for the daytime retrieval, which benefits from the availability of shortwave channels to constrain the total optical thickness of the layer. For the nighttime the retrieved (Figure 21, upper panels) values are less accurate. The nighttime optical thickness retrievals are exclusively based on SEVIRI's thermal channels which can provide useful information only up to an optical thickness of about 5. The emission of clouds with an optical thickness higher than 5 is saturated, resulting in an effectively unconstrained retrieval using the thermal channels. This low constraint from the measurements makes it more difficult for the retrieval to move from the discrete steps matching the look up table grid, which explains the clustering in discrete steps in the scatter plots.

For two-layers cases, the comparison is complicated by the fact that the overlapping layers are often of type ice over liquid water clouds (about 60% of all multi-layer cases on average). In these cases, the retrieved optical thicknesses from OCA will be higher than those from DARDAR for which no information is available for the liquid cloud layers. Therefore, we restricted the comparison to cases where both layers in DARDAR were detected as ice. This, however, does not always guarantee complete consistency in the cloud types along the full profile as it is possible in certain conditions the presence of residual liquid or mixed phase not correctly identified in the lidar/radar classification.

The comparison of OCA and DARDAR particle sizes (Figure 20 and Figure 21, lower panels) reveals significant dispersion, with OCA spanning a large range of particle sizes from 5 μm and up to 60 μm (the upper boundary of the look up tables used in the forward model). The values retrieved by DARDAR cover a smaller range of particle sizes, with values between 15 μm and 50 μm . This discrepancy is partly related to the effective cloud level measured by the instruments, the real vertical gradient in particle size distribution within the cloud and the ice crystal model and size distributions assumed in both retrievals. Daytime retrievals from OCA are constrained by the solar channels and show, relative to DARDAR a systematic difference of about 2 μm and a random difference (standard deviation) of about 15.9 μm . For the nighttime, the OCA retrievals show no skill and are almost uncorrelated with the particle sizes retrieved by DARDAR.

In two-layer conditions, OCA retrieves the particle size using thermal channels only. For these conditions the upper layer is generally thin enough to allow for retrievals with some skill and smaller retrieval error and data dispersion. For two-layer conditions the mean particle sizes from OCA is about 16 μm during daytime and nighttime. This value is significantly lower than the mean DARDAR particle size of about 30 μm .

OCA vs A-Train - all orbits 2007 to 2015 day_time (QC applied)

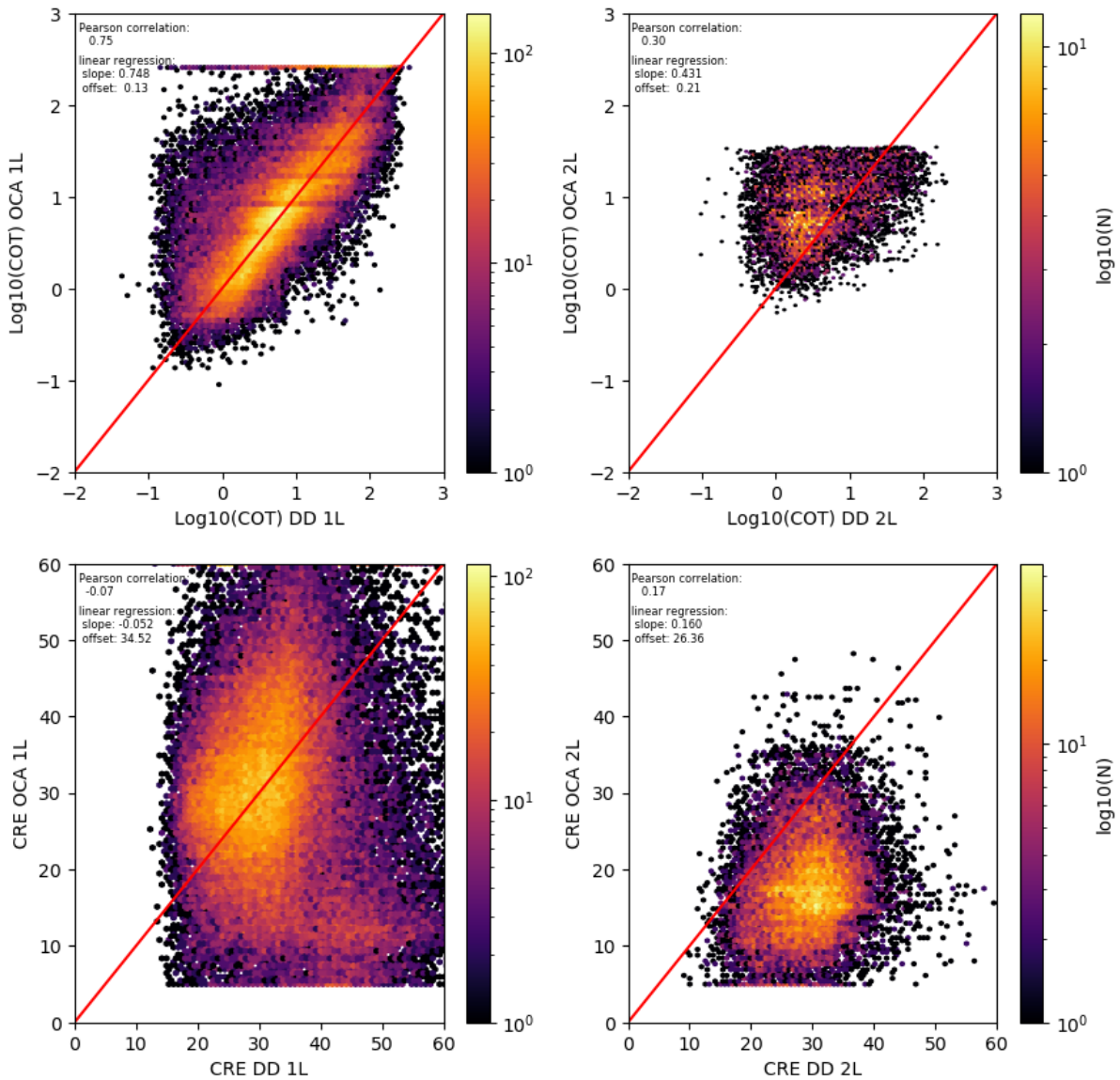


Figure 20: Scatter plots of ice cloud optical thickness and effective radius retrieved by OCA and DARDAR for all the collocated pixels in the daytime granules. Upper panels: cloud optical thickness for pixels identified as single layer (left) and two-layer (right). Lower panels: cloud top effective radius for pixels identified as single layer (left) and two-layer (right). For the two-layer pixels only the total COT from DARDAR where both upper and lower layers are of type ice are used.

OCA vs A-Train - all orbits 2007 to 2010 night_time (QC applied)

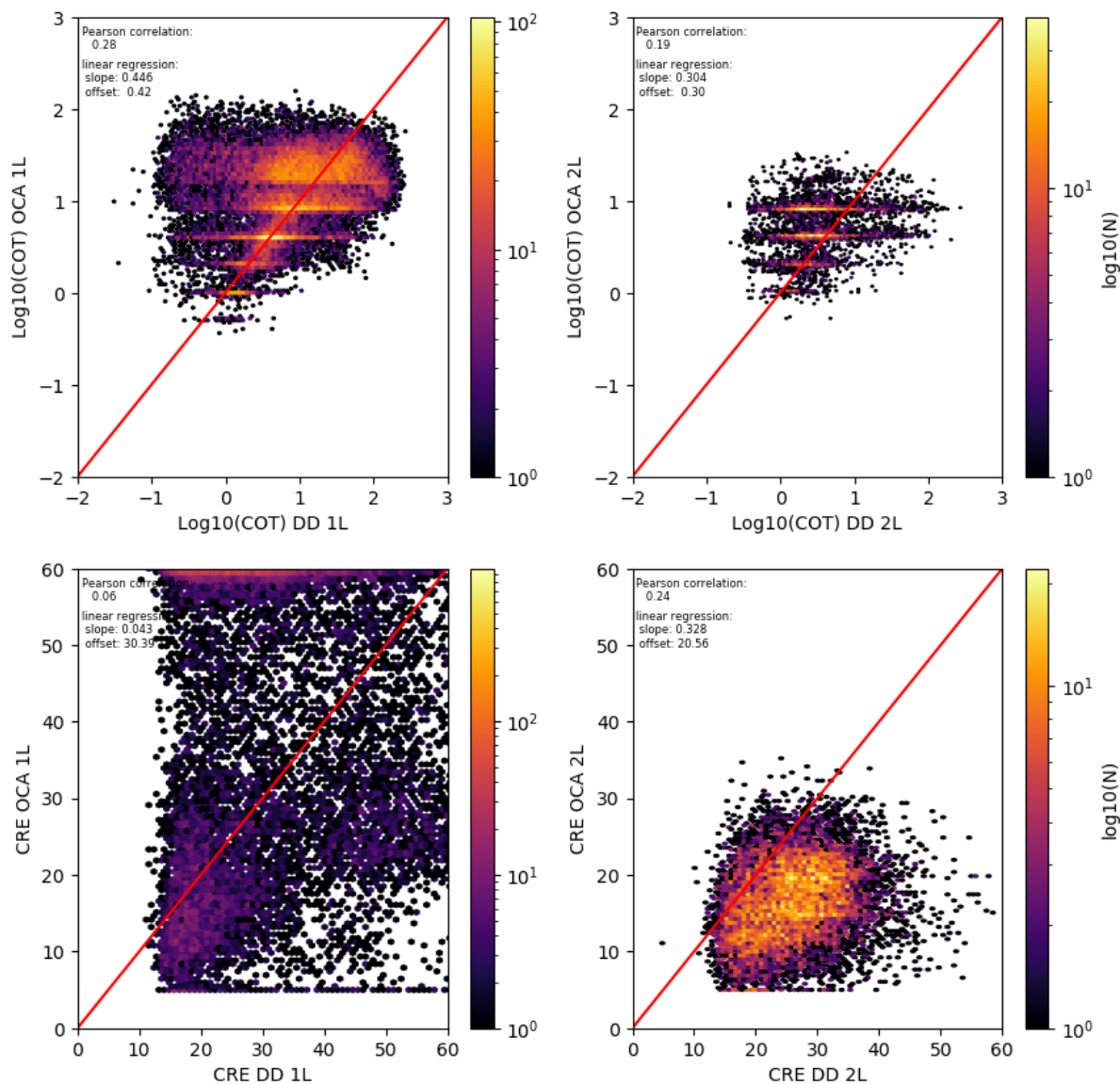


Figure 21: As Figure 20 but for the collocated pixels in the nighttime granules.

Table 3: Summary of the statistics from a set of A-Train granules collocated with SEVIRI pixels. Cloud top height (CTH), ice cloud effective radius at cloud top (CRE) and ice clouds optical thickness (COT) are shown for OCA and DARDAR retrievals. In brackets the standard deviation computed over all the collocated products.

	OCA		DARDAR		OCA-DARDAR	
	Day (2007-2016)	Night (2007-2010)	Day (2007-2016)	Night (2007-2010)	Day (2007-2016)	Night (2007-2010)
CTH (km)	mean (std)	mean (std)	mean (std)	mean (std)	mean (std)	mean (std)
Ice, single	9.2 (3.0)	8.2 (3.2)	10.8 (3.3)	10.2 (3.7)	-1.6 (1.2)	-2.0 (1.6)
Liquid, single	1.9 (1.5)	1.7 (1.3)	2.0 (1.6)	1.8 (1.4)	-0.1 (0.9)	-0.1 (0.8)

Two-layer upper	9.7 (1.8)	9.8 (1.7)	12.1 (2.4)	12.7 (2.6)	-2.4 (1.9)	-2.9 (2.0)
Two-layer lower	2.9 (2.0)	2.6 (2.1)	4.9 (3.2)	5.0 (3.3)	-2.0 (3.1)	-2.3 (3.3)
CRE (μm)						
Ice, single	30.8 (12.9)	50.9 (16.3)	32.9 (8.9)	32.7 (11.2)	-2.1 (15.9)	18.4 (19.2)
Two-layer upper	17.4 (6.1)	16.5 (4.9)	29.3 (5.8)	26.0 (6.6)	-11.9 (7.9)	-9.4 (7.2)
Log10(COT)						
Ice, single	0.87 (0.64)	1.01 (0.40)	0.78 (0.63)	0.91 (0.64)	0.08 (0.44)	0.18 (0.65)
Two-layer	0.87 (0.65)	0.70 (0.27)	0.42 (0.50)	0.35 (0.42)	0.44 (0.52)	0.35 (0.45)

The cloud feature mask includes information about the phase of cloud layers, and thus the dataset collocated and synchronised OCA and DARDAR retrievals can also be used for validating the cloud phase retrievals from OCA. The result of this validation, as summarised in the matrix in Figure 22, shows the agreement between OCA and DARDAR for the categories of ice, liquid and multi-layer clouds as observed during the daytime orbits. Note that offline analysis revealed that the results of the nighttime orbits are similar to those from the daytime orbits.

We can see that of all OCA retrievals in the single layer ice cloud category (blue column), 63% fully agrees with DARDAR, 22% partly agrees with DADAR with also an ice phase but then falling in the two-layer category, and 15% disagrees with DARDAR and retrieves single layer liquid clouds. For the single layer liquid category (green column) there is a very high agreement of about 93%.

In OCA the two-layer category always assigns the phase ice to the upper layer and the phase undetermined to the lower layer. We used DARDAR to analyse the phase of the upper and lower layer. The results show, in the majority of cases the upper layer is of phase ice (95%) and the lower layer has a prevalence is for phase liquid water (55%). In terms of detection of multi-layer situations, the comparison shows that OCA and DARDAR agree in about a third of the cases. The remaining two thirds of multi-layer cases are assigned either as single layer ice or as single layer liquid water clouds by OCA.

It has to be noted, on one hand these results depend on the definition of the reference truth for multi-layered cloud profiles, which is not always clear-cut, in particular not for thin upper cloud layers (see discussed in section 5.1). This might be the case for some of the multi-layer clouds that were retrieved as single layer by OCA. In this case the CTH retrieved by OCA tends often to be closer to the second layer in the DARDAR profile, as shown in the right panel of Figure 23, or between of the two layers when both cloud layers have a significant impact on the upwelling radiance measured by SEVIRI. This disagreement in the categorisation between OCA and DARDAR was observed in about 14% of all OCA ice cloud types. On the other hand, when OCA retrieves a single layer ice cloud as multi-layer, errors in the retrieved CTH are smaller and results are similar to what already analysed in Figure 23, left panel. This latter case happens in about 17% of all OCA ice cases, often when the upper cloud layer has a low particle density or with a challenging vertical distribution of ice water content.

In general, including in the CTH evaluation the pixels where the OCA multi-layer categorisation does not match the DARDAR one, scores suffer of a slight degradation. This is relevant to correctly interpret the comparisons presented in section 7.2.1 where the disk-averaged values in OCA include all cloud types. As we can see from Figure 24, for the ice category, the one mostly affected by errors in the categorisation of the multi-layer profiles, the average difference between the two dataset increases by about 300 m when all points are included. This is likely an upper-end estimate because part of the points showing a large OCA-

DARDAR difference are due to thin upper layers not observed by SEVIRI but still identified as top-layer in DARDAR according to the threshold adopted in this study (section 5.1) rather than to missed two-layer profiles by OCA.

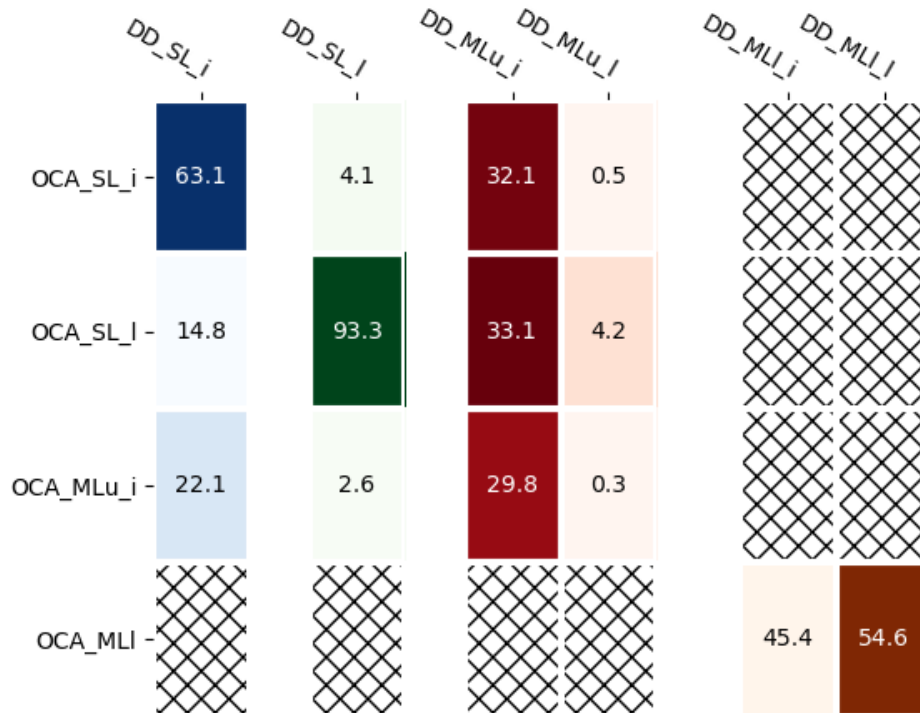


Figure 22: Comparison of cloud categorisation in OCA and DARDAR (DD). The categories are single layer ice (SL_i), single layer liquid (SL_l) and multi layer (ML). The multi layer category is further divided into upper layer (MLu) and lower layer (MLl) and both can be of the type ice (MLu_i, MLl_i) or liquid (MLu_l, MLl_l). The numbers and colors refer to the percentage of cases with respect to the total of that category (blue=ice, green=liquid, red=multi-layer). For OCA, the multi-layer category only allows ice for the upper layer while for the lower layer the phase is not defined. The comparison is done for the daytime A-Train orbits collocated with SEVIRI with the quality-control filter applied as explained in the text.

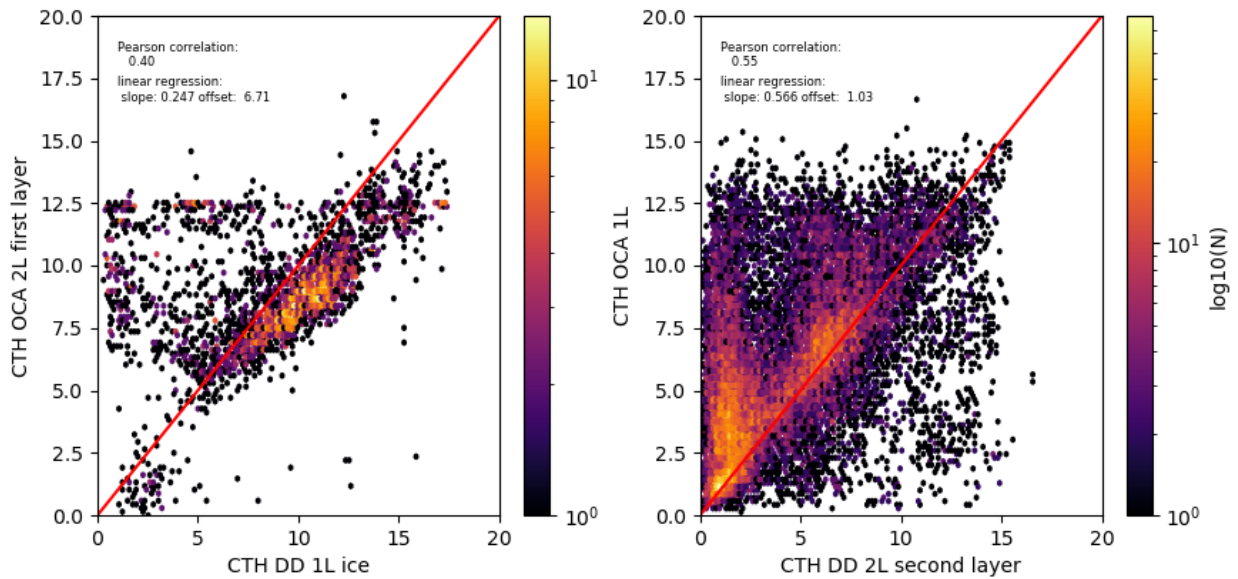


Figure 23: Scatter plots of cloud top height (km) retrieved by OCA and DARDAR for all the collocated pixels in the daytime granules for the profiles where the single/two layer characterisation does not agree between OCA and DARDAR. Left: profiles where OCA retrieves two layer clouds and DARDAR single layer. The first layer in the OCA retrieval is shown. Right: profiles where OCA retrieves single layer clouds and DARDAR shows multiple layers. The OCA CTH is compared to the second layer in the DARDAR profile.

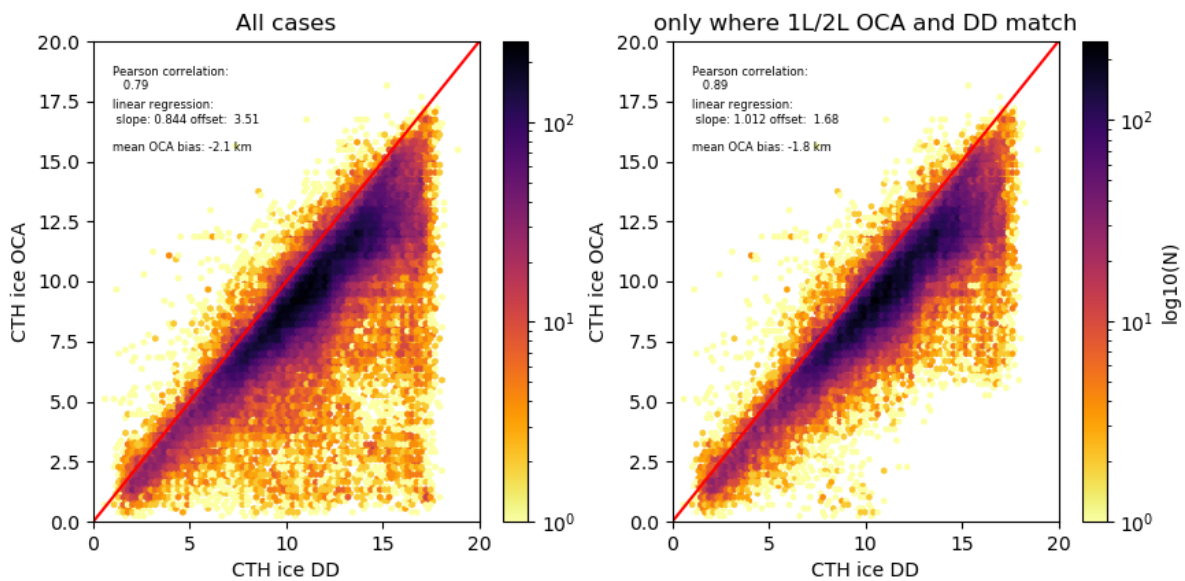


Figure 24: CTH comparison between OCA and DARDAR for the ice cloud type. The comparison includes all cases of single and multi-layer profiles. The left hand side plot includes the profiles where the multi-layer categorisation does not agree between OCA and DARDAR. In the right hand side plot only includes points where the multi-layer categorisation agrees between the two datasets. Data are for the set of day-time orbits between 2007 and 2015.

7.1.1 Evaluation of the OCA product uncertainty

The optimal estimation algorithm at the core of the OCA retrieval allows for the computation of an uncertainty estimate for each state variable and, as mentioned before, these error estimates

are used to provide a basic quality control for the products to remove the retrievals with a large uncertainty.

It is valuable for a CDR an estimate of the quality of the retrieval uncertainty, but the task is generally not straightforward. A series of different contributions affect such an analysis from the uncertainty in the reference dataset to the errors related to the collocation procedure, the geophysical variability of the variable being analysed and the differences in the physical quantity measured in the two comparing datasets (Merchant et al., 2017) . In this section we provide an evaluation of the quality of the uncertainty estimate for the CTH retrieved by OCA. For this product the uncertainty in the reference retrieval from CloudSat and CALIPSO is generally negligible and the source of the remaining uncertainty is due to the comparison procedure.

The quality of OCA CTH uncertainty is evaluated using as metric the difference between the OCA and DARDAR CTH ($x_{oca}-x_{dd}$), scaled by an estimate of the total uncertainty. Assuming negligible the uncertainty in the CTH retrieved by CloudSat/CALIPSO, the total uncertainty depends on two contributions, the OCA retrieval uncertainty (u_{oca}) and the uncertainty arising from the comparison procedure (u_{comp}) including the spatio-temporal mismatch in the collocation, difference in the measurements from active and passive instruments and assumptions used in the definition of cloud phase and multi-layer situations. The metric is

therefore defined as the ratio $\frac{x_{oca} - x_{dd}}{\sqrt{u_{oca}^2 + u_{comp}^2}}$ and it shows how the total uncertainty compares to the difference between the OCA CTH and the reference values from DARDAR. Large values of the ratio indicate likely underestimated uncertainty not able to properly represent the difference against the reference values. To take into account some of the uncertainties implicit in the comparison procedure used in the analysis and in the collocation method, we considered $u_{dd}=1\%$ of the DARDAR CTH. The value is a very conservative estimate of contributions difficult to quantify. Moreover, to account for the known difference in the cloud level sensed by the lidar/radars and SEVIRI, we removed the average bias of 1.6 km for ice clouds CTH (2.0 km for night time pixels), as reported in Table 3.

For an ideal uncertainty estimate, the distribution of these scaled differences would have a Gaussian shape with unity standard deviation and full width at half maximum (FWHM) of 2.35. Larger FWHM indicates underestimated uncertainties and as we can see from **Error! Reference source not found.** this is the case for the OCA CTH uncertainty. Both the night-time and day-time one layer CTH are a factor between 8 and 15 too small. Part of this is due to the underestimation of the uncertainty contribution coming from the characterisation of scene and cloud properties in the OCA forward model. If this choice on one hand preserves a high precision in the CTH retrieval, on the other hand it results in an underestimated final retrieval uncertainty.

An inflation by a factor about 10 of the CTH uncertainty provided in this CDR is therefore suggested as the accuracy of the product. The precision is certainly higher and this should be taken into account depending on the particular application.

The uncertainty computed for the other variables should likely be inflated to a similar degree, but a full evaluation is not attempted for this first version of the data record.

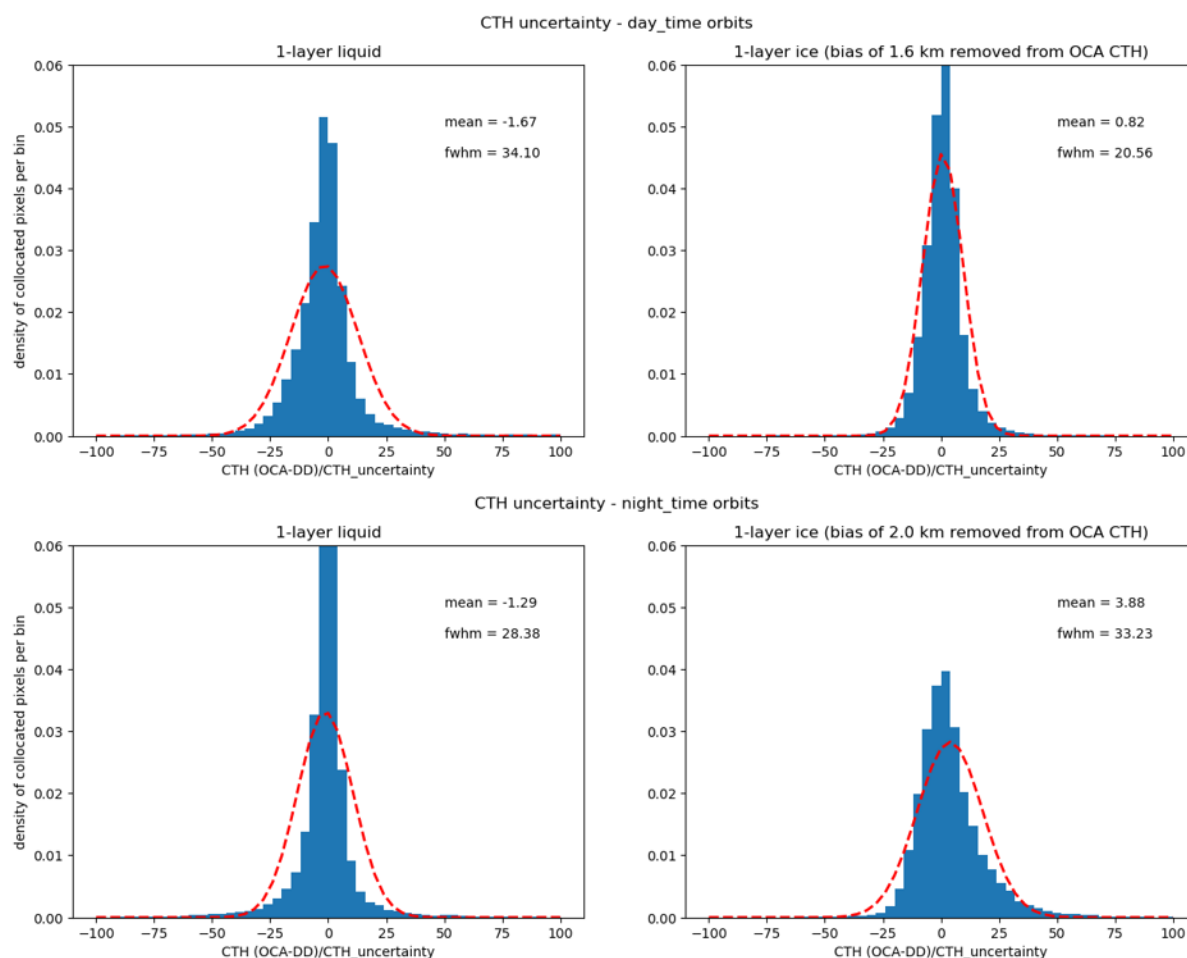


Figure 25: OCA CTH uncertainty validation expressed as the difference between OCA and DARDAR CTH scaled by the combination of retrieval uncertainty and uncertainty due to the comparison procedure (see text). Top panels are for day-time orbits 2007-2016 and lower panel for night-time orbits (2007-2010). Left are results for one-layer liquid clouds and right for one-layer ice clouds. Large values indicate that the uncertainty is likely too small to correctly account for the observed difference between the OCA and DARDAR CTH. OCA vs MODIS and CLAAS 2.1

7.2 OCA vs MODIS and CLAAS 2.1

This section presents the comparison between OCA Release 1 CDR against the cloud products from MODIS and CLAAS 2.1 CDRs, i.e., cloud top pressure (CTP), cloud particles effective radius (CRE) and cloud optical thickness (COT). All MODIS products used in the following comparisons are the average between the AQUA and the TERRA retrievals. This is a cross-comparison between retrievals based on passive imager measurements and therefore shall be considered as an evaluation of the consistency of OCA Release 1 and not as its validation. For the CTP a third dataset is used, based on the L3 CALIPSO GEWEX cloud top products, using the cloud top version that approximates the cloud top pressure sensed by a passive instrument.

With the pre-processing applied to the data described in sections 5.2 and 6, we reduced, as much as possible, the differences in the three datasets caused by the differences in time averaging, spatial gridding and type/phase aggregating. We found that this leads to a fair comparison between OCA and the other two reference datasets. The main discrepancies

between the CDRs, as highlighted in the following sections, are dominated by the intrinsic differences in algorithms, cloud masks and, for MODIS products, the platform.

7.2.1 Cloud Top Pressure (CTP)

The OCA mean spatial distribution of CTPs captures the large-scale seasonal feature in the cloud height and is comparable with the other datasets (Figure 26), but with distinct differences. On average the OCA CTP retrievals fall within those retrieved by MODIS and CLAAS 2.1. Generally, OCA retrieves lower CTPs than MODIS over land and water and higher CTPs than CLAAS 2.1, with larger differences over land. In agreement with the analysis against CloudSat and CALIPSO data in Section 7.1, the differences are smallest in areas dominated by thick low water clouds, such as the stratocumulus region over the SE Atlantic. The observed differences are largest over the intertropical convergence zone, where a large fraction of ice and multi-layer clouds exists. A distinct feature in the OCA dataset is the large occurrence of low CTPs over the Sahara Desert. This problem is caused by contamination of surface signal over very bright and hot surfaces that is emitted through high thin ice clouds. This problem occurs in the CLAAS 2.1 data as well.

Figure 27 shows an example for very thin ice clouds over the western Sahara. We can observe that both OCA and CLAAS 2.1 retrieve a large number high CTPs at the edges of these thin ice clouds. The feature is further enhanced in the OCA data due to the very cloudy sky-conservative cloud mask used in input. This means that the algorithm has to deal with a lot of pixels with very thin cloud layers. Because these retrievals in OCA are not much affected by a large cost or large final errors they are accepted by the quality control. This leads to an overestimation of CTP in over desert. Besides a revision of the cloud mask used by OCA, the further improvements in the CTP retrievals should reduce the occurrence of extremely high CTP retrievals in these conditions, which is subject to further research. As OCA Release 1 includes the cloud probability fractions, the user can filter out areas with very thin clouds.

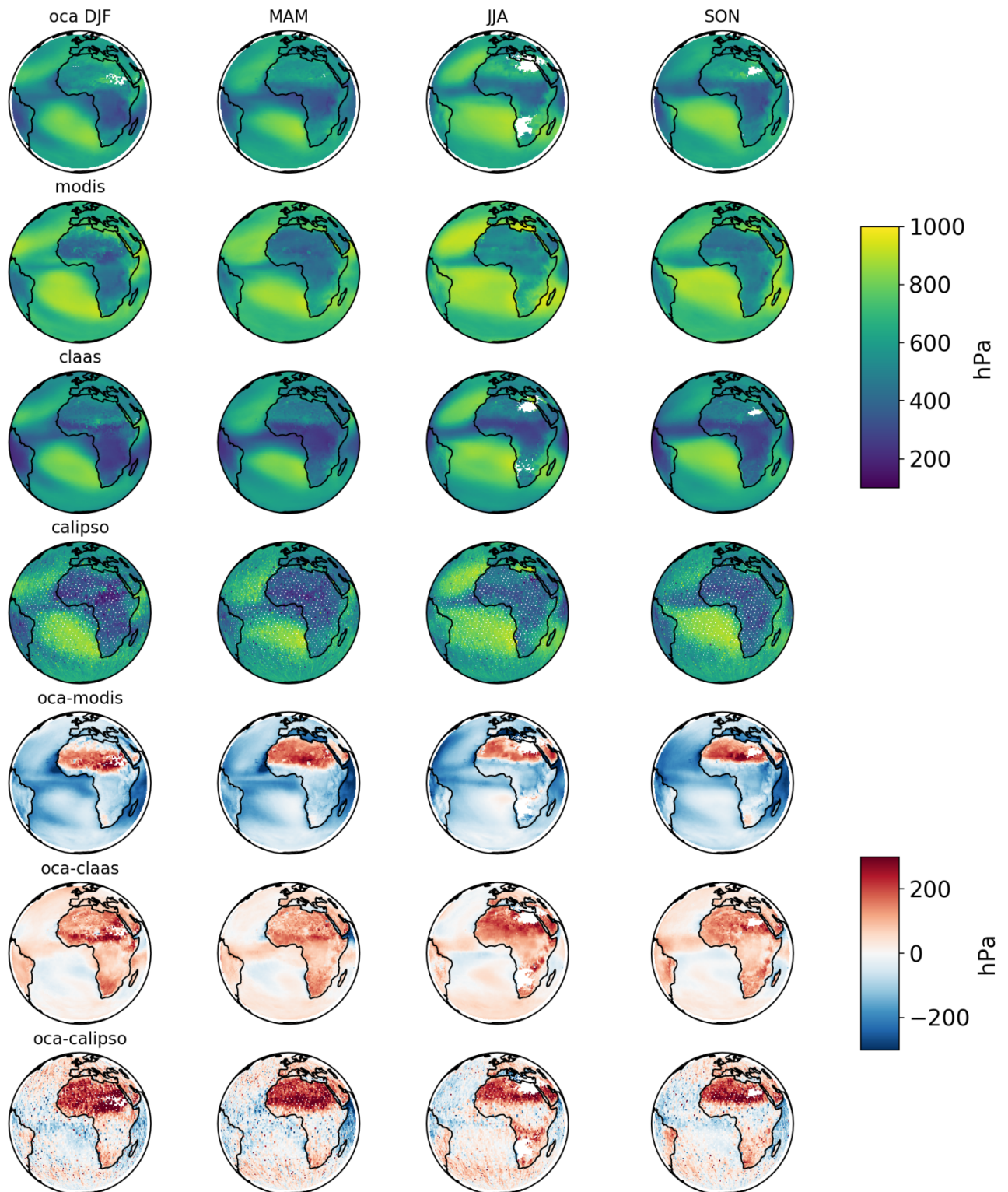


Figure 26: Seasonal mean combined (ice+liquid water clouds) CTP from OCA, MODIS, CLAAS 2.1 and CALIOP GEWEX L3 datasets. On the bottom the difference between OCA and respectively MODIS, CLAAS 2.1 and CALIPSO GEWEX L3 (passive CTP flavour). White areas in the OCA and CLAAS 2.1 figures indicate regions where not enough valid retrieval were available (see text for details).

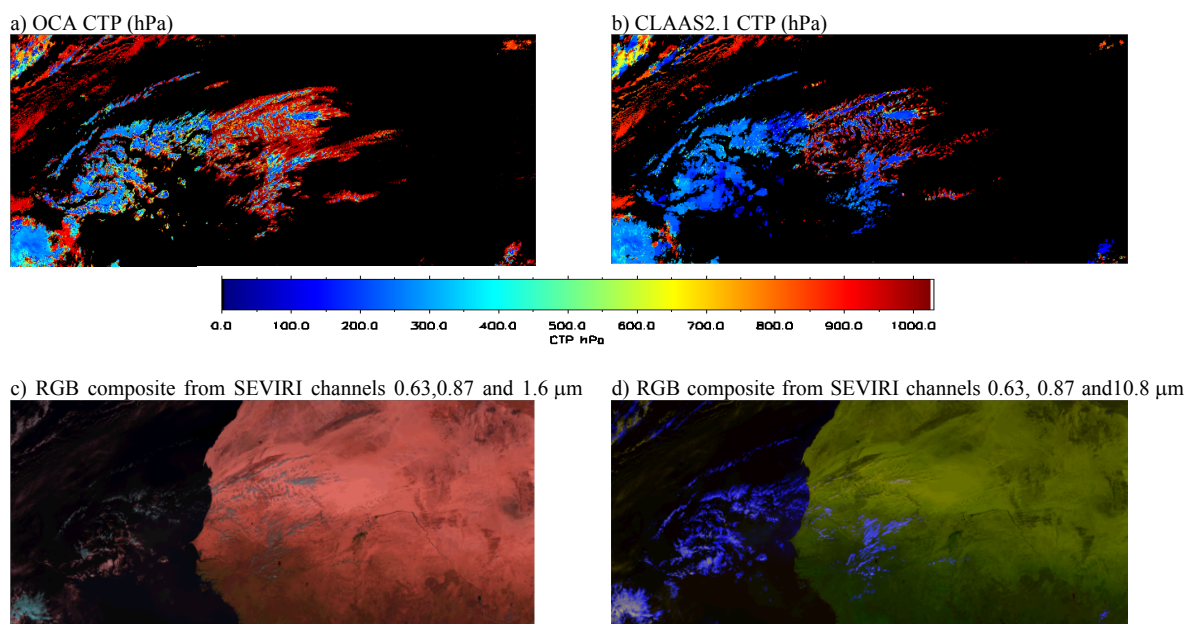


Figure 27: OCA (a) and CLAAS 2.1 (b) CTP (hPa) retrieval over western Sahara for the repeat cycle at 12UTC on the 20th of January 2010. In blue are clouds with low CTPs and in red clouds with high CTPs. RGB composite from SEVIRI channels 0.63 μm, 0.87 μm, 1.6 μm (c) and 0.63 μm, 0.87 μm, 10.8 μm (d).

These characteristics are confirmed by the comparison against the CALIPSO L3 GEWEX CTP when adjusted to better represent what a passive instrument would sense by selecting only clouds with $COT > 0.3$. The area over the Sahara Desert again shows a consistently high occurrence of too low cloud tops (large CTP) in OCA while a mix of positive and negative differences are observed over the oceans: at high latitudes OCA tends to retrieve lower cloud tops than CALIPSO while slightly higher cloud tops (lower CTP) are observed at lower latitudes.

When the un-adjusted CALIPSO CTP are used (Figure 28), the picture becomes more similar to what already observed in the analysis against DARDAR, with a widespread underestimation of the cloud top height due to the prevalence of high, often thin cloud sensed by the lidar and not seen by SEVIRI.

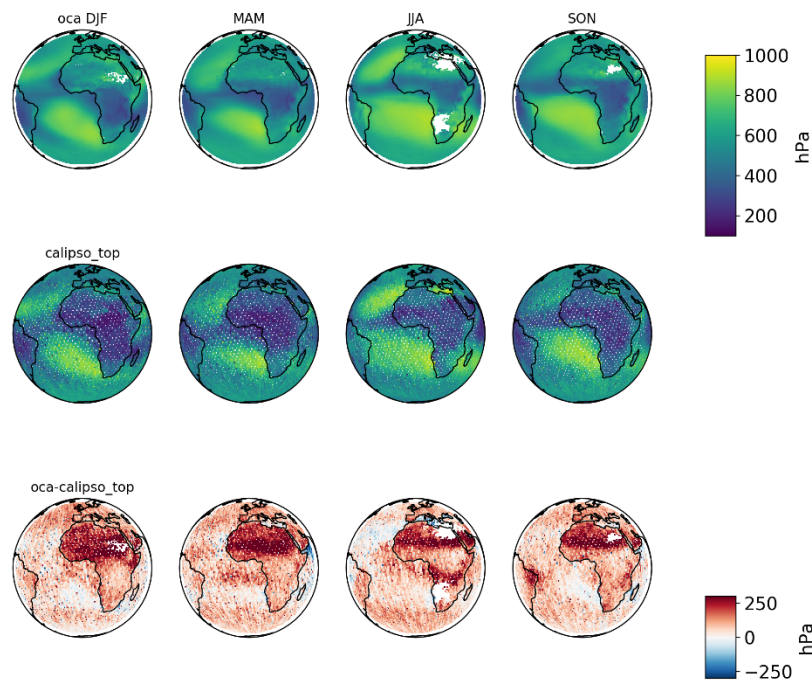


Figure 28: As Figure 26 but only showing the CTP comparison between OCA and CALIPSO L3 GEWEX for the TopLayer version

The time series of the area-weighted disk average CTPs over the whole period 2004-2019 (see Figure 29) confirms the mean differences between the datasets discussed above. OCA sits in between the MODIS and CLAAS 2.1 retrievals. The CALIPSO L3 GEWEX time series covers a shorter time frame than the other three and shows on average lower CTP than OCA, part of the difference being dominated by the positive bias shown by OCA over the North Africa. The four time-series are consistent and highly correlated, showing the same features throughout the years. One characteristics shared between the two SEVIRI-based datasets is an upwards trend starting from about 2012, though this is not statistically significant in the OCA database. The feature was also noted in the CLAAS 2.1 validation report (Finkensieper, Stephan et al., 2020).

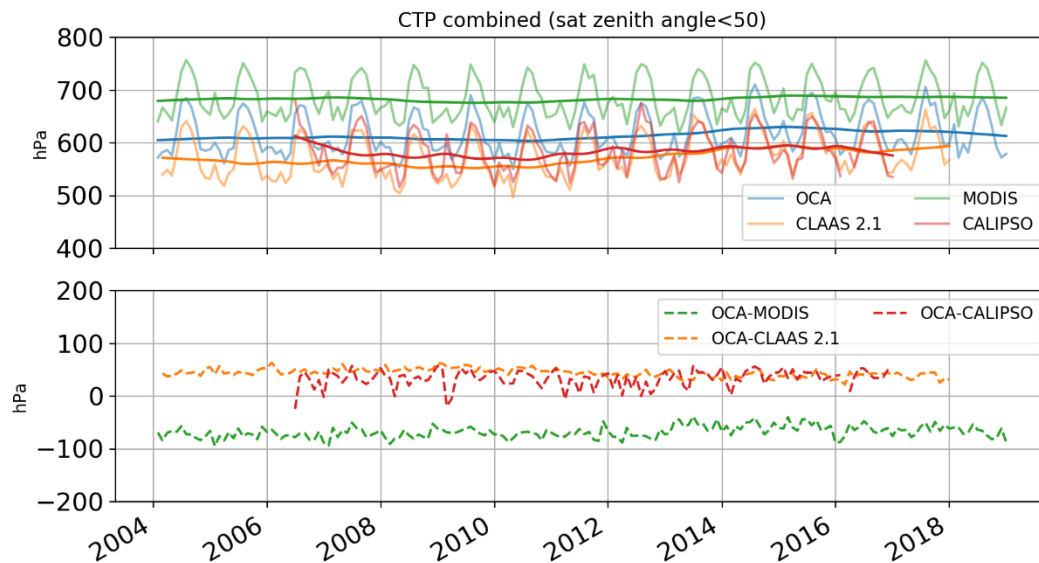


Figure 29: Weighted area-average of retrieved cloud top pressure (CTP) from OCA, MODIS, CLAAS 2.1 and CALIPSO L3 GEWEX (passive CTP flavour) datasets over a SEVIRI disk. Averages are done for the areas within a maximum SEVIRI viewing angle of 50° . Top panel: monthly means with a lowess (locally weighted scatter plot smooth) smoothing filter applied to each time series. Lower panel: differences between OCA and respectively MODIS, CLAAS 2.1 and CALIPSO L3.

7.2.2 Cloud Optical Thickness (COT)

The spatial distribution of OCA total cloud optical thicknesses, combining ice, liquid and multi-layer cloud types, is in general agreement with the other two datasets, although there are some distinct differences (Figure 30). OCA observes larger COTs than MODIS over land in Central Africa, while it observes generally lower values than CLAAS 2.1 over land and sea, particularly over the Southern Ocean. Large positive COT anomalies in the western hemisphere correspond to areas where there is a combination of both large solar zenith angles to the East and large viewing zenith angles to the West. This means that most of the signal in the solar channels comes from back-scattered radiation, often from the side of the clouds which, due to their larger optical paths, artificially increase the retrieved COT. A similar effect is seen in the CLAAS 2.1 record, but here the effect is smaller because the CLAAS 2.1 L2 products used in the generation of the L3 dataset are limited to a solar zenith angle $< 75^\circ$. Although we created the monthly averages trying to minimise their impact, OCA retrievals in the twilight are partly included in the monthly means generation (section 6.1.1). The inclusion of these retrievals cause the distinct sharp lines observed in Figure 30 especially in the differences against CLAAS 2.1 and MODIS. These lines correspond to the transition of the OCA retrieval from day-time to night-time following the movement of the terminator towards the west as the day progresses. Similarly, the large COT retrieved at high latitudes towards the South Pole is common to both SEVIRI retrievals and most likely a result of the high viewing zenith angle of SEVIRI in those regions.

Areas of large positive anomalies over the Eastern Sahara and Arabian Peninsula are caused by pixels defined as cloudy but are in reality surface features misinterpreted by the cloud mask, as discussed for the CTP in section 7.2.1. In this situation OCA COT retrieval is not reliable. These pixels can be filtered applying a higher cloud probability threshold to the L2 product.

Future improvements to the algorithm will include the capability to better constrain the retrieval in these situations.

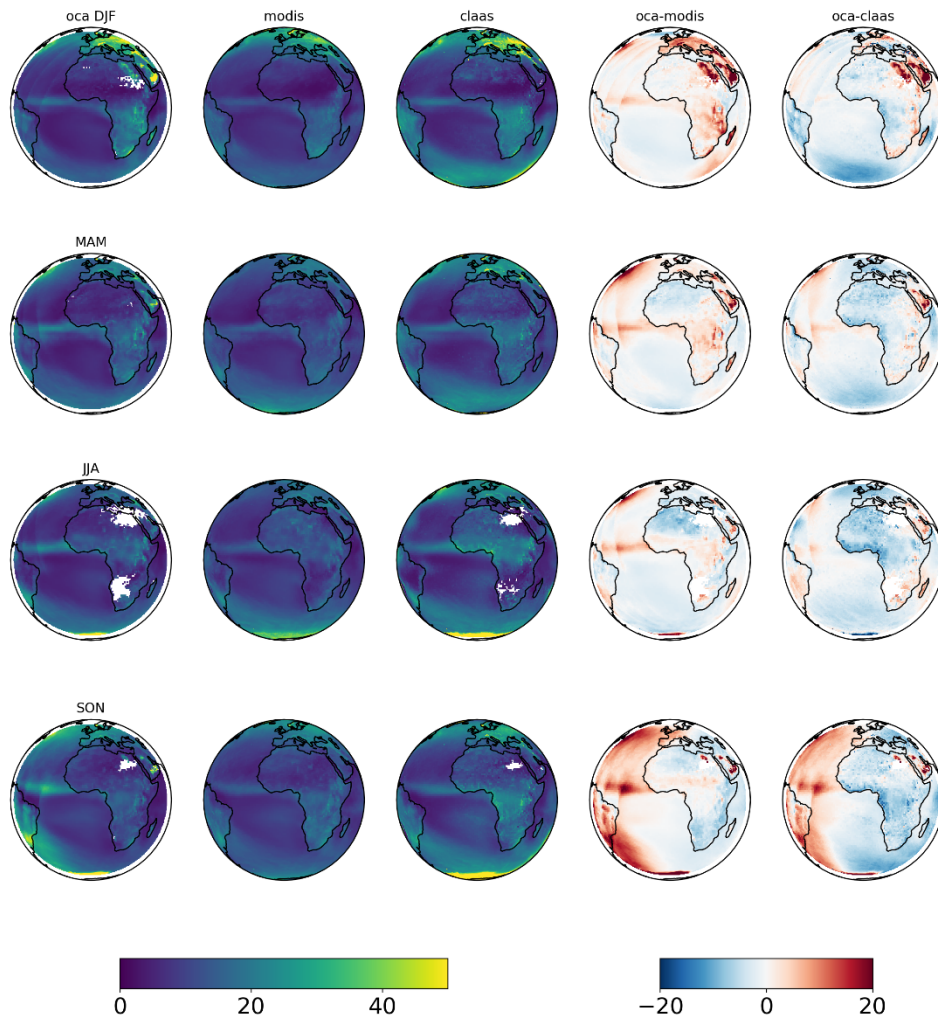


Figure 30: Seasonal mean combined (ice+liquid water clouds) cloud optical thickness (COT) from OCA, MODIS and CLAAS 2.1 datasets. On the right the difference between OCA and respectively MODIS and CLAAS 2.1. White areas in the OCA and CLAAS 2.1 figures indicate regions where not enough valid retrieval were available (see text for details).

The time series of the retrieved COT over the full period shows that the OCA COTs fall between the other two datasets with a distinct annual cycle with a maximum around December (Figure 31). This is in part linked to the above mentioned cases of high COT over the desert and in part to the large COTs retrieved at the edge of the twilight region. The annual cycle in the COT is visible also in the time-series of the other two datasets, but with a smaller magnitude than in the OCA.

From about end 2012, the OCA time-series shows a decrease in the mean COT that brings the values closer to MODIS. It is possible that this change is related to issues in the shortwave channel calibration of SEVIRI. The OCA Release 1 CDR uses the operationally calibrated Level 1 data that were adjusted with a set of (static) offsets to account for the significant deviations found in comparisons between SEVIRI and MODIS Level 1 data (Meirink et al., 2013). This static correction is likely to have left some uncorrected drifts and jumps in the accuracy of the calibration, especially at the interchanges between instruments.

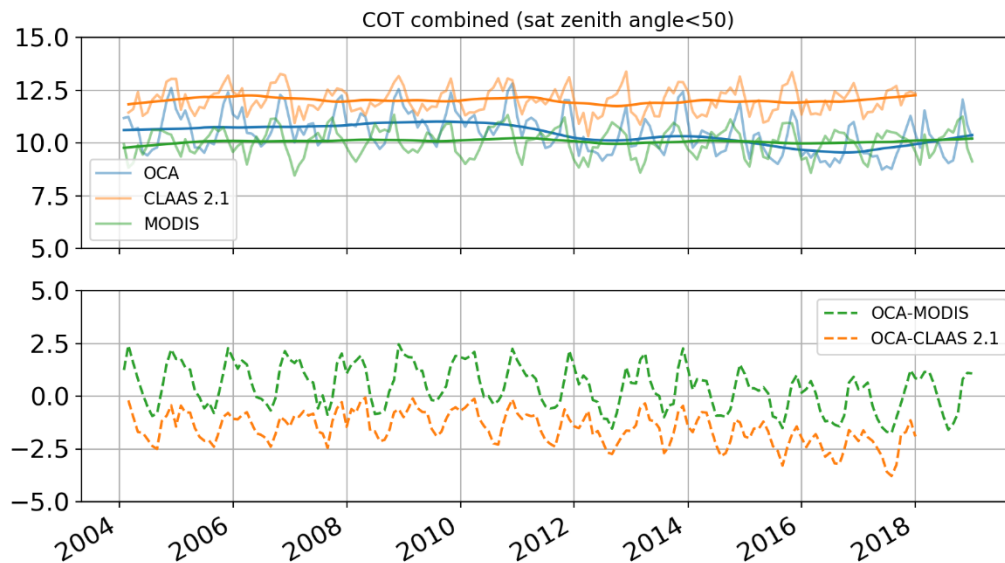


Figure 31: Weighted area-average of retrieved cloud optical thickness (COT) from OCA, MODIS and CLAAS 2.1 datasets over a SEVIRI disk. Averages are done for the areas within a maximum SEVIRI viewing angle of 50°. Top panel: monthly means with a lowess (locally weighted scatter plot smooth) smoothing filter applied to each time series. Lower panel: differences between OCA and respectively MODIS and CLAAS 2.1

7.2.3 Cloud Particle Effective Radius (CRE)

The analysis of the cloud particles effective radii is done for ice and liquid phase separately, as explained in Section **Error! Reference source not found.** The seasonally-averaged ice cloud particle sizes for the three datasets are shown in Figure 32. MODIS and OCA use the same underlying ice crystal model, represented by aggregates of severely roughened solid columns (based on Yang et al. 2013 and Baum et al., 2011, 2014) while CLAAS 2.1 retrievals are based on the assumption of randomly oriented roughened hexagons. The bulk ice scattering properties look-up tables are computed by averaging the single particles properties over a set of gamma-type size distributions for different particle effective dimensions.

The combination of different algorithms, assumptions on the ice habits and particle size distributions, and the definition of the effective dimension are the main contributors for the differences in the ice particle dimension retrieval observed in our comparison. The values retrieved by OCA and CLAAS 2.1 are closer to each other and significantly lower than those retrieved from MODIS. OCA retrieves, on average, the lowest values, except for the areas at high latitude where the contribution of solar channels is less when the regions are partially in the shadows during the winter season. This underestimation may be partly explained by the fact that 1) average OCA values may contain both ice and, to a smaller amount, liquid cloud clouds (section 5.2), and 2) OCA tends to retrieve too small ice particles size for two-layer pixels. This was already observed from the comparison against DARDAR products, where the largest underestimation was reported for two-layer clouds (section 7.1).

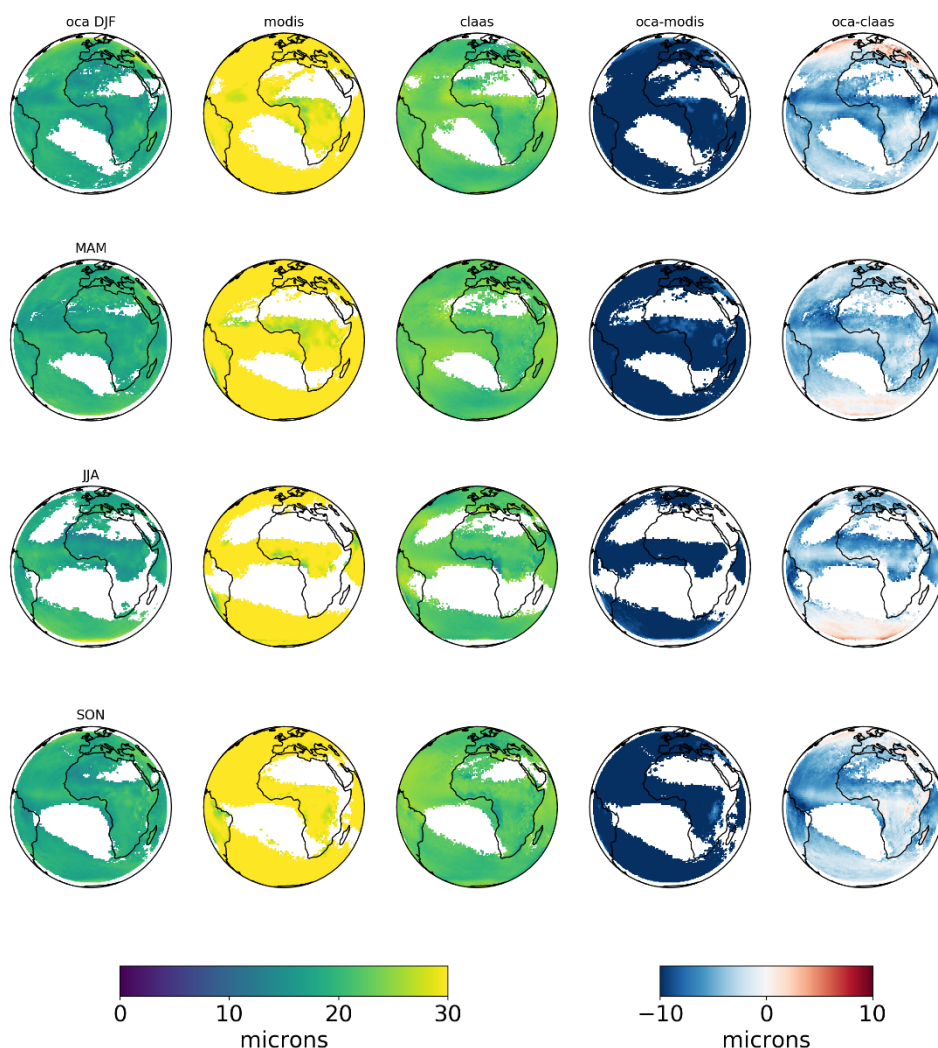


Figure 32: Seasonal mean ice water clouds effective radius (CRE) from OCA (single layer and two-layer), MODIS and CLAAS 2.1 datasets. On the right the difference between OCA and respectively MODIS and CLAAS 2.1. White areas in the OCA and CLAAS 2.1 figures indicate regions where not enough valid retrieval were available for this cloud phase. Similarly for the MODIS figures the white areas are regions for which the ice cloud fraction according to the *Cloud_Retrieval_Fraction_Ice_FMean* variable is less than 0.2 (see section 5.2).

The time series of the retrieved ice particle size (Figure 33) shows that the differences between the three datasets are stable throughout the period without any significant trend.

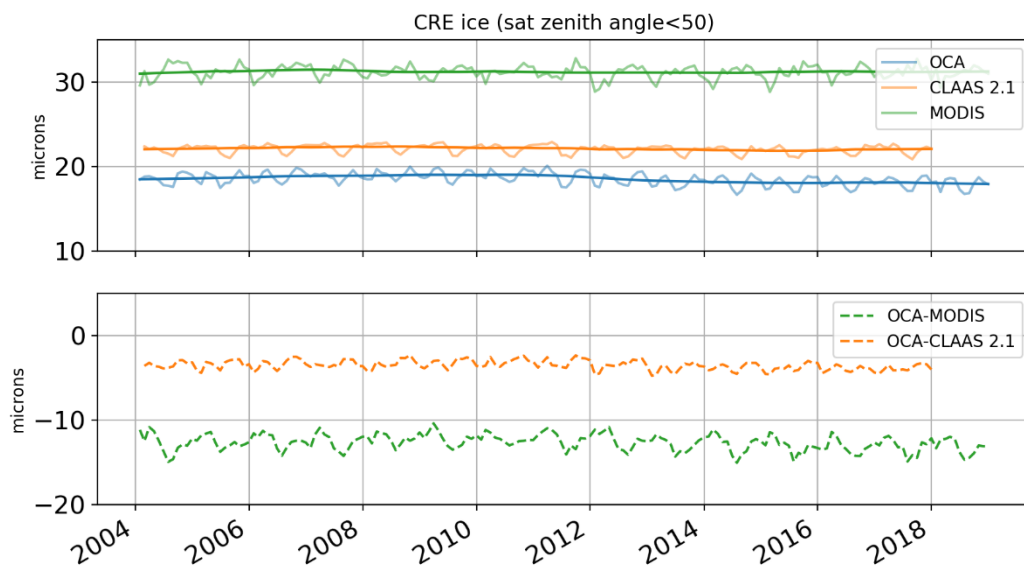


Figure 33: *Weighted area-average of retrieved ice water cloud effective radius (CRE) from OCA (single layer and two-layer), MODIS and CLAAS 2.1 datasets over a SEVIRI disk. Averages are done for the areas within a maximum SEVIRI viewing angle of 50°. Top panel: monthly means with a lowess (locally weighted scatter plot smooth) smoothing filter applied to each time series. Lower panel: differences between OCA and respectively MODIS and CLAAS 2.1*

The retrieved particle sizes for liquid water cloud show a closer agreement between the three data records than those for ice clouds. This is expected because of the lower uncertainty of the liquid droplet shape and size distributions. Values of OCA are slightly higher than those of other two CDRs because 1) average OCA values may contain both water and, to a smaller amount, ice clouds (section 5.2) 2) in areas where the solar channels are not available, the retrieved CRE tends to be too large (Figure 34). As already discussed for the CTP (see section 7.2.1), a significant number of retrievals over the Sahara desert include very thin ice clouds detected by the cloud mask used in OCA. The algorithm retrieves these pixels as low altitude water clouds, resulting in an anomalously high number of liquid water particles with large sizes. The user can remove the occurrence of these retrievals by filtering the L2 data with a higher threshold of the cloud probability mask.

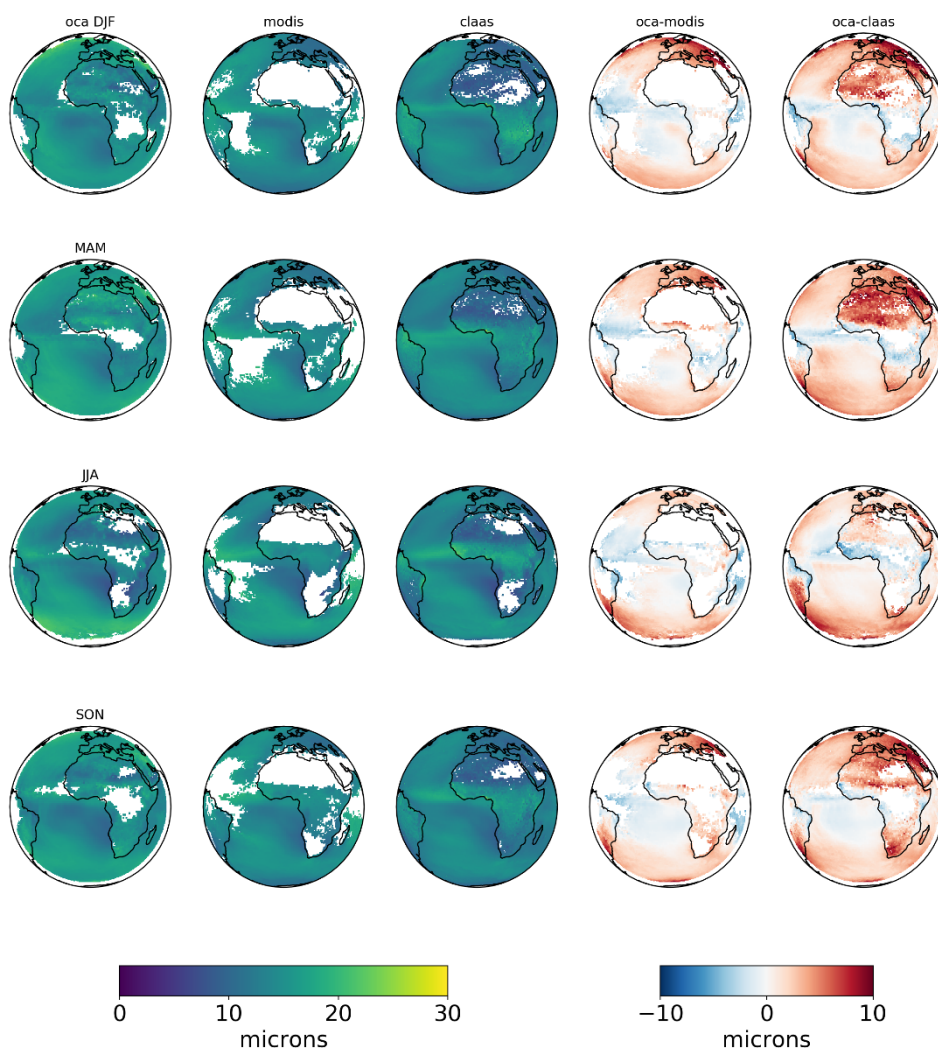


Figure 34: Seasonal mean liquid water clouds effective radius (CRE) from OCA, MODIS and CLAAS 2.1 datasets. On the right the difference between OCA and respectively MODIS and CLAAS 2.1. White areas in the OCA and CLAAS 2.1 figures indicate regions where not enough valid retrieval were available for this cloud phase. Similarly for the MODIS figures the white areas are regions for which the liquid cloud fraction according to the *Cloud_Retrieval_Fraction_Liquid_FMean* variable is less than 0.3 (see section 5.2).

On average, the mean differences in the retrieved liquid particle sizes of the three CDRs are in the order of 1-2 μm over the SEVIRI disk (Figure 35). However, the OCA time series shows a distinct annual cycle with a peak around March/April. Again this is mostly linked to the already mentioned anomalous number of liquid clouds with large droplet size over the Sahara Desert. No significant trends are observed in the time-series.

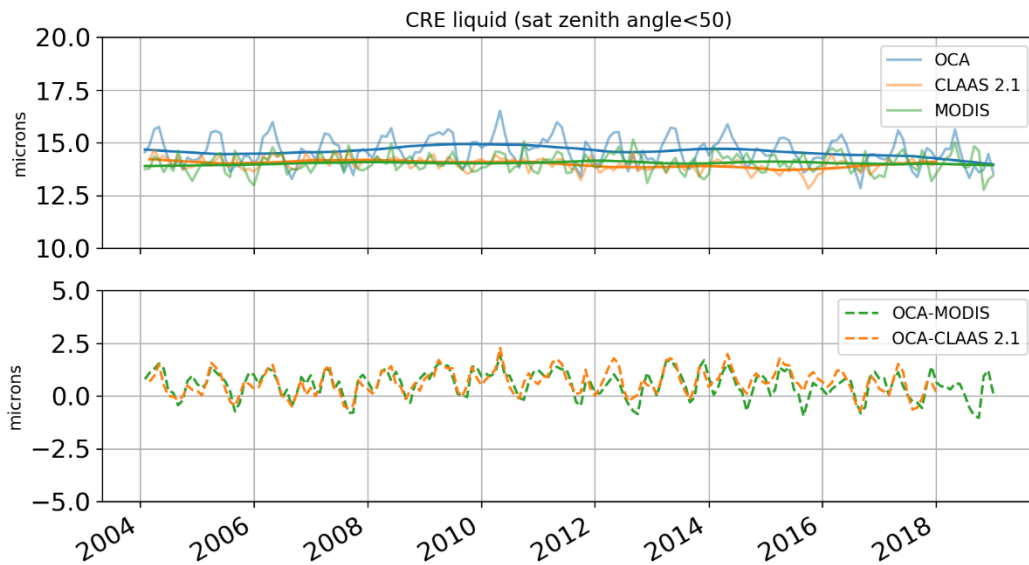


Figure 35: Weighted area-average of retrieved liquid water cloud effective radius (CRE) from OCA, MODIS and CLAAS 2.1 datasets over a SEVIRI disk. Averages are done for the areas within a maximum SEVIRI viewing angle of 50°. Top panel: monthly means with a lowess (locally weighted scatter plot smooth) smoothing filter applied to each time series. Lower panel: differences between OCA and respectively MODIS and CLAAS 2.1

8 COMPARISON OPERATIONAL NEAR REAL TIME (NRT) SEVIRI OCA

This section presents the comparison of the CTP products from OCA Release 1 CDR and the OCA NRT. The CTP products from both retrievals are based the same algorithm. However, there are some differences, in particular in the in the usage of input auxiliary data, i.e.:

- Cloud mask: NRT used the SEVIRI NRT MPEF cloud mask at pixel resolution. This is not available for the CDR, so instead the independent CM-SAF SEVIRI cloud mask processor is used (EUMETSAT, 2021).
- Model data: NRT uses forecast (latest model output at run time) data from ECMWF. The CDR uses ERA-INTERIM (2006) forecast. The NRT product uses just 30 vertical RTTOV levels, while in the CDR the 54 RTTOV levels.
- Clear sky reflectance maps: The maps are the same, but for CDR not all were available and it has been necessary to use maps of a different year as explained in the PUG (EUMETSAT, 2021)

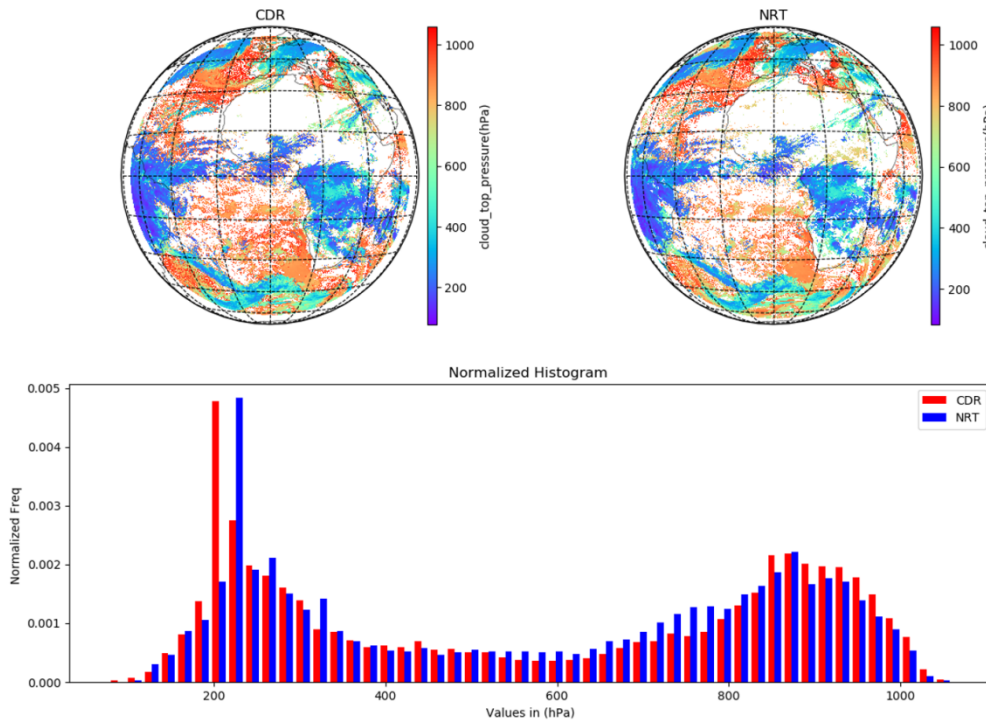
The comparison is limited to the CTP product because it is the most relevant OCA product for the AMV retrievals. The objective of this comparison is to show that NRT and CDR retrievals are consistent in their absolute values and seasonal behaviour. Two sets of comparison have been performed:

- Firstly, a single product comparison in order to appreciate potential differences at the pixel level. For instance, to check if a geographical pattern (latitude or longitude related) or surface type related (desert, forest, water) appears. However, the differences could also arise of course from the different cloud masking because the independent cloud mask used in the CDR is based on two channels only. This may be less accurate over bright deserts or in the night, for example. The model data used as input can also impact the retrieval. The model used for ERA-INTERIM (Integrated Forecast System (IFS) model cycle 31r2) is about 12 years older than the model version used for the forecast in the January 2018 case analysed here (IFS model cycle 43r3). The impact of the model evolution is clearly shown in the paper by Hoffmann et al., 2019 comparing ERA5 against ERA-INTERIM. The different model data together with the higher number of vertical RTTOV levels used in OCA for the CDR will lead to a different cloud height estimates.
- Secondly, a comparison performed over a full year (both day and night) is used to show any seasonal variations of disk-averaged values.

8.1.1 Single product comparison

The comparison shows that the instantaneous CTP retrievals are very similar. The images in Figure 36 and Figure 37 show that the same cloud patterns are found in the CDR and NRT products. Moreover, this Figure shows that the histograms of the cloud height distribution is almost identical. The only difference is for high clouds between 200 and 240 hPa and low clouds between 700-800 hPa. These generally occur in regions dominated by either high thin cirrus or low stratocumulus clouds associated with temperature inversions. In case of thin cirrus clouds, the algorithm uses the input forecast level as initial first guess for the position of the cloud layer. When the retrieval manages to move the cloud layer from its initial position, this remains dependent on the input forecast levels. Similarly, the position of low clouds is related to the height of the temperature inversion, making the accuracy of the CTP retrieval solely dependent on the vertical resolution of the input meteorological profile. The observed difference occurs in both the daytime and nighttime products, and may be largely attributed to the difference between the NWP forecasts used for the NRT retrievals and reanalysis data used for the CDR retrievals.

OCA comparison NRT vs CDR cloud_top_pressure (hPa) - 26 January 2018: 0 UTC



OCA comparison NRT vs CDR cloud_top_pressure (hPa) - 26 January 2018: 1200 UTC

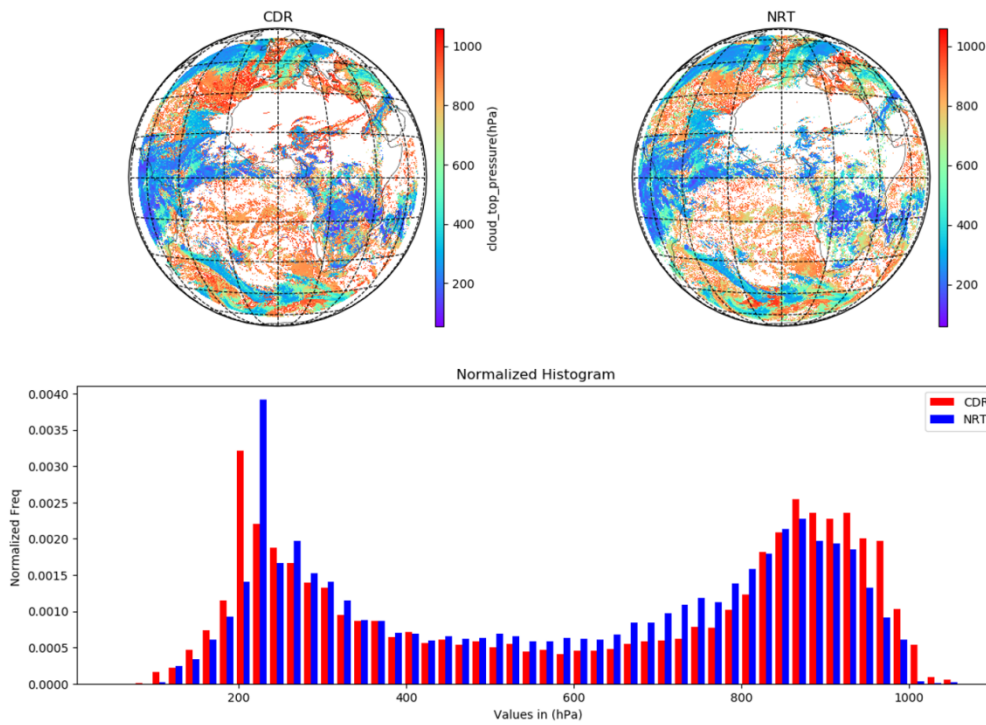
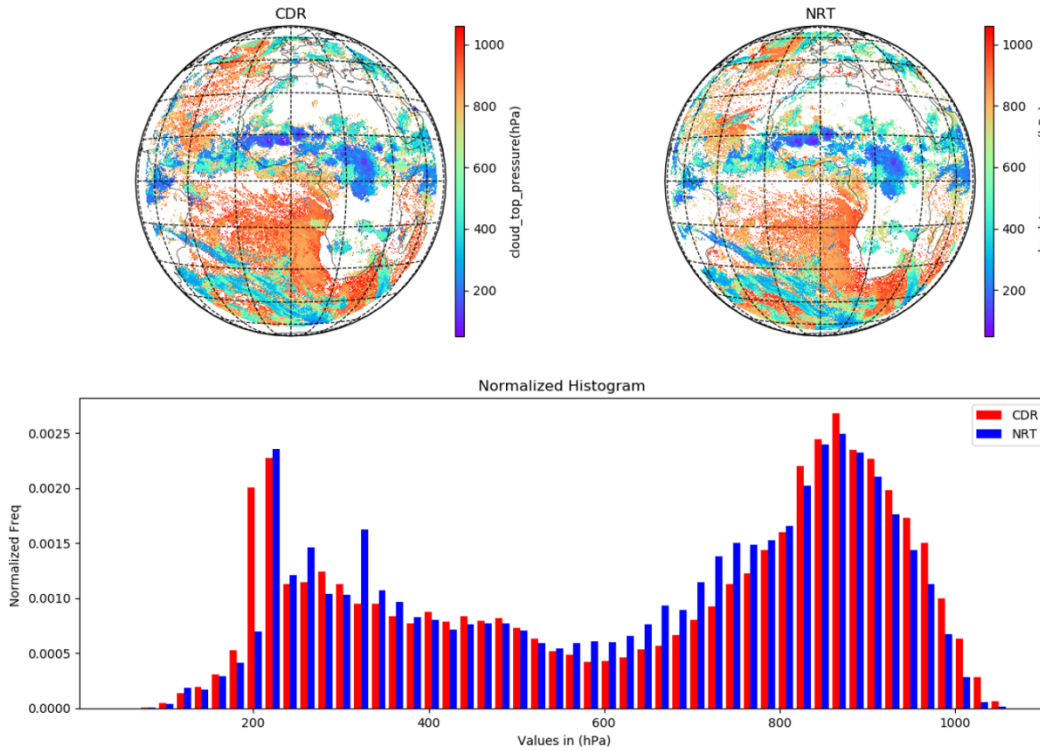


Figure 36: Comparison of single products for the 26th of January 2018 boreal winter: night case (upper panel) and daylight case (bottom panel).

OCA comparison NRT vs CDR cloud_top_pressure (hPa) - 15 July 2018: 0 UTC



OCA comparison NRT vs CDR cloud_top_pressure (hPa) - 15 July 2018: 12 UTC

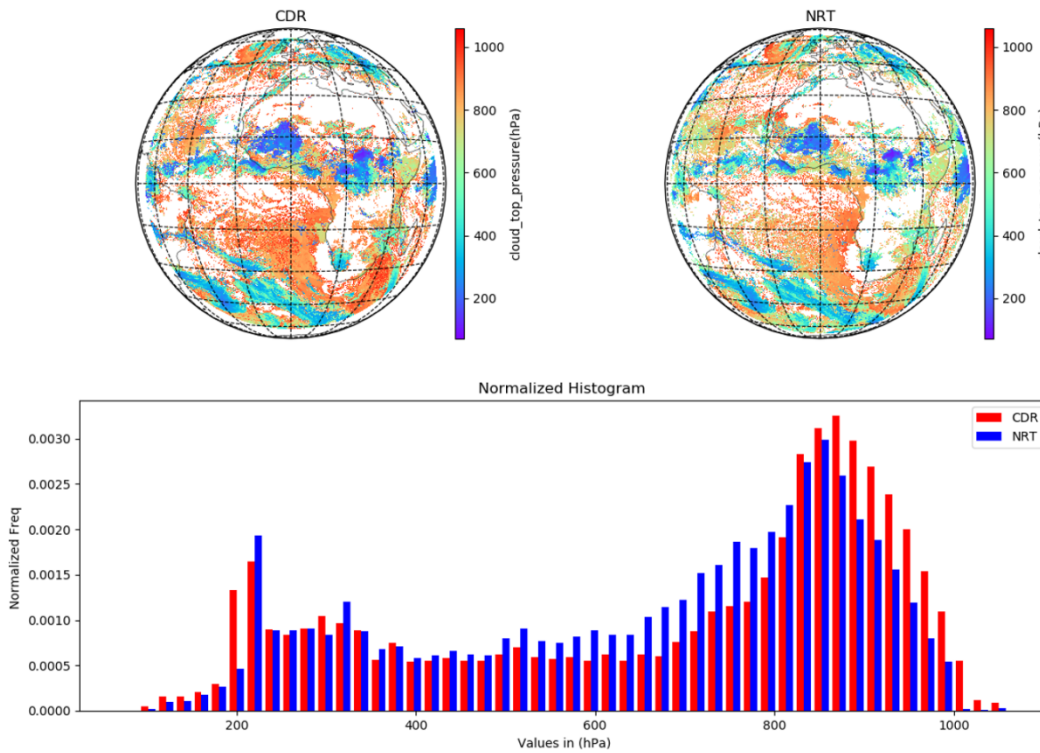


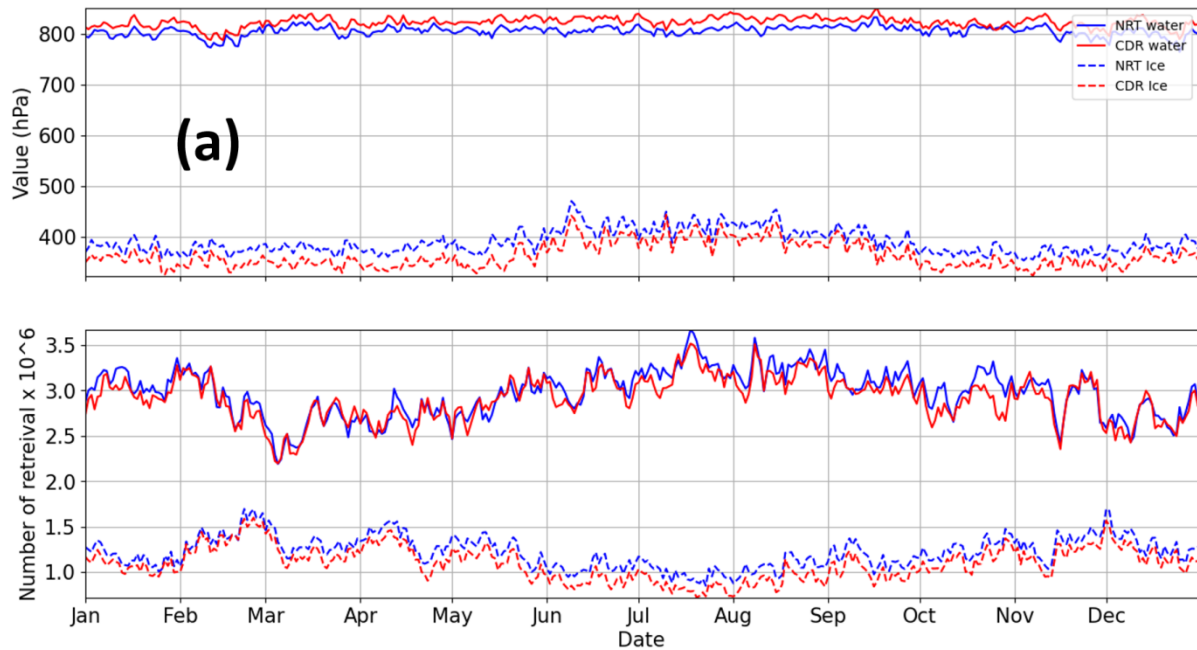
Figure 37: Same as Figure 36 for boreal summer: 15th of July 2018

8.1.2 Long term comparison

In this section the impacts of using a different cloud masks in NRT and in the CDR retrievals are evaluated. Hereto, a quantitative comparison is done using different set of pixels to compute the average over the full disk, i.e., (a) all pixels of the CDR and NRT retrievals are used; (b) only pixels with retrievals from both CDR and NRT are used. The comparison is done (Figure 38 and Figure 39) for both ice (dashed line) and water phases (continuous line). The cloud top pressure (in hPa) have been analysed for two observation times, i.e., one at night (00 UTC) and one in the day (12 UTC). The comparison of the 00 UTC retrievals (Figure 38) shows that CDR and NRT are very close when all retrieved pixels are used, while CDR clouds are slightly higher in the atmosphere (lower cloud top pressure) than NRT clouds when only common retrieved pixels are used. The result is the opposite for the 12 UTC case (Figure 39). In both cases the impact of using a different number of clouds processed by OCA is clear and introduces a pressure difference between 20 and 30 hPa. This difference could then be related with the different model data used, latest model forecast for NRT and ERA-Interim forecast from 2006 for CDR and different vertical resolution used, as mentioned in Section 8.

In conclusion, the one-year analyse presented here shows that NRT and CDR OCA products are well in-line with each other.

Comparison for cloud_top_pressure 2018 (slot 0UTC)



Comparison for cloud_top_pressure 2018 (slot 0UTC, only common retrieval)

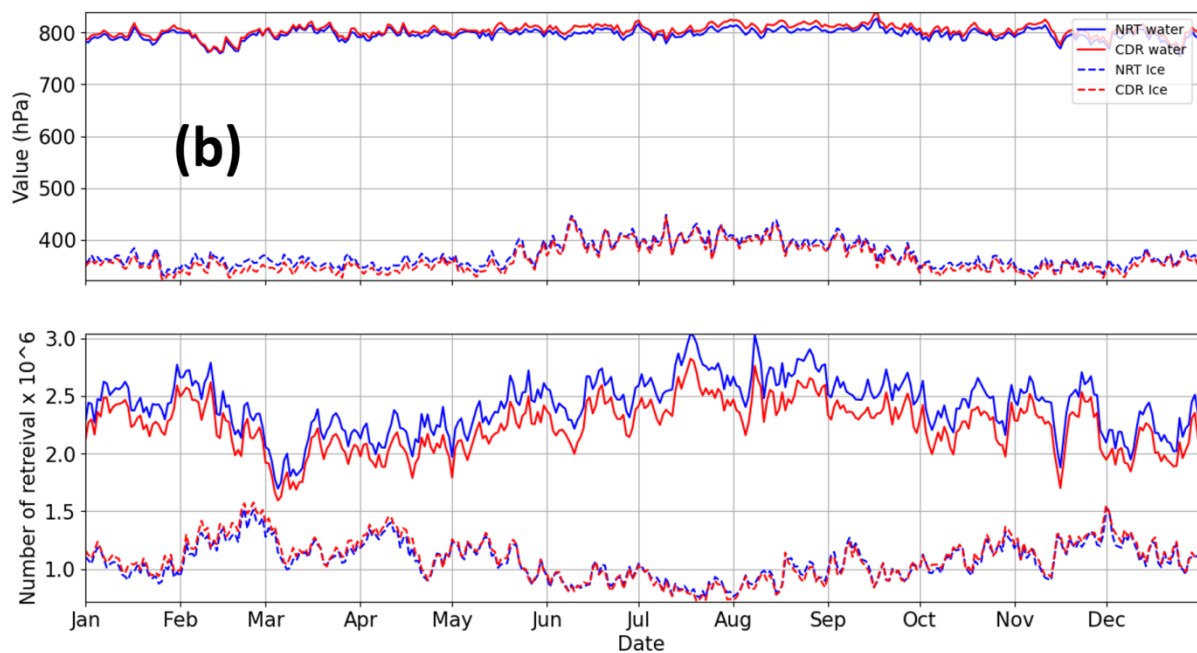
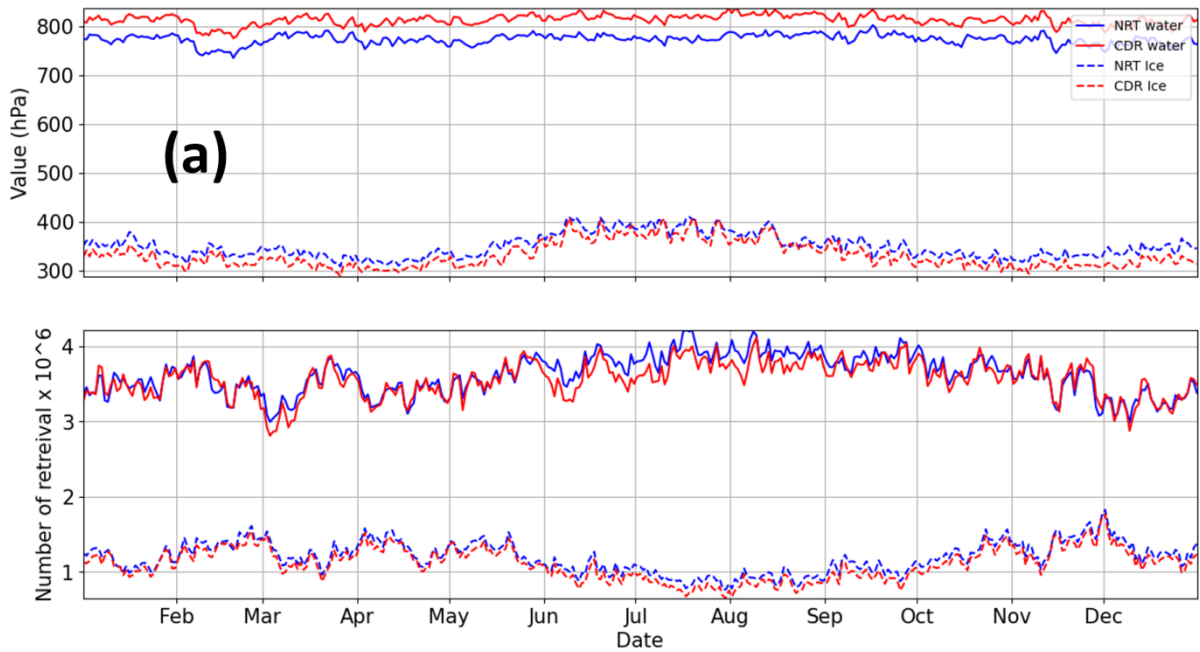


Figure 38: Case at 00 UTC (a) all pixels used for the average; (b) only common retrieved pixels used for the average. Cloud top pressure in hPa (upper plot) and number of retrievals (bottom plot). NRT in blue, CDR in red, dashed line for ice and continuous line for water.

Comparison for cloud_top_pressure 2018 (slot 12UTC)



Comparison for cloud_top_pressure 2018 (slot 12UTC, only common retrieval)

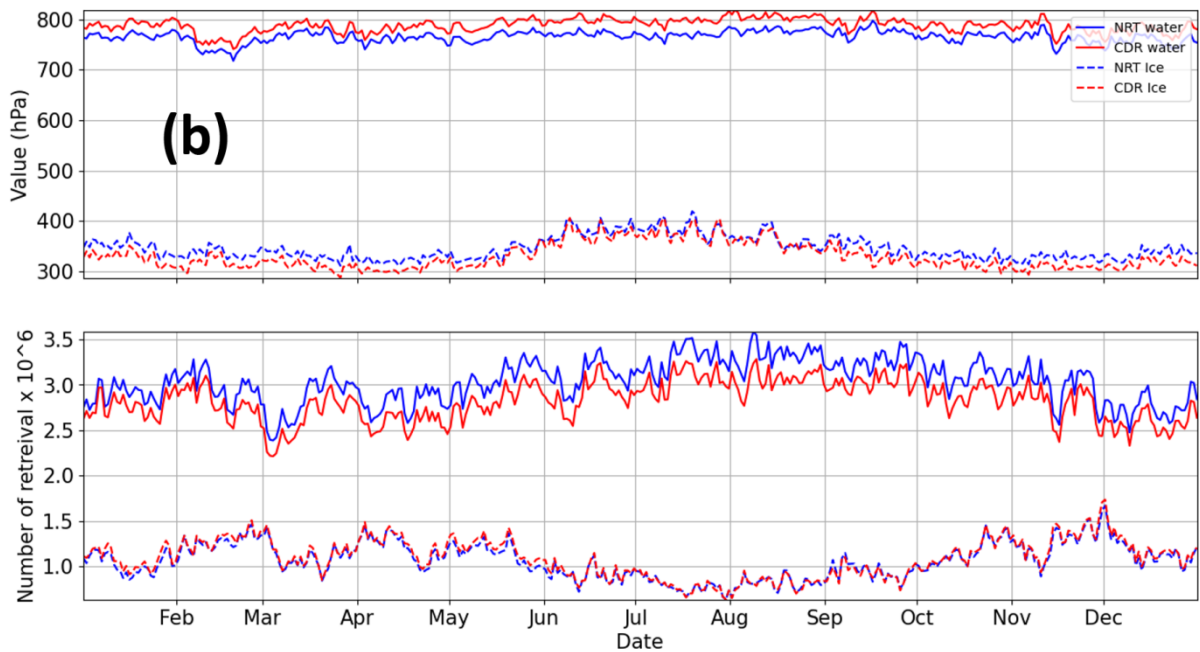


Figure 39: Same as Figure 38 for the daylight case at 12:00 UTC.

9 LIMITATIONS AND POSSIBLE FUTURE IMPROVEMENTS

In the OCA Release 1 CDR, the following limitations should be considered by the users. Potential improvements to the algorithm or its inputs are given when possible and if already implemented for tests.

1. The daytime and nighttime products from OCA have different systematic and random uncertainties in COT and CRE. This limitation does not apply to the CTP. Since the ratio between daytime and nighttime COT and CRE retrievals varies with location and season, one should restrict their usage to only daytime or only nighttime observations in climate research, such as studying diurnal cycles of seasonal variations.
2. A cloud screening that is not state of the art (e.g. current operational standard) gives false detections over deserts at night which, combined with poor constraints on COT at night, leads to anomalously high values.
3. Anomalously high CTP values over bright surfaces. This is due to the inherently challenging cloud detection and properties retrieval over such areas. However, for the current CDR, this issue could be a consequence of a false cloud detection in the input cloud mask adopted for the OCA retrieval. As mitigation measure, the input cloud mask array is included in the product so that any user can decide for further pixel screening depending on the application. **Improvement:** A state of the art cloud mask or the current mask with a threshold dependent on the underlying surface conditions will be used.
4. Like other retrievals based on passive imagers, OCA CTPs are generally higher (lower altitude) than observed CTPs (e.g. as sensed by satellite or airborne lidars). Maximum differences (~1.5 km) are found for high thin ice clouds. **Improvement:** More realistic modelling of cloud extinction in the algorithm forward radiative transfer.
5. Clear sky reflectance maps were not archived operationally at EUMETSAT for the complete period (2004-2019). Maps for a different day or even for a different year (same day) were used in case of a gap. This may have introduced some level of dynamic but systematic error in the daytime retrieval of COT and CRE for thinner clouds. **Improvement:** Regeneration of the missing clear sky reflectance maps.

10 CONCLUSIONS

The main conclusion from the validation are as follows:

- The CDR is stable and homogeneous over the entire period.
- The CDR is consistent when compared against measurements and retrieval products from CloudSat and CALIPSO collocated with SEVIRI pixels over the period 2007-2015. The biases in the OCA products known already from previous studies, have been confirmed. In particular, when the reference cloud top height is defined by lidar measurements, radiometer-based cloud top height retrievals like OCA tend to be biased low, especially for high thin ice clouds (~1.5 km below the real top). The cloud top height retrieval for overlapping cloud layers shows larger biases than for single layer clouds. The retrieval of the cloud optical thickness and particle effective radius is most reliable for daytime measurements while the cloud top height retrieval is of comparable quality for daytime and nighttime SEVIRI slots.
- CRE is significantly more accurate when solar channels are available. Nighttime retrievals produce particle sizes that generally are too large, especially for single layer ice clouds. Similarly, the current two-layer algorithm is restricted to use of infrared channels and these retrievals also suffer from the lack of solar channel input. This last limitation can be mitigated by the use of a more complete radiative transfer model that includes solar channels when available. This is currently investigated for the next version of the algorithm.
- The CDR and archived near real time OCA products are consistent and in close agreement. However, some differences appear due to the usage of different input data for the retrieval. The differences in cloud top pressure between the CDR and NRT products are due to the usage of a different cloud mask and different model data as inputs. The cloud mask used in the CDR has a larger amount of thin cirrus for which the reliability of OCA retrieval is low. The cloud mask is included in the data files so it can be used by users to filter out products based on different cloud probability thresholds. The CDR uses the ERA-Interim reanalyses meteorological profiles while the NRT uses operational model forecasts data. Those model data are used in the CDR at a higher vertical resolution than for the generation of the NRT products and this has an impact especially on the definition of cloud top height close to temperature inversions.
- The comparison of the OCA Release 1 CDR against other two independent satellite reference CDRs (MODIS L3 and CLAAS 2.1) shows that the products of the three different algorithms are compatible and consistent over the whole period 2004-2019. However, it can at some particular time differs, as for example for cloud ice particle size where the results differ significantly. OCA shows a significant downward trend of the cloud optical thickness time series, not observed in the other two CDR. A possible cause of this is that it was not possible to incorporate the latest calibration information on the short-wave channels in the creation of this CDR.

Appendix A TIME SERIES AT 00 AND 12UTC

Figure 40 and Figure 41 present an example of the cloud properties time series (CRE, COT, and CTP) for a day and a night products: daytime at 12UTC and nighttime at 0UTC. For both night and day series, the generated cloud properties are homogeneous and stable. The difference between daytime/nighttime ice CRE values was discussed when comparing against DARDAR (Section 7.1).

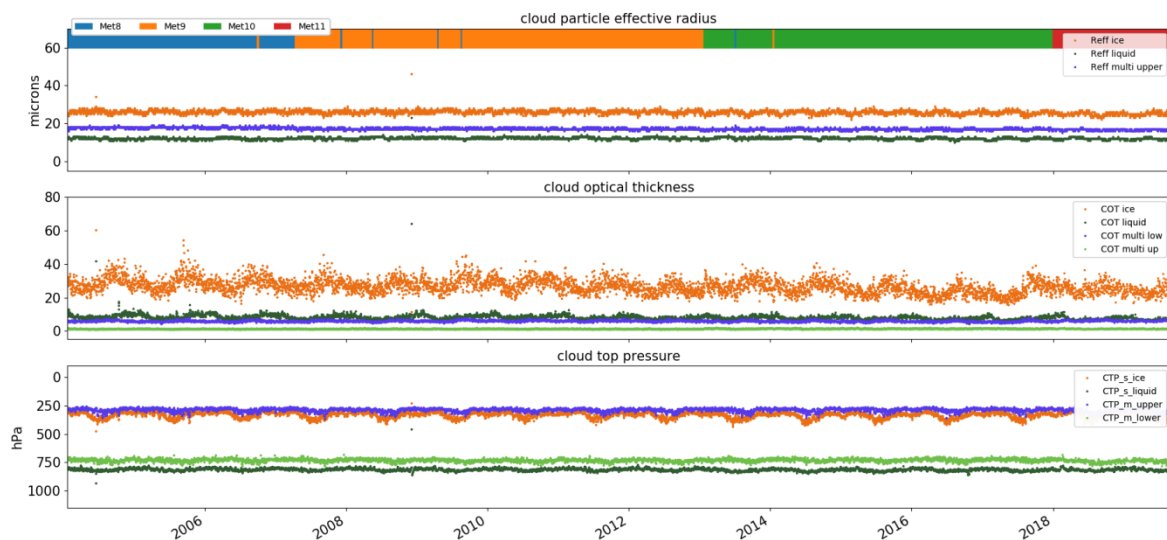


Figure 40: Time series for the 12UTC repeat cycle for the cloud properties averaged over the SEVIRI disk: CRE (upper panel), COT (middle panel) and CTP (bottom panel). The plots distinguish among the cloud phases. The upper bar in the upper panel shows the lifetime of the primary satellite providing the measurements. The colorbar at the top shows the Meteosat satellite used at a particular point in time.

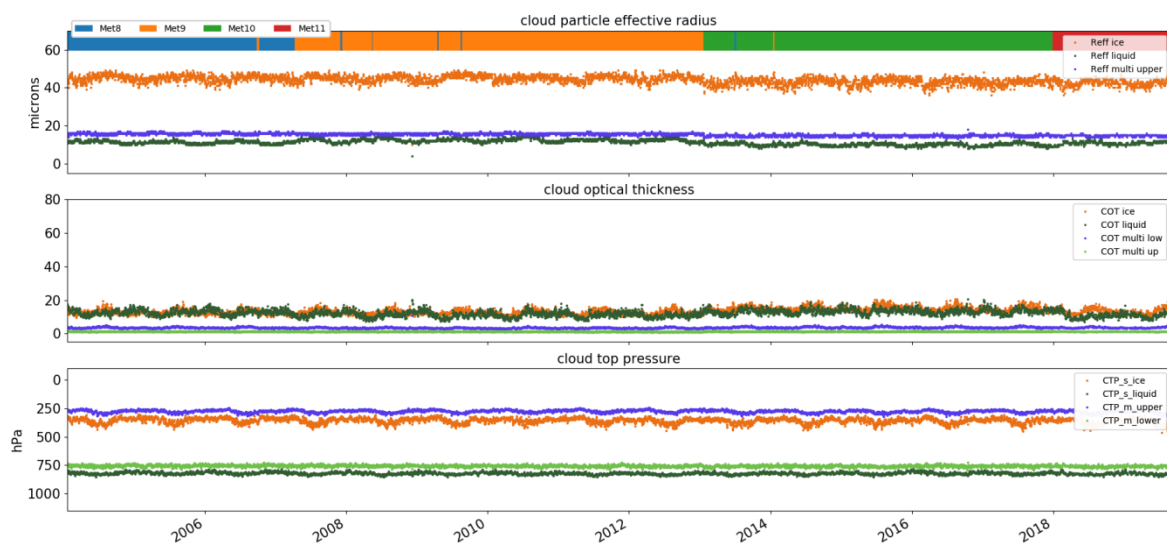


Figure 41: As but for the 00UTC repeat cycle.

Appendix B HOVMOELLER DIAGRAM FOR ALL DAY RETRIEVAL

This section contains the Hovmoeller diagram considering both daylight and nighttime retrieval (one product/hour is used). The main difference if compared with the daylight only case is in the 20°-30° North belt. This is because the combination of possibly wrong cloud assignment from the cloud mask and the Sahara Desert surface type result in a wrong COT retrieval.

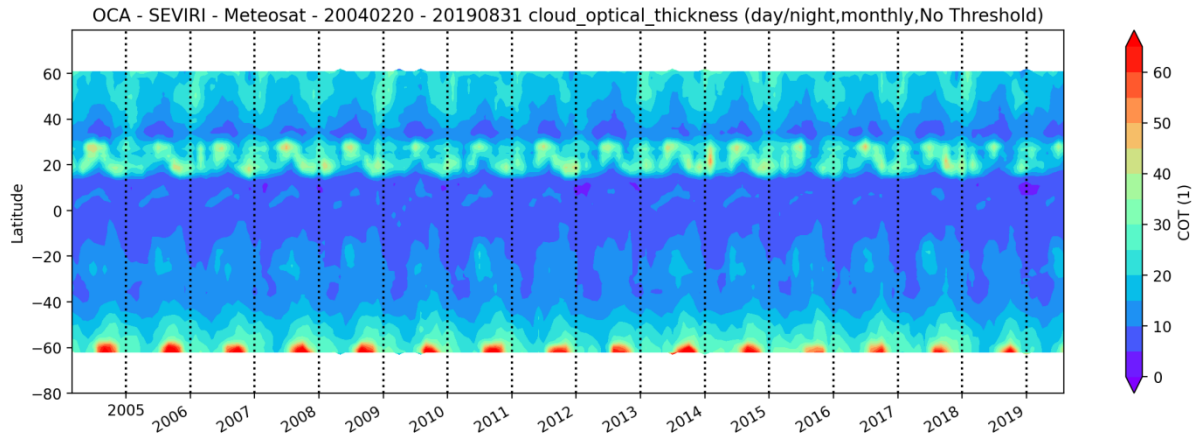


Figure 42: Monthly Hovmoeller diagrams for zonal mean (60°-60°) COT. No threshold on the available number of days per month is applied

The CTP and CRE show some changes in the values (due to a different set used for the average) but no specific spatial/temporal artefact as present for COT.

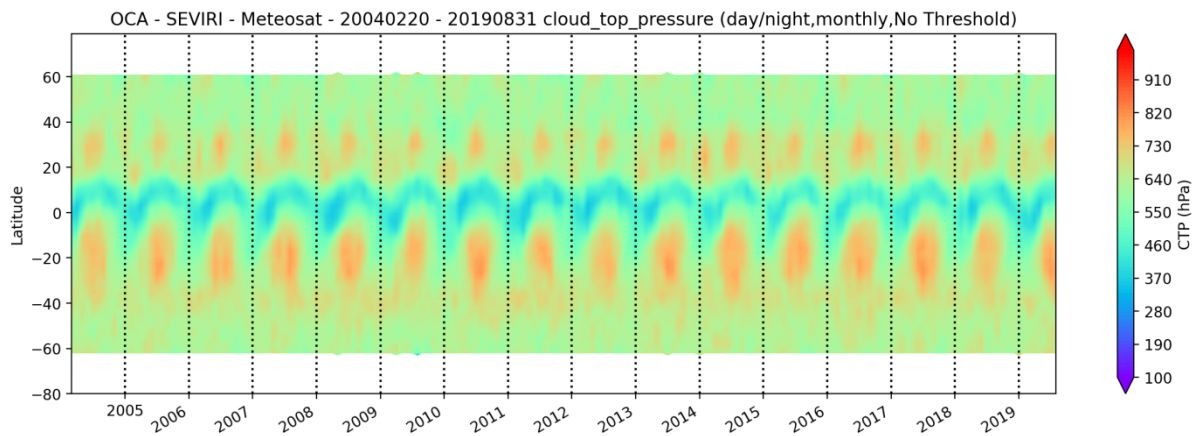


Figure 43: Monthly Hovmoeller diagrams for zonal mean (60°-60°) CTP. No threshold on the available number of days per month is applied

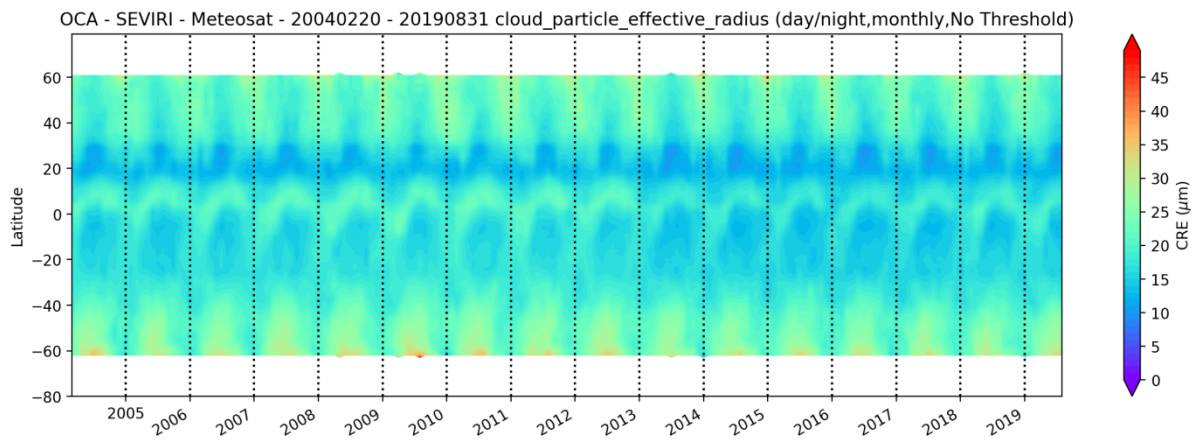


Figure 44: Monthly Hovmoeller diagrams for zonal mean (60°-60) CRE. No threshold on the available number of days per month is applied